CHARACTERIZATION OF DEVICES AND MATERIALS FOR GALLIUM NITRIDE AND DIAMOND THERMAL MANAGEMENT APPLICATIONS

by

Bobby Logan Hancock, B.S., M.S.

A dissertation submitted to the Graduate Council of
Texas State University in partial fulfillment
of the requirements for the degree of
Doctor of Philosophy
with a Major in Materials Science, Engineering, and Commercialization
December 2016

Committee Members:

Mark Holtz, Chair

Edwin Piner

Alex Zakhidov

Thomas Myers

Jeff Wetzel

FAIR USE AND AUTHOR'S PERMISSION STATEMENT

Fair Use

Duplicate Permission

ACKNOWLEDGEMENTS

I am very fortunate to have had the opportunity to work and grow alongside many fine individuals throughout my graduate experience in the Materials Science, Engineering, and Commercialization (MSEC) program at Texas State University.

First and foremost, I would like to thank my advisor, Dr. Mark Holtz. I am sincerely grateful for his dedication and personal investment in his students and his graceful abilities to teach and motivate. Through countless thoughtful discussions and never missing an opportunity to share a laugh, his guidance has made my PhD experience worthwhile. It has been an honor to work under his direction.

I also extend my appreciation to Dr. Edwin Piner for his collaboration, contributing his time in discussion and counsel, and for being an invaluable resource in all things GaN. A special thank you is also due to his CVD research group – Jon Anderson, Jeff Simpson, Raju Ahmed, and Anwar Siddique – for all of their help and cooperation, in research and camaraderie.

To my lab-mates at Texas State, both in Physics and MSEC, I am thankful for their support and friendship in and out of the lab. I owe a special gratitude to Mohammad Nazari, Sandeep Sohal, and Brian Squires for the many years spent enduring my company in the – often uncomfortably – close quarters of a dark, noisy spectroscopy lab.

I would like to thank the Texas State ARSC technical team and support staff, with special acknowledgement to Dr. Casey Smith, Eric Schires, Alissa Savage, and Nate

England for the many hours spent training and answering my questions. Their impressive skillsets are second only to their approachability and patience with novice trainees such as myself.

I would like to thank the MSEC program for providing financial support for my doctoral degree and the MSEC faculty and staff for delivering a unique and fulfilling graduate experience. I also gratefully acknowledge the Defense Advanced Research Projects Agency (DARPA) for partial funding of my PhD research.

I thank my committee members, Dr. Alex Zakhidov, Dr. Thomas Myers, and Dr. Jeff Wetzel for their advice, encouragement, and cooperation during the preparation of my dissertation work.

I am extraordinarily grateful for my family, which encompasses a list of exceptional individuals too long to enumerate and too important to describe. Their continual encouragement and unconditional support of my success throughout the course of my education is invaluable. This list includes my wife's family, whose patience and reassurance has been uplifting and has provided a constant source of drive.

Finally, and most importantly, I thank my wife, Christian. Without her love, support, and constant motivation, none of this would have been possible.

TABLE OF CONTENTS

LIST OF TABLES

Table **Page**

LIST OF FIGURES

Figure **Page**

ABSTRACT

As trends progress toward higher power applications in GaN-based electronic and photonic devices, the issue of self-heating becomes a prominent concern. This is especially the case for high-brightness light-emitting diodes (LEDs) and high electron mobility transistors (HEMTs), where the bulk of power dissipation occurs within a small (sub-micron) region resulting in highly localized temperature rises during operation. Monitoring these thermal effects becomes critical as they significantly affect performance, reliability, and overall device lifetime. In response to these issues, diamond grown by chemical vapor deposition (CVD) has emerged as a promising material in III-nitride thermal management as a heat-spreading substrate due to its exceptional thermal conductivity. This work is aimed toward the characterization of self-heating and thermal management technologies in GaN electronic and photonic devices and their materials. The two main components of this dissertation include assessing self-heating in these devices through direct measurement of temperature rises in high-power LEDs and GaN HEMTs and qualifying thermal management approaches through the characterization of thermal conductivity and material quality in CVD diamond and its incorporation into GaN device layers. The purpose of this work is to further the understanding of thermal effects in III-nitride materials as well as provide useful contributions to the development of future thermal management technologies in GaN device applications.

1. INTRODUCTION

In this first chapter, an introduction will be given to the III-nitride (III-N) family of materials and their significance in the communities of semiconductor research and industry. A brief overview of the devices pertinent to the studies in this dissertation will be presented, followed by a discussion of the issues facing these devices in the context of self-heating and thermal management. The use of diamond as an effective heat-spreading substrate in response to the problem of self-heating in high-power III-N devices will be described. In the final section of this chapter, an overview of the scope and overall objectives of this dissertation will be presented.

1.1 III-nitride Materials and Devices

Considerable advancements in semiconductor research and industry have been seen recently for technologies involving III-nitride (III-N) materials. GaN, InN, AlN, and their ternary compounds, AlGaN and InGaN, exhibit many unique material properties and have displayed exceptional promise in recent decades as excellent semiconductors. Covering the spectral range from ultraviolet (UV) to infrared (IR), III-N compounds have demonstrated admirable applications in optoelectronics and commercial lighting. Robust performance capabilities in high power, high frequency, and high temperature roles have also given these wide band gap materials a promising potential in the electronic and communication industries by reaching application spaces other semiconductors were unable to address.

From a materials standpoint, III-nitrides offer many advantages over existing semiconductor technologies. As illustrated in Fig. 1.1, the wide energy band gap range

offers extensive opportunities for device capabilities. The various ternary compounds offer versatility through stoichiometric compositions along the energy spectrum. The additional ability for the production of successful hetero-structures has also contributed to expanding the flexibility of III-N applications. The direct band gap across multiple compositions is preferable for optoelectronic devices and has demonstrated the utility of GaN-based materials in the successful production of light-emitting diodes (LEDs), laser diodes (LDs), photodetectors, and photovoltaics (PVs). The role of GaN in the research and commercial industries for these devices is flourishing with expanses in green, blue, and white high-power and high-brightness LEDs due to good reliability and energy conservation when compared to traditional lighting [1]–[4]. Complex heterostructures and multiple quantum well (MQW) architectures have also led to superior performance enhancements in this market due to further advantages in thermal management and light-extraction [5], [6].

Similar benefits are paralleled in nitride electronic applications. For transistors, GaN-based devices have made considerable strides compared to existing silicon and arsenide technologies. Attractive material properties such as high breakdown voltage, electron mobility, and thermal conductivity have given rise to higher output powers at high frequency and high temperature capability [7]–[10]. The comparison in Tbl. 1.1 summarizes the quantitative attributes of GaN over those for other common device materials [7], [10]–[13]. From the table, competitive advantages are seen in breakdown field E_{br}, saturation velocity v_{sat}, mobility μ, and thermal conductivity κ by considerable amounts compared to Si and GaAs. The final term in this list, JM, denotes the Johnson power-frequency figure of merit. This quantity is used to assess the potential of a material

for high-frequency applications, demonstrating the performance limitation in transistor technologies [7], [10], [13]–[15].

Table 1.1. Comparison of material properties for various semiconductors. Adapted from [7], [11], [12].

	Si	GaAs	SiC	GaN
Band gap, $\boldsymbol{E_g}$ (eV)	1.1	1.42	3.26	3.39
Mobility, $\boldsymbol{\mu}$ (cm^2/Vs)	1300	8500	700	1000-2000
Electron saturation velocity, $\boldsymbol{v_{sat}}$ (10^7 cm/s)	1.0	1.3	2.0	2.5
Breakdown field, $\boldsymbol{E_{br}}$ (MV/cm)	0.3	0.4	3.0	3.3
Thermal conductivity, $\boldsymbol{\kappa}$ (W/cmK)	1.5	0.5	4.5	>1.5
Dielectric constant, $\boldsymbol{\varepsilon_r}$	11.8	13.1	10.0	9.0
Johnson Fig. of Merit, $\boldsymbol{JM = E_{br}v_{sat}/2\pi}$	1	2.7	20	27.5

As technology and research progress into higher power and frequency regimes, the issue of self-heating becomes a more prominent concern. In most cases, the device is experiencing extreme power dissipation within a small (sub-micron) region, resulting in a highly localized rise in temperature during operation. Monitoring these device thermal effects becomes critical as they significantly affect the performance, reliability, and overall device lifetime. In LEDs, unwanted heating can lead to considerable losses in quantum efficiency, changes in output wavelength, device lifetime, and material deterioration [5], [6], [16]–[18]. For electronic devices, residual heat causes losses in efficiency and output power density, decrease in electron mobility, and device degradation [7], [9], [19].

Considerable research has focused on investigating self-heating effects in III-N photonic [6], [17], [18], [20], [21] and electronic devices [9], [22]–[28], utilizing a number of different techniques and approaches. As this technology progresses, increased knowledge of this self-heating issue is crucial to advancements in device reliability and design optimization.

Efforts for mitigating the thermal effects in III-nitride devices have begun to focus on unique avenues for addressing vertical heat-dissipation through the device material by incorporating good thermal conductors in close proximity to the active epilayers. Of these approaches, synthetic diamond has emerged as a promising material for efficient evacuation of heat as a substrate or heat-spreading layer. The growth of diamond using chemical vapor deposition (CVD) has improved in both sustainability and material quality, leading to promising results for the successful incorporation of diamond heat-spreading films and substrates into high-power GaN devices [29]–[33].

The purpose of this body of work is to further the understanding of thermal effects for GaN high-brightness light-emitting diodes and high electron mobility transistors as well as the efficacy of current thermal management schemes. This is accomplished by providing in-depth characterization of the self-heating issues inherent to these devices as well as addressing the characteristics and sustainability of current GaN-on-diamond technologies. This chapter provides an overview of the materials and devices of interest for the chapters to follow, introduces the current issues involving self-heating in these particular devices, and presents the rising potential of diamond as a formidable solution in GaN thermal management.

1.1.1 Light-emitting Diodes

Solid-state lighting in industrial and commercial applications has seen considerable growth in recent years along with the utilization of LEDs with high-power and high-brightness capabilities. The global market for LEDs is projected to reach $42.7 billion by 2020, with a compound annual growth rate of 13.5% from 2014 - 2020 [34]. A leading step in this movement was the development of GaN-based high-brightness blue/green LEDs in the mid-1990s capable of reasonable luminous efficiencies [1], [2]. These innovations paved the way for white LEDs and have profoundly revolutionized the lighting industry by offering light sources with competitive brightness and superior efficiency [2], [35]. InGaN/GaN multiple quantum well (MQW) LEDs have become mainstream solutions for green to ultraviolet applications, seeing many commercial benefits for their long lifetimes, small size, and efficiency compared to incandescent bulbs [3], [6], [17], [18].

Gallium arsenide (GaAs) was introduced in the early 1960s as one of the pioneer III-V materials for infrared LEDs and solid-state lasers [36]–[38]. For visible light emission, GaAsP and AlGaAs compounds were the first to be utilized [39], [40]. In the 1970s and 1980s, trends for high-brightness LEDs resulted in the use of AlGaAs/GaAs material compounds [39]. More recently, high-brightness LEDs have been accomplished using AlGaInP as the primary compound with emission in longer visible wavelengths from red, amber, to yellow [41], [42] with limitations exceeding wavelengths past 555 nm [39].

Nitride semiconductors became present in commercial applications in the late 1990s for emission covering the blue/green regions of the visible spectrum [43]. With a

band gap range from 0.7 eV (InN [44], [45]) to 3.4 eV (GaN [46]) the flexibility of nitride LEDs is considerably versatile, as seen in Fig. 1.1.

The use of GaN for blue and UV LEDs emerged in the late 1980s [47], [48]. The advancement of this technology was met with obstacles in regard to material quality and lack of native substrates. The growth of GaN on hetero-substrates such as sapphire results in a highly-dislocated layer, with dislocation densities on the order of 10^8 to 10^{10} cm^{-2}. This is mainly due to a substantial lattice mismatch and discrepancies in coefficients of thermal expansion [49]. Although defect densities on this order would be far too high for efficient emission in AlGaAs and GaAsP materials, GaN is applauded for its exceptional resilience to dislocations.

Figure 1.2(a) shows the construction of a typical high power LED, illustrating the various packaging complexities needed to accommodate the devices for high-power operation. The simplified material architecture for such an LED is shown in Fig. 1.2(b) for a typical InGaN/GaN MQW LED. From these two images, it is evident how self-heating in the active region can become an issue when the bulk of power dissipation is accomplished in such a small region, resulting in highly localized temperature rises.

1.1.2 High Electron Mobility Transistors

Commercial demands for high power and high frequency performance have led to an increase in the employment of wide-band gap materials in transistor applications. Si and GaAs have been the industry standard for many years with great success, but have slowly began to reach their performance limitations. The most recent record for output power density in GaAs field-effect transistors (FETs) in 2007 was 3.6 W/mm at 2-3 GHz,

marking a mild improvement over the traditional record of 1.4 W/mm at 8 GHz in 1989 [13]. GaN-based technologies, for comparison, demonstrate power densities in the range of 30 - 40 W/mm, illustrating their superiority in power applications [11], [13], [50]. The GaN power devices market is forecasted at $2.6 billion by 2022, with a compound annual growth rate of 24.5% from 2016 - 2022 [51].

As illustrated in Tbl. 1.1 before, the material properties for GaN-based transistors offer significant benefits in regard to commercial functionality. The higher power densities translate into a capability for smaller devices with competitive performance. The large breakdown field and electron mobility are also substantial in comparison to Si and GaAs devices. All of this coupled with the capability for successfully growing AlGaN/GaN heterostructures results in the achievement of high current, high voltage operation with considerable efficiency [7], [12].

The schematic for a typical AlGaN/GaN high electron mobility transistor (HEMT) structure is shown in Fig. 1.3(a) labeling the epilayers, contacts, and location of the 2-dimensional electron gas (2DEG) channel at the AlGaN/GaN interface. In its basic operation, a GaN-based HEMT is a depletion-mode, or normally-on, field-effect transistor where current flow between the source (S) and (D) ohmic contacts is governed by the field exhibited by the gate schottky contact, as demonstrated in Fig. 1.3(b) [7], [12], [13]. The stack typically consists of a non-native substrate (Si, SiC, or sapphire) onto which the nucleation layer(s), a GaN buffer layer, and AlGaN barrier layer are grown. The ohmic contact at the source and drain are typically accomplished with Ti/Al-based metals and the gate schottky contact is typically realized using Ni/Au [13].

A key mechanism in the operation for GaN HEMTs is the presence of polarized charges due to both the inherent polarity of the material and the strained AlGaN grown on top of Ga-face GaN. A dipole is created with a positive "sheet" of charge at the AlGaN-GaN interface and a negative surface charge on the top surface of the AlGaN, as depicted with (+) and (-) in Fig 1.3(b). This polarization configuration results in a large concentration of excess free-moving electrons bound within the GaN along the channel, leading to the two-dimensional electron gas (2DEG) phenomenon and ultimately the ability for high output power transistors [7], [13].

1.2 Self-heating and Thermal Management in III-N Devices

As the technology and research progress into high power and high frequency regimes, the issue of self-heating becomes of greater concern. In most cases, the device is experiencing extreme power dissipations within a small (sub-micron) region, resulting in a highly localized rise in temperature. Monitoring thermal effects in these devices becomes critical as they significantly affect the performance, reliability, and overall device lifetime. As mentioned, self-heating in LEDs leads to losses in efficiency, peak wavelength output, and reliability [5], [6], [16]–[18]. In electronic devices, losses in efficiency, power density, electron mobility, and device degradation are all a consequence of unwanted heating [7], [9], [19].

A considerable amount of research has been focused on investigating self-heating effects in III-N photonic [6], [17], [18], [20], [21] and electronic devices [9], [22]–[25], [52], utilizing a number of techniques and approaches. As the technology progresses, increased knowledge of thermal transport is crucial to advancements in device reliability and design optimization. The first step in accomplishing this is a good understanding of

the behavior of vertical heat removal from the active region into the substrate. Improvements in precise and effective characterization techniques for diagnosing and monitoring thermal behavior at the material level is crucial to these efforts. The following subsections outline the issues facing GaN-based LEDs and HEMTs with regard to self-heating and introduces a few of the techniques utilized in characterizing and monitoring temperature in these devices.

1.2.1 Self-heating in LEDs

High-brightness LEDs operate with much higher electrical compliances than their standard brightness counterparts, reaching upwards of ~5A and/or ~100V. Consequently, self-heating in the active region becomes a critical concern as it directly affects internal (and external) quantum efficiency, peak emission energy, degradation, and overall lifetime [1], [5], [17], [18]. Temperature rises in the active region, or LED *junction*, can be observed to reach upwards of ~100 °C for AlGaN and InGaN UV and blue LEDs [20], [53]. As mentioned in the sections above, the active region for these structures is very small (< 1 μm – see Fig 1.2), resulting in the majority of the resistive heating occurring within a miniscule volume and ultimately a highly localized temperature rise.

Consequently, because of the small region of interest, an effective measurement of the LED temperature rise in the junction is difficult to *directly* accomplish. The small size and complex encapsulation make it arduous for traditional temperature techniques such as RTDs and thermocouples to be applied directly to the active region. For this reason, many research efforts have begun to focus on accurate means for *indirect* junction temperature measurements.

Indirect measurements of the junction temperature can be accomplished using optical techniques, such as Raman spectroscopy [54], photoluminescence [55], and electroluminescence [18]. Apart from the considerable experimental complexities, the spectroscopic measurements which rely on the temperature-induced changes in the band gap energy suffer from competing effects due to carrier screening and bandfilling in polar III-nitride materials [39], [53].

Xi and Schubert introduced an indirect electrical method for establishing junction temperature based on the temperature-dependence of the diode forward voltage in the active region for UV GaN LEDs [17]. This method was extended and modified by Keppens et al. to demonstrate an alternative experimental technique based on similar semiconductor principles for various packaged III-V LEDs [21]. In both of these cases, temperature results were validated using the temperature-dependence of the electroluminescence (EL) peak energy via the popular Varshni band gap model [56]. However, as mentioned above, the EL method of temperature validation is not applicable to all high-brightness LEDs and additional competing electrical effects must be taken into consideration for polar materials, such as the case for InGaN/GaN MQW devices. These methods are discussed in more detail in Chapter Three.

1.2.2 Self-heating in HEMTs

Self-heating in GaN HEMTs is a significant concern, as it accounts for the majority of device degradation related to drain current and mobility losses. Since GaN-based devices are operated at large power densities, upwards of ten times higher than Si and other III-V technologies, the self-heating effects can, in turn, play a much bigger role in the loss of performance and irreversible damage in some cases [9], [19], [25], [27],

[52]. Considering this, monitoring the operating temperatures in HEMTs is an important feature of commercial production as well as materials research.

While established methods are in place for monitoring the large-scale effects of self-heating, many of the more cost-effective techniques exhibit poor spatial and depth resolution. Observation of the operating temperature in-production can be accomplished by IR thermography, where an infrared viewer is used to identify local heating, mostly on the surface of the device. This type of metrology can be revealing to major issues in fabrication design and large defects in the material. It is also a very cost- and time-effective method, as large amounts of data – and even detailed spatial maps – can be collected relatively quickly. However, the spatial resolution of this type of measurement is solely dependent on the size of the optical probe and its relation to the size of the region of interest. For the case of GaN HEMTs, this becomes an issue as a much smaller spatial resolution is required (~1 μm) and most IR systems have a resolution limit of approximately 10 μm [9], [52], [57].

Thermal measurements involving physical contact with the material can also be used to acquire an idea of local heating in semiconductor devices; Thermocouples, scanning thermal probes, and thermographic phosphors are some examples [57]. Again, spatial resolution becomes an issue as it is limited by the size of the probe and the region of interest. However, contact methods can exhibit resolution down to 100 nm in some cases. The drawback of this technique is that the device must incorporate the measurement apparatus into the packaging, and must be pre-meditated in the technology design. Another significant issue is the slow time response, which can be an issue for high-frequency devices, such as HEMTs intended for microwave applications [57].

Raman spectroscopy has become a commonly-used method for temperature measurement in GaN HEMTs and has been successfully reported by a number of groups [22], [24], [25], [27], [28], [52]. Enhanced spatial resolution on the order of 1 μm can be obtained with this technique, offering relevant information in significant regions of interest on the transistor, as well as the added ability for real-time spatial mapping during operation [25]. *Ultraviolet* Raman utilizes an excitation energy near or above the band gap of GaN, resulting in a shallow optical penetration depth in the material. This allows the region near the 2DEG to be probed directly without sacrificing lateral spatial resolution [9], [27], [28]. Since temperature rises in the 2DEG *hot spot* can reach values from 100-350 °C, the depth-sensitive attributes of this technique are significant [27], [58]. Further details of this technique and its effectiveness for monitoring temperature rise during operation in AlGaN/GaN HEMTs are discussed in Chapter Four.

1.2.3 Substrate Material Properties

In the discussion of thermal management, the material properties of the device substrate play a major role, with thermal conductivity being a key contributor. However, coefficient of thermal expansion (CTE), lattice constant, electrical resistivity, thermal boundary resistance, and cost are all important in the overall consideration of material quality and success of the technology. Table 1.2 provides a comparison of material properties for typical GaN substrates. Properties for diamond are included in the table as well, displaying a range of κ values for CVD diamond material. Values for thermal conductivity in these polycrystalline films vary as a function of layer thickness and grain size, as discussed in more detail later.

Sapphire was one of the first substrates utilized for commercial growth in GaN [59]. However, the mismatches for lattice parameters and CTE between GaN and sapphire are both rather large when compared to SiC [60]. Additionally, low thermal conductivity makes the substrate non-ideal for thermal considerations. Si and SiC are typical choices for GaN substrates in current technologies. While Si boasts a considerable advantage in cost and availability, lattice mismatch requires the introduction of seed and transition layers (e.g. AlN, AlGaN) to reduce stress, providing additional layers which contribute to the overall thermal boundary resistance of the transistor stack. Diamond offers apparent benefits in thermal conductivity, but similar to traditional substrates, exhibits non-ideal qualities in lattice mismatch and CTE. Precise investigations of the material thermal properties are necessary for furthering the development of substrate thermal management improvements.

Table 1.2. Comparison of material properties for various GaN substrate materials. Compiled from [61]–[65]. * Large range in κ for CVD diamond [66], [67].

	Sapphire	Si	6H-SiC	Diamond	AlN	GaN
Thermal conductivity, κ (W/mK)	27	149	490	~10 - 1800*	290	130
Lattice constant (Å)	4.758	5.431	3.08	3.567	3.112	3.189
Coefficient of Thermal Expansion (10^{-6}/K at 300 K)	6.66	2.6	4.3	1.5	4.15	5.59

1.2.4 Thermal Boundary Resistance

One of the principal barriers for thermal management in devices consisting of hetero-epitaxial layers is the tendency for interfaces to inhibit the flow of heat from the active layer(s) into the substrate. Thermal boundary resistance (TBR) describes this

process of impedance from efficient vertical heat dissipation at an interface. In most discussions, the cause of an effective TBR is attributed to intrinsic "resistances" in the device interlayers and defects at the material interface. For a temperature difference ΔT and heat flow q through an area A, $TBR = (\Delta T \cdot A)/Q$, with units m^2K/W [68]. Fig 1.4(a) shows a simple sketch of how the resistances in individual layers and TBR at the interface contribute to a combined effective thermal resistance for the stack. Additional contributions to TBR for GaN-substrate interfaces are illustrated in Fig. 1.4(b). These mechanisms include phonon scattering at the transition layer interfaces, scattering at dislocations, point defects, and other imperfections and disorder at the GaN-substrate interface [69].

TBR has been the focus of many studies in GaN for both photonic and electronic device materials. In many cases, the magnitude of the TBR is device-specific and depends heavily on the growth method, material layers, compositions, doping concentration, and ultimately the thermal characteristics of the substrate. These existing variables have caused considerable discrepancy in reported values for TBR in GaN literature, especially between theoretical expectations and experiment.

For GaN on SiC substrates, predicted values as low as 10^{-9} m^2K/W have been established [26]. However, the experimental measurements of this value exhibit a larger range from ~ 1×10^{-8} [70], [71] to 1.2×10^{-7} m^2K/W [26], [72]. Similarly for GaN-on-Sapphire, the experimental measurements range from $1 – 5 \times 10^{-7}$ m^2K/W, much higher than the predicted 10^{-9} m^2K/W [26]. For GaN-on-silicon, experimental values in the literature for TBR range from ~7×10^{-9} to ~7×10^{-8} m^2K/W [26], [72]. Again, calculations of the TBR for Si provide much lower values on the order of 10^{-9} [58]. The

large discrepancy in values is mainly attributed to lack of a theoretical approach taking into account case-specific variations, e.g. variations in transition layer compositions, nucleation formations, lattice mismatch, defect concentrations and imperfections at the interface [26], [58], [73].

Incorporating diamond as a substrate for GaN has seen similar obstacles for overcoming TBR. These materials exhibit a comparable, yet competitive, range for TBR from ~$3 – 5 \times 10^{-8}$ [69], [70], [74] to ~1×10^{-7} m2K/W [75]. Similar to other substrates, the TBR in GaN-on-diamond is typically attributed to the acoustic mismatch between materials, the diamond seeding interlayer, and the defective region at the initial growth regime of the diamond nucleation layer [76].

1.3 Diamond

Diamond has recently gained attention in the electronic world as thermal management begins to motivate the progress of technologies. As a bulk material, diamond has one of the highest reported thermal conductivities (2000 W/mK) [29]. Other appealing material properties are its large mechanical hardness, low coefficient of thermal expansion, and low electrical conductivity.

Efforts have been successful at achieving high-quality synthetic single-crystal diamond in the laboratory [77]. While the thermal properties of these materials are appealing, the applications are typically industrial and not seen in electronics. GaN on single-crystal diamond studies have been reported, however the substrate size and scalability are not ideal for device applications [78], [79]. The development of diamond

growth by chemical vapor deposition (CVD) has opened many doors in this regard, with capabilities for large area deposition and high-quality thin films.

1.3.1 Chemical Vapor Deposition

Original methods for producing synthetic diamond involve high-temperature high-pressure (HPHT) processing. These techniques were useful at introducing diamond into numerous new mechanical applications not commercially accessible to natural diamond. The eventual introduction of chemical vapor deposition (CVD) brought forth a diverse range of functionalities for diamond with its ability for higher-yield, thin film large area growth, and free-standing plates or substrates.

CVD diamond growth is accomplished by the introduction of carbon atoms to pre-existing diamond material (typically in the form of micro-particles or diamond *seeds*) on the growth surface to form a tetrahedrally-bonded carbon structure. The carbon source for the process is provided by a gas mixture, typically hydrogen and methane. An energy source at the surface (microwave plasma or heated filament) is utilized to promote the dissociation of the gas molecules for deposition of carbon atoms on the wafer. Growth temperatures are typically ~700 – 900 °C, provided via microwave plasma or thin current-driven filaments – hot filament CVD (HFCVD).

A major achievement in the growth of diamond via CVD is the ability to encourage the production of the carbon diamond allotrope and avoid the propagation of graphite or other more-stable forms of carbon at the surface. This is accomplished, largely, by the introduction of atomic hydrogen at the surface. The hydrogen works to

etch graphite during the reaction to promote the growth of diamond sp^3 bonds and suppress the graphitic formation.

CVD diamond is polycrystalline. While this provides an advantage in its abilities to cover large surface areas with considerable thickness uniformity, the effects have been observed as a contributing limitation in the applications addressing thermal conductivity. Variations in grain size and a high density of grain boundaries introduce a number of obstacles for in-plane thermal transport. Surface roughness is another issue often viewed as a limitation for use in device heat-spreading films. However, efforts involving the incorporation of multi-step CVD processing (i.e. microwave-enhanced, followed by hot filament CVD) have been seen to mitigate some of these concerns [26].

1.3.2 Diamond as a Heat-spreading Substrate

Processes for incorporating diamond substrates into GaN device layers have been successful in accomplishing full standalone wafers with sizes up to 100-mm. Figure 1.5(a) displays GaN-on-diamond wafers of varying sizes. Initial efforts for fabricating a GaN-on-diamond wafer involved the physical bonding of GaN HEMT layers to a diamond wafer substrate [29], [65]. In this technique, a device-ready GaN-on-Si wafer is first bonded face-down to a sacrificial carrier wafer. The original growth substrate is then removed from the GaN HEMT layers by means of wet chemical or dry etching processing. The now exposed GaN epi-layer surface is treated with a dielectric coating (nanometer-thin) to encourage the facilitation of the subsequent bonding of the GaN-on-carrier wafer to a CVD diamond wafer. Following the removal of the carrier wafer, the process results in a GaN-on-diamond wafer [29], [33], [65], [80].

Several groups have reported on considerable success with this technique for incorporating a good thermal conducting substrate and the ability to maintain the quality of the GaN epilayers during the transfer process [29], [65]. In Ref. [65], the group demonstrates the potential of GaN-on-diamond at heat extraction compared to other substrates. They report a reduced rise in temperature ~ 100 °C when compared to GaN-on-SiC and suggest an improvement in the vertical thermal impedance by ~58% for GaN-on-diamond.

More recent fabrication processes involve the direct growth of CVD diamond on the GaN HEMT material stack [76], [81]. In this technique, the initial nitride layers are grown by MOCVD on a silicon substrate. Figure 1.5(b) illustrates this process. The GaN-surface of the wafer is bonded to a sacrificial handle wafer and the silicon substrate is removed in a similar fashion to the technique described above. Additionally, the nitride transition layers (e.g. AlGaN, AlN) are also removed. A thin dielectric layer (~30 nm) is then deposited on the exposed GaN surface to facilitate diamond seeding. Typical material for this seeding layer is SiNx [76], [82], [83]. Finally, diamond is deposited using hot-filament or microwave-enhanced CVD. After the removal of the handle wafer, the result is a standalone GaN-on-diamond wafer.

These techniques have proven successful for wafer scale-up to sizes reaching 100 mm [29]. With substrate thicknesses typically < 100 μm, the extension to wafer diameters this size offers a number of technical hindrances, namely wafer bow and warping which lead to cracking or breakage. In Ref. [29], the most common step in the fabrication process for which wafer fracture was observed was following the atomic bonding of the GaN-carrier to CVD diamond wafer.

With the GaN-on-diamond technology in an early, yet promising, state, thorough characterization of material quality and thermal properties for these materials is crucial to its potential. Chapters Five, Six, and Seven will touch on efforts involving the investigations of CVD diamond in its applications to GaN-on-diamond applications.

1.4 Dissertation Overview and Research Objectives

The aim of this work is three-fold: (1) to introduce the success and potential growth of III-nitride technology and its overwhelming presence in industry and academic research; (2) to present the reader with the current issues facing high-power and high-frequency III-nitride devices in regard to heat production and the need for thermal management solutions to further the progress of these technologies; (3) to demonstrate the effectiveness of experimental characterization techniques at monitoring and identifying these thermal effects in III-nitride devices and materials, as well as substantiate the significance of these studies for the future developments in III-nitride research and industry applications.

In Chapter Two, an overview of the measurement and characterization techniques utilized in this work are presented. The basics of Raman and photoluminescence spectroscopies are detailed with a discussion of their applicability to studies of III-nitride materials. [Scanning electron microscopy (SEM) and transmission electron microscopy (TEM) are overviewed with a demonstration of their usefulness in analysis of III-nitride thin-films.] Methods and accomplishments in the context of data analysis and simulation will also be described in some detail, highlighting finite element (FE) analysis and optimization data-fitting techniques for appropriate error propagation in the presentation of experimental data.

In Chapter Three, an optical and electrical investigation of self-heating in InGAN/GaN LEDs will be described. The focus of this study is to present the shortcomings of optical methods for accurately determining the junction temperature in high-brightness LEDs due to competing effects such as band-filling and carrier screening in polar III-nitride materials. The bulk of this work has been published in Ref. [53].

Chapter Four highlights efforts involving the examination of self-heating in AlGaN/GaN high electron mobility transistors. Ultraviolet and visible micro-Raman spectroscopy is used to measure temperature rises in the various materials of the device during operation to establish a vertical temperature profile throughout the epi-layer stack. The bulk of the experimental work and analysis in this chapter was performed in close collaboration with Dr. Mohammad Nazari, the results of which are, in part, reported in Ref. [58] for which Dr. Nazari was the principal author.

In Chapter Five, various studies involving the characterization of CVD diamond are presented. Investigations of the lateral thermal conductivity in CVD diamond thin films on silicon using micro-Raman are demonstrated. The details of analytical tools and simulations used in fitting data and extracting accurate thermal conductivity and TBR values are also discussed.

Chapter Six presents a study of stress distributions in a GaN-on-diamond wafer. Mapping of stresses across a full 75-mm GaN HEMT-on-diamond wafer are accomplished using UV and visible Micro-Raman spectroscopy. Results from simulations are also discussed, incorporating the role of threading dislocations at the GaN-diamond interface in local stress relaxation along the growth direction of the GaN buffer layer. Much of this work has been reported in [84].

In Chapter Seven, photoluminescence (PL) spectroscopy is utilized to accomplish full-wafer stress mapping across the same 75-mm GaN-on-diamond wafer. Similar to results from Raman, unexpected stress uniformities are observed. Results from simulation are presented with discussion of the variations in threading dislocation density along the growth direction of the GaN. The bulk of this study has recently been submitted for publication.

Chapter Eight provides a summary of the dissertation and addresses conclusions of the work overall with suggestions for future research.

1.5 Figures

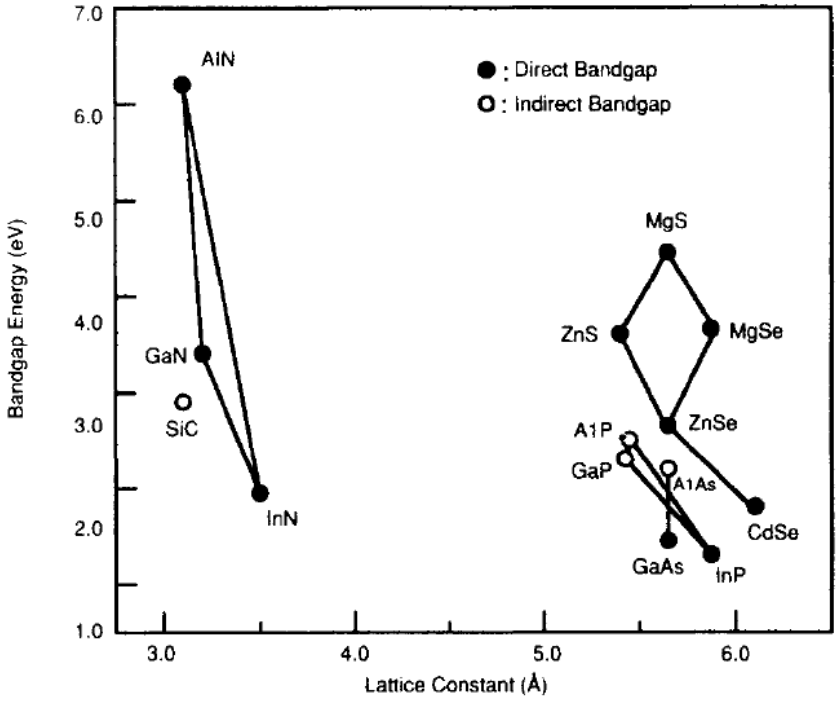

Figure 1.1. Plot of band gap energy as a function of lattice parameter. The plot shows a comparison of band gap energies and lattice parameters for a number of semiconductor materials, demonstrating the versatility of nitride-based compounds in the energy spectrum [85].

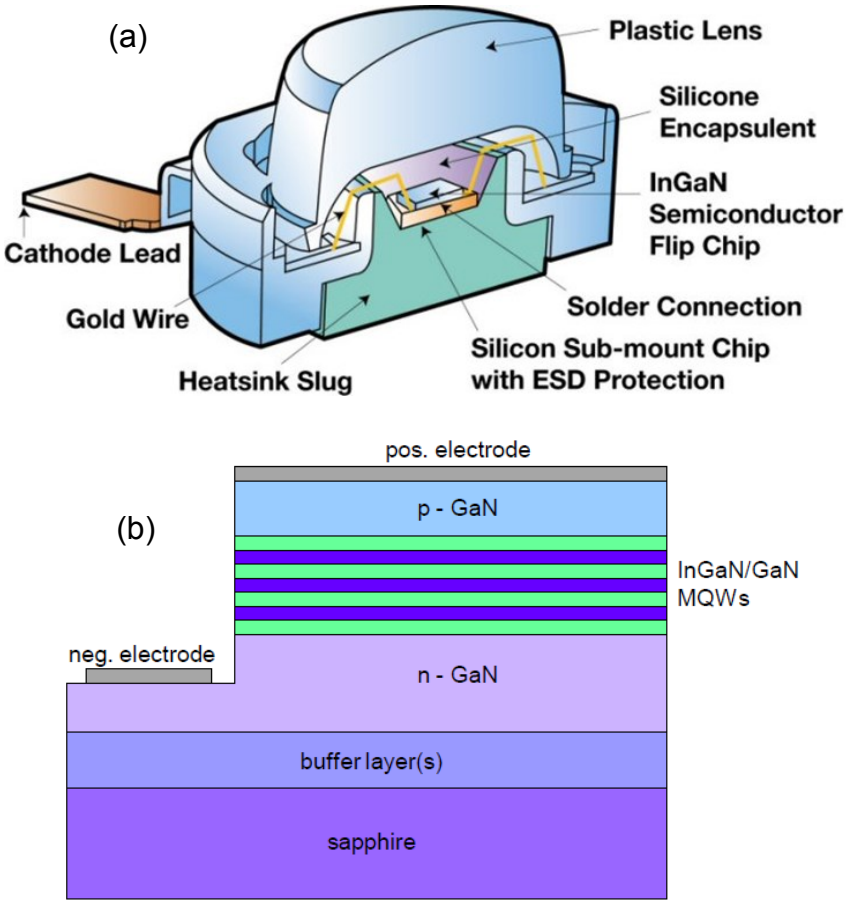

Figure 1.2. Structure of a high-brightness LED. (a) Example of typical high power LED construction with labels for various parts of packaging and encapsulation. (*Courtesy: Lumileds*) (b) Illustration of material layers present in an InGaN/GaN multiple quantum well LED; adapted from [86].

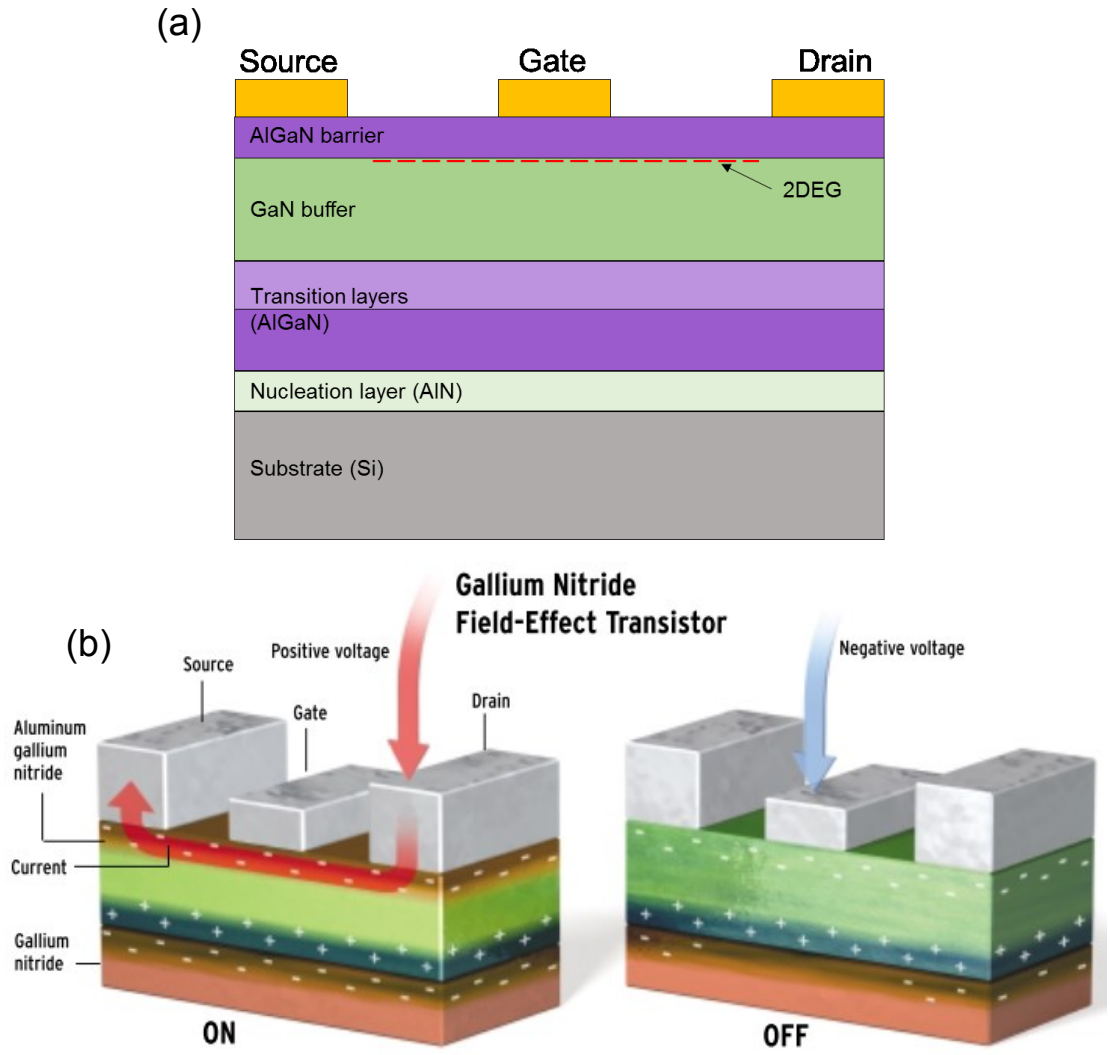

Figure 1.3. Structure of an AlGaN/GaN HEMT. (a) Cross-section for an AlGaN/GaN high electron mobility transistor with key materials labeled and the position of the 2DEG. (b) Illustration of an AlGaN/GaN HEMT during operation for a small gate bias (left) and large gate bias (right) demonstrating the normally-on mode of operation [7].

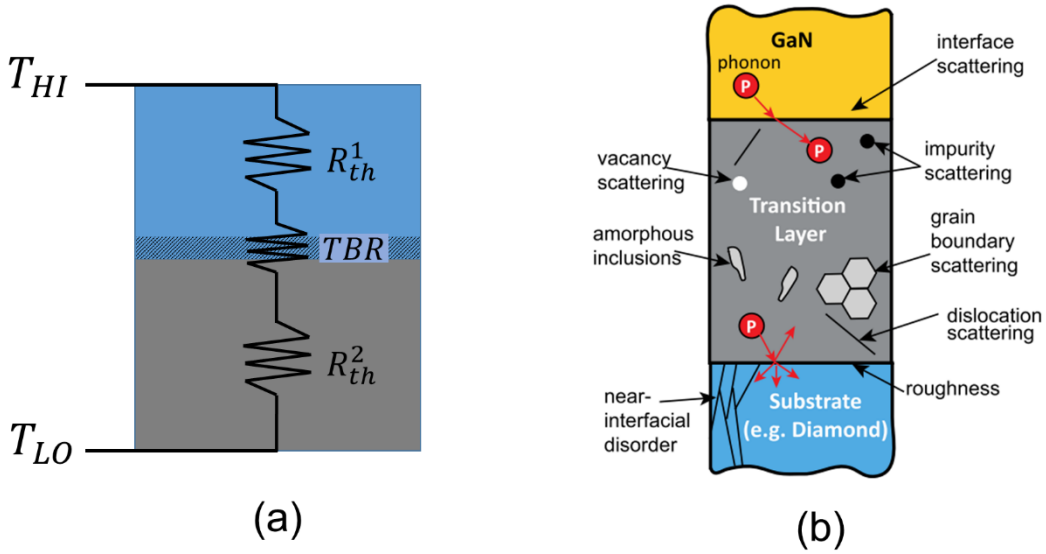

Figure 1.4. Thermal boundary resistance. (a) Drawing depicting circuit analogy for thermal resistances in two materials and thermal boundary resistance (TBR). (b) Illustration of mechanisms contributing to thermal resistances between the GaN layer and substrate [69].

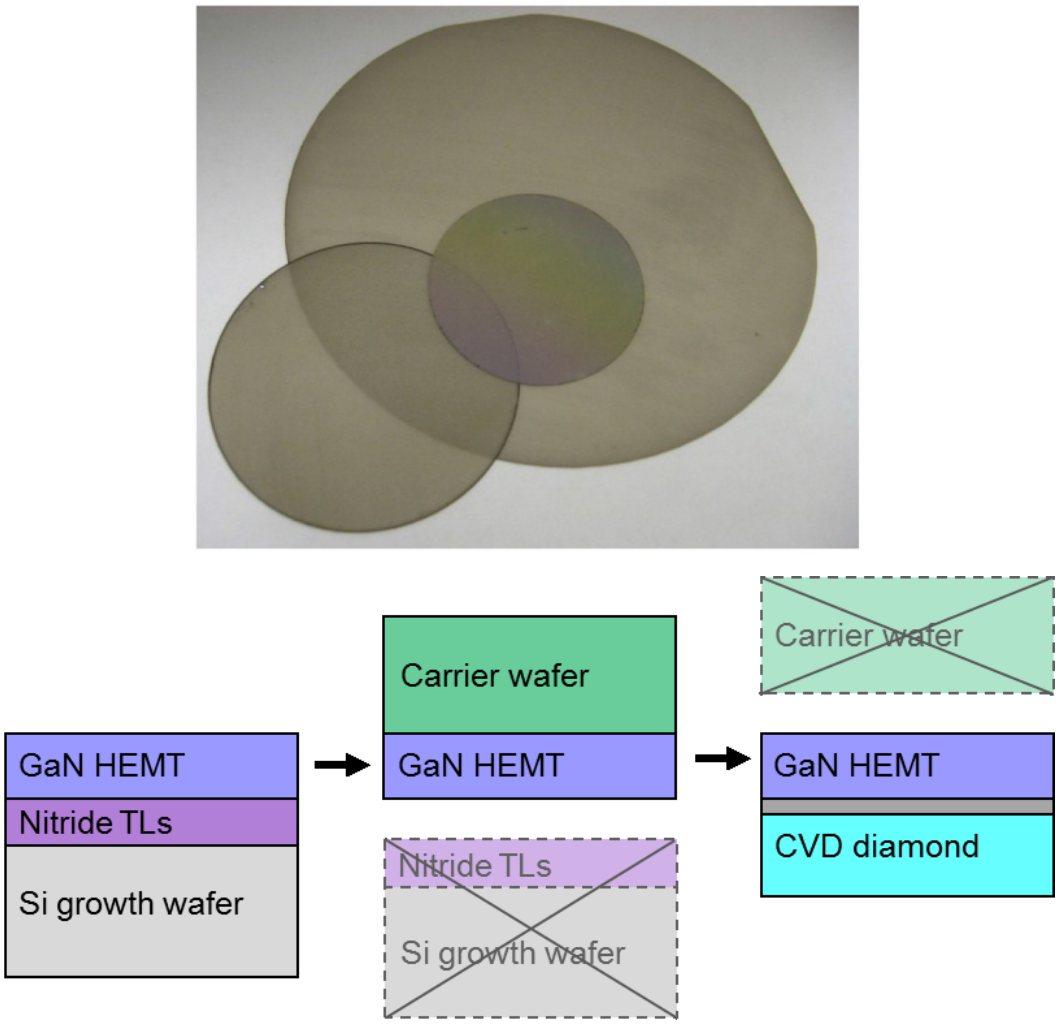

Figure 1.5. GaN-on-Diamond wafers. (a) Photograph of several GaN-on-diamond standalone wafers of varying sizes, up to 100-mm [29]. (b) The fabrication process for producing GaN-on-diamond wafers. An HEMT on Si is first bonded to a carrier wafer and Si substrate and nitride transition layers (TLs) removed. A seeding layer is deposited on the exposed GaN and diamond is grown via CVD prior to removing the carrier wafer; Adapted from [29].

2. CHARACTERIZATION, MEASUREMENT, AND ANALYSIS TECHNIQUES

In this chapter, a brief overview of the experimental methods and data analysis techniques pertinent to the studies in this dissertation will be presented. Details regarding standard equipment employed and typical measurements for each of the approaches will be provided. An overview of the applications relevant to self-heating and materials characterization in III-nitrides is also discussed along with a brief review of the underlying theory.

2.1 Raman Spectroscopy

Raman spectroscopy is a non-contact, non-destructive optical technique boasting a number of uses in materials characterization with applications ranging in scope from biomedical [87] to homeland security [88]. As a characterization tool, Raman is useful at identifying unknown materials, assessing material quality, and obtaining information regarding physical changes in material systems such as changes in temperature, stress/strain, and composition. In bulk semiconductors and thin films, Raman and micro-Raman have become extremely useful in these experimental applications.

A number of experimental variations have arisen for Raman spectroscopy. Micro-Raman spectroscopy, or *Raman microscopy*, incorporates the use of excitation and collection using a microscope objective for analysis of small samples and thin films with noteworthy spatial resolution (~1 μm). Variations in collection geometry are seen, including off-axis, 180° backscatter, and transmission, depending on the sample and objectives of the experiment. As the signal from Raman is inherently weak in comparison to the laser intensity, excitation focus and collection efficiency are critical in these

measurement [89]. For the studies in this work, Micro-Raman using a backscatter geometry is utilized exclusively. Other popular techniques for Raman include confocal microscopy [90], time-resolved [9], resonance Raman, surface-enhanced Raman spectroscopy (SERS) and surface-enhanced resonance Raman [91], and tip enhanced Raman spectroscopy (TERS) [92], to list a few.

Raman spectroscopy relies on the inelastic scattering of photons with lattice vibrations, or phonons, in the material. When light at a frequency ν_0 is incident on a material, the majority of light is scattered elastically and results in the same energy as the source, ν_0, termed *Rayleigh scattering*. A very small portion (~10^{-5} of the incident intensity) of the scattered light is attributed to *Raman scattering*, and is observed at a frequency $\nu_0 \pm \nu_m$, where ν_m is a vibrational frequency of the lattice [89], [93]. The energies at $\nu_0 - \nu_m$ and $\nu_0 + \nu_m$ are described as the *Stokes* and *Anti-Stokes* shifts, respectively. By measuring the energy of the scattered photon, and determining the amount of energy by which ν_0 has been shifted, the energy of the particular lattice vibration mode involved in the interaction, ν_m, can be determined, denoted the *Raman shift* for that phonon. Measurement of the Raman shift energy yields insight into information concerning the vibrational states in the material. This scattering phenomenon was first discovered by C. V. Raman in 1928 [94].

A typical setup for Raman spectroscopy is illustrated in Fig. 2.1. Laser excitation and collection of the Raman signal are accomplished through an objective and focused on the surface of the sample in question. Reflective and focusing optics are utilized to direct the collected beam and focus the signal through the entrance slit of the spectrometer. To exclude unwanted signal from the laser, a holographic notch filter is implemented,

capable of precisely eliminating light at the laser wavelength from the collected scattered signal. Once the collected signal enters the spectrometer, the light is dispersed by a diffraction grating and directed toward the exit slit at the specified wavelength, near the initial excitation wavelength of the laser. Variations in signal detection exist, with most common approaches being the photomultiplier tube (PMT) and charge-coupled device (CCD) array detectors. For the experimental studies in this work, a liquid nitrogen-cooled CCD detector was used for all investigations. Figure 2.2 shows examples of typical Raman spectra collected for (a) silicon, (b) GaN, and (c) diamond.

2.1.1 Raman Applications

Micro-Raman has proven to be useful in the determination of temperature rise for semiconductor materials with many applications in research as well as industry. For III-nitrides specifically, many groups have found the utilization of Raman thermography beneficial for investigating device self-heating [24], [27], [28], [95].

Experimentally, temperature rises are determined from changes in the measured phonon peak energy and linewidth in the Raman spectrum. For GaN, an increase in temperature results in a red-shift in the phonon peak and linewidth broadening. This is due largely to thermal expansion of the lattice and phonon decay through anharmonic interactions resulting in changes in the observed Raman phonon spectra [96]. The temperature dependence of the phonon energy $\omega(T)$ can be described by

$$\omega(T) = \omega_0 - \Delta_1(T) - \Delta_2(T), \tag{2.1}$$

where ω_0 is the initial phonon energy, Δ_1 represents the thermal expansion contribution, and Δ_2 describes the phonon decay interactions [96].

For the temperature range addressed in the studies for this dissertation, the dependence in Eq. 2.1 can be simplified for the experimental determination of temperature rise (ΔT) due to changes in the phonon peak position, $\Delta\omega = \omega - \omega_0$ by

$$\Delta\omega = k_R \Delta T \,, \tag{2.2}$$

where k_R is the Raman temperature coefficient [58], [97]. This value is material- and phonon-specific and can be determined through calibration of the sample by controlling the ambient temperature and observing the behavior of $\Delta\omega$ over a particular temperature range. For GaN, temperature rise can be determined from the E_2^2 (ω_0 ~ 567 cm-1 [58], [98]) and A_1(LO) (ω_0 ~ 740 cm-1 [58], [98]) phonons with coefficients k_R^{E22} ~ -0.02 cm-1/K and k_R^{A1LO} ~ 0.03 cm-1/K [97].

Raman spectroscopy has also proven useful at identifying changes in stress. In the discussion of semiconductors this technique is valuable as residual stress impacts many aspects concerning material quality and future device viability on the material. A number of research efforts have been focused on experimental characterization of stresses in III-nitride materials using Raman spectroscopy [99]–[103].

Similar to Raman thermal measurements, mechanical stresses, σ, in the material are determined by observed changes in the measured phonon frequency ω and can be described by the relationship

$$\Delta\omega = a'(\sigma_{xx} + \sigma_{yy}) + b'\sigma_{zz} \pm c' \left[(\sigma_{xx} - \sigma_{yy})^2 + 4\sigma_{xy}^2 \right]^{1/2} \,, \tag{2.3}$$

with σ_{ij} denoting stress in the ij plane. The coefficients a', b', and c' are termed phonon stress deformation potentials with units cm^{-1}/GPa which are material- and phonon-specific [104]. For the majority of the experimental work with device materials, Eq. 2.3

can be simplified under the assumption that deformation occurs freely in the z-direction (σ_{zz} = 0) and that shear stress, represented by σ_{xy}, can be neglected for measurements involving mostly planar materials far from edges and structures. The final term in Eq. 2.3 can also be neglected due to the small impact of device asymmetry [104]. From this, the combined the relationship becomes:

$$\Delta\omega = a' \cdot \left(\sigma_{xx} + \sigma_{yy}\right), \tag{2.4}$$

For the case of biaxial stress ($\sigma_{xx} = \sigma_{yy}$), Eq. 2.4 can be simplified further to $\Delta\omega = k_S \cdot \sigma_{xx}$, where k_S is termed the Raman stress/pressure coefficient in units cm^{-1}/GPa. For GaN, the in-plane biaxial stresses are most pertinent to applications in this study. Stresses can be determined for the E_2^2 phonon with k_S^{E22} ~ -3 cm^{-1}/GPa and using the A_1(LO) phonon with k_S^{A1LO} ~ -2 cm^{-1}/GPa [84], [97], [101], [103], [104]. The relationship between in-plane stress σ_{xx} and strain ε_{xx} in the GaN crystal can be determined by

$$\sigma_{xx} = [(C_{11} + C_{12}) - 2C_{13}^2/C_{33}]\varepsilon_{xx}\ , \tag{2.5}$$

where the term in brackets encompasses the biaxial modulus for GaN comprised of the C_{ij} elastic constants with values: C_{11} = 390 GPa, C_{12} = 145 GPa, C_{13} = 106 GPa, and C_{33} = 398 GPa, resulting in a modulus of ~ 478 GPa [23], [103]. The out-of-plane strain, ε_{zz}, can be obtained by $\varepsilon_{zz} = -(2C_{13}/C_{33})\varepsilon_{xx}$ [105].

2.2 Photoluminescence

Photoluminescence (PL) spectroscopy is a non-destructive, non-contact, optical characterization technique, useful in the investigation of optical and electronic properties in materials research. In semiconductors, it is a useful tool for estimating band gap and

material properties which affect the near-band edge states. Because of exceptional optical properties in GaN, PL has proven to be a powerful means for experimental determination of material quality, temperature, and stress in III-nitrides research [99], [102], [106]–[109]. The lateral spatial resolution also provides for opportunities in detailed mapping capabilities.

In the simplest of terms, photoluminescence is an optical process in which light is emitted from a material as a result of the absorption of incident light. In semiconductors, this occurs when the incident light is of an energy (E) higher than that of the energy band gap (E_g) of the material. The initial absorption of a photon with $E > E_g$ causes the creation of an electron-hole pair through the promotion of an electron into the conduction band. From this state the excited electron (hole) begins relaxation to energies lower (higher) in the conduction (valence) band through a process referred to as thermalization, in which excess energy is transferred to the lattice in the form of phonons. Finally, recombination of the electron-hole pair results in the release of a photon with energy approximately equal to the energy separation of the band gap for the material.

This process reveals a great deal of information regarding the band structure of the material. As radiative recombination can occur at defect sites in the crystal as well, PL spectroscopy is also very valuable for obtaining insight into material quality, revealing details concerning defect composition and concentration. The rate at which these recombination processes occur can also provide important information about the material using time-resolved photoluminescence [110].

For the studies in this work, the experimental setup for PL measurements consist of a diode-pumped Ti:Sapphire femtosecond laser with 8MHz repetition rate, frequency-

tripled to 291 nm, for the excitation source. Excitation and collection are accomplished using a 15X all-reflective objective with 0.4 NA to focus the laser light onto the sample with typical spot diameter of ~10 μm. PL spectra is collected using a 0.64-m spectrometer with a microchannel plate photomultiplier as the detector. Figure 2.3 shows typical PL spectra for GaN from a HEMT device. This is similar to spectra measured in Chapter Seven for AlGaN/GaN HEMT layers on diamond.

2.2.1 Measurements of Stress using PL

Photoluminescence has been well-established as a viable technique for determining stresses in semiconductor materials, with considerable applications in GaN [99], [102], [109]. In-plane stress, σ_{xx}, is determined from shifts in the measured peak position, E, in the PL spectrum, representing changes in the energy band gap, E_g. A stress factor, k_{PL}, is utilized to evaluate the stress-energy relationship [103], [107], [109]:

$$\sigma_{xx} = (E - E_0)/k_{PL}\,, \tag{2.6}$$

where E_0 represents the strain-free PL peak energy, where $\sigma_{xx} > 0$ corresponds to a tensile stress. For GaN, k_{PL} = 21.1 ± 3.2 meV/GPa and E_0 = 3.4180 ± 0.0008 eV [103], [107].

2.3 Data Analysis and Simulation

The following gives a brief introduction to some of the techniques used in this work for analyzing experimental results by means of modeling, simulation, and data fitting.

2.3.1 Finite Element Analysis

Finite element (FE) analysis is the concept of simplifying large or multi-body problems by the discretization of the system into a composition of *finite elements*. From this approach the physics can be addressed in each element and extrapolated across the complete system to arrive at a solution to the original problem. This technique has proven useful at simplifying complex boundary value problems in physics and engineering since its introduction in 1956 [111]. Through the use of simulation software, this capability has gained more widespread use in its applications in research and industry.

In a typical FE analysis, the system is divided into discrete elements by means of a *mesh*. Calculations are then performed at the intersection *nodes* of each mesh element. Figure 2.4(a) shows an example of a FE simulation model using COMSOL Multiphysics, demonstrating the meshing technique and resulting simulated results for temperature rise in the model. Depending on the model and the objectives of the simulation, a number of concurrent calculations at each mesh element can be performed by the software ranging from simple kinetics (force, friction, displacement) to electrodynamics (EM fields, current, voltage). Complexities can even be addressed in regard to *multiphysics* problems, e.g. joule heating from current-induced temperature rises. For the studies in this work, heat transfer and solid mechanics are utilized the most to investigate thermal transport and mechanical/thermal stresses in the material.

Figure 2.4(b) shows an example of a two-dimensional FE model used for simulating thermal expansion in GaN-on-diamond layers during fabrication, as discussed in Chapter Six.

2.3.2 Data Fitting and Optimization

Finite element modelling is also very useful in fitting experimental data to predicted models to extract specific material properties from the simulation. For the study presented in Chapter Six, the fabrication process for producing GaN-on-diamond wafers was simulated. Thermal stresses were modeled for each step of the process, as discussed in the chapter. A stress relaxation parameter, f, was introduced into the material to describe effects of threading dislocations on the elastic properties of the GaN by $E = (1 - f)E_{bulk}$.

To establish a value for f, a parameterization was utilized. In this approach, the simulation is compiled, sweeping the values of f for each run. This approach is repeated until a reasonable agreement is seen between the experimental and simulated values for stress in the GaN. This parametric sweep is demonstrated in Fig. 2.5 for a number of simulation cycles. More details of this specific simulation are explained in Chapter Six.

For the study presented in Chapter Five, FE simulations are used to validate the assessment of thermal conductivity, κ, from Raman measurements. For this a two-dimensional simulation was employed to model the temperature profile for heat transfer in diamond membrane samples. Optimization capabilities in the FE software were utilized to fit the experimental Raman data and extract values for in-plane κ and thermal boundary resistance (TBR) between the diamond and silicon substrate. The optimization technique incorporates a Monte Carlo algorithm for minimizing a particular objective function in the model. For the case of this study, the objective function used was the chi-square (χ^2) fit between the experimental and simulated phonon shift, $\omega(x)$ across the

diamond layer. The Monte Carlo algorithm runs repetitive cycles of the simulation, adjusting the fitting parameters (κ and TBR), until reasonable agreement between the data and simulation are achieved. As a result, the simulation results in optimized values for the fitting parameters κ and TBR, as well as a value for the χ^2 agreement.

The chi-square minimization provides a measure of *goodness of fit* between a collection of expected results and observed results. For a set of measurements comparing a plot of observed results $(x_i, y_i \pm \delta y_i)$ to a theoretical objective function $f(x_i, a, b, \dots)$ – where $a, b, \dots$ represent fitting parameters – chi-square (χ^2) can be mathematically described as

$$\chi^2 = \sum_{i=1}^{n} \left(\left(y_i - f(x_i) \right) \Big/ \delta y_i \right)^2 . \tag{2.7}$$

The *reduced* chi-square is determined by $\tilde{\chi}^2 = \chi^2/(d-1)$, where d represents the degrees of freedom, which for data-fitting d = (number of data points) – (number of fitting parameters) [112].

This approach is also useful as it provides a means of validating uncertainty in the simulated values through statistical confidence intervals, as detailed in Chapter Five discussion.

2.4 Figures

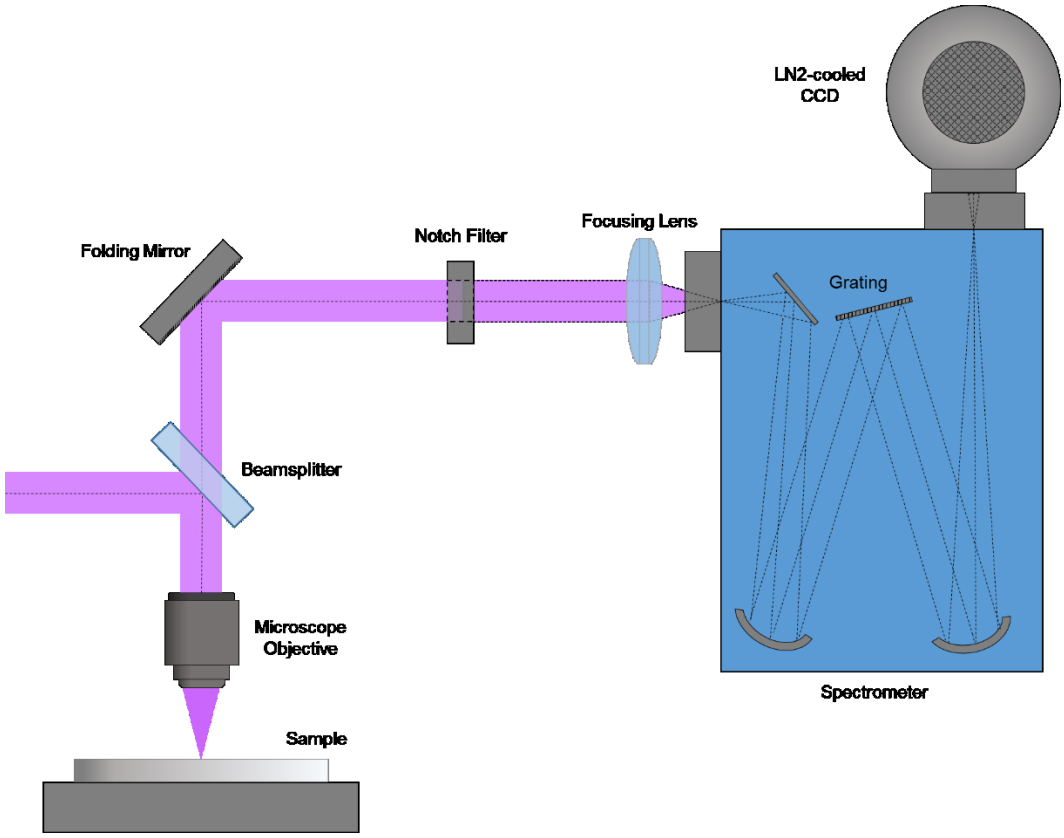

Figure 2.1. Experimental setup for Raman spectroscopy. Schematic of a typical micro-Raman spectroscopy setup, incorporating reflective and refractive optics for directing and focusing, microscope objective, notch filter, single diffraction grating, and CCD detector cooled by liquid nitrogen (LN2).

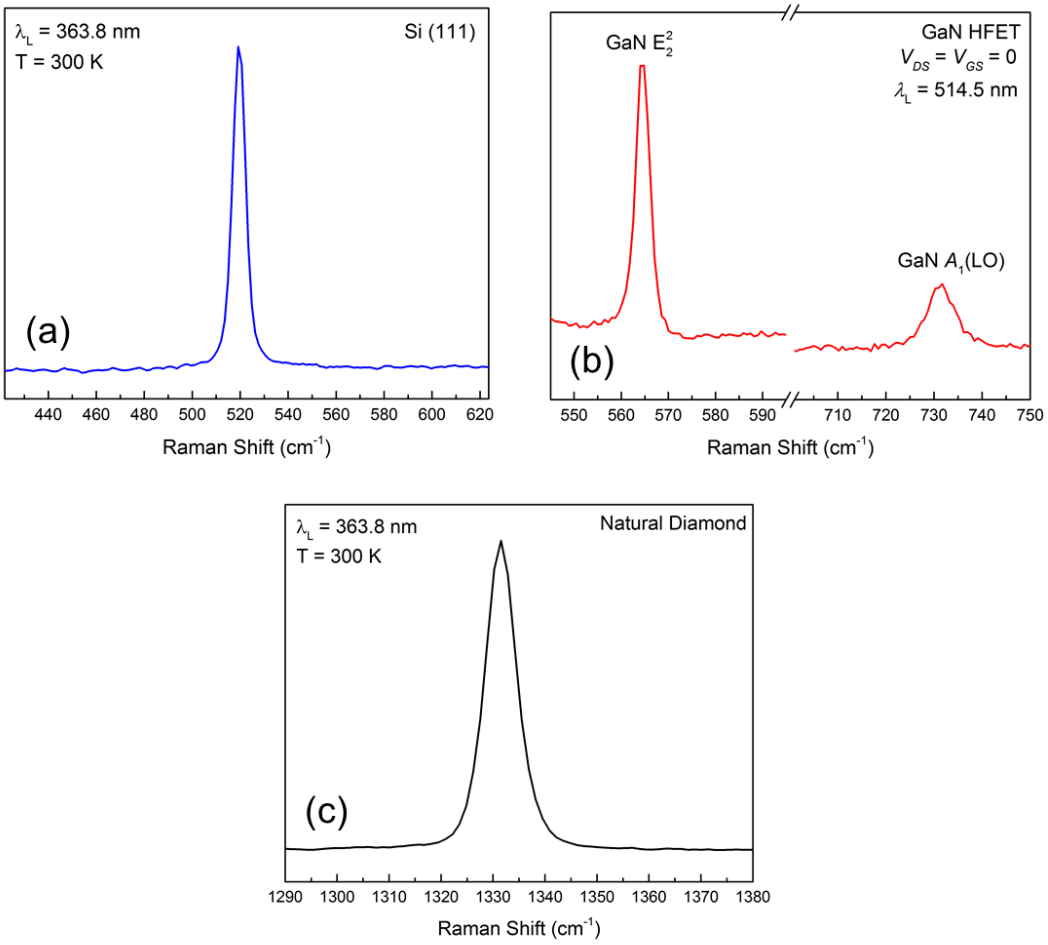

Figure 2.2. Typical Raman spectra. Typical Raman spectra are shown for (a) silicon, (b) GaN from an AlGaN/GaN HEMT device, and (c) natural diamond.

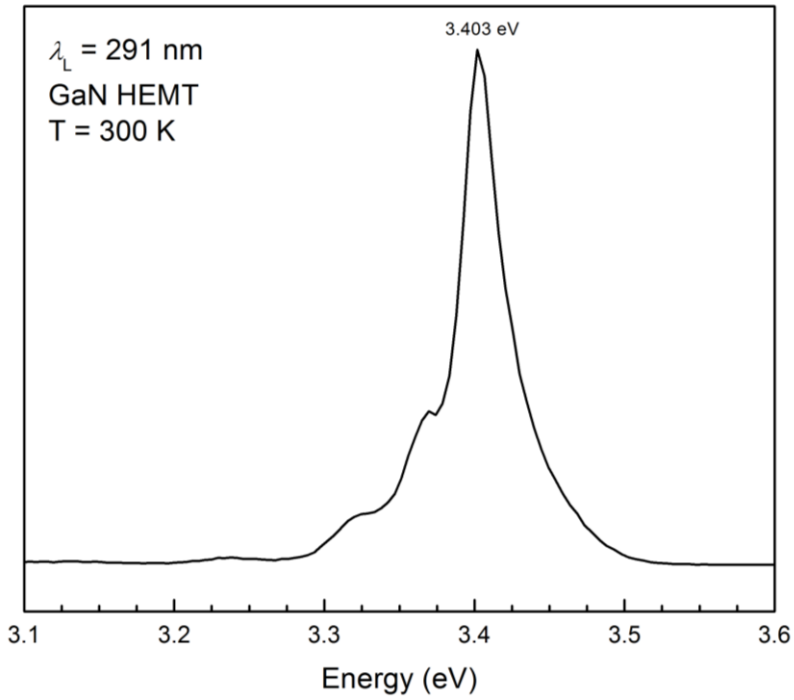

Figure 2.3. GaN photoluminescence spectrum. Spectrum showing GaN PL from an AlGaN/GaN HEMT test structure sample.

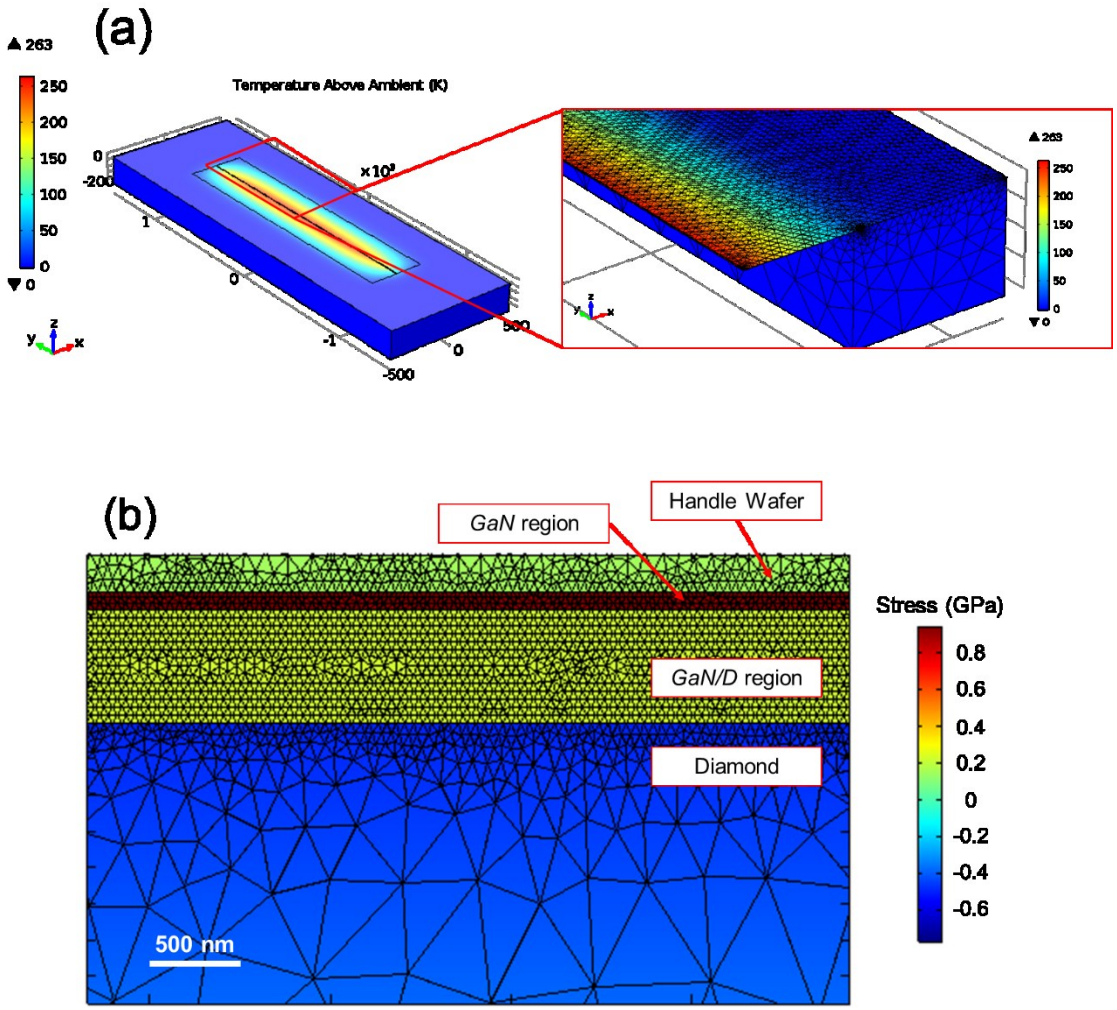

Figure 2.4. Finite element models. (a) Three-dimensional finite element simulation for diamond thin film membrane on silicon discussed in Chapter Five. The magnified image displays the model in quarter symmetry to illustrate the complexity of the meshing. (b) Two-dimensional model, discussed in Chapter Six, for GaN-on-diamond simulations of thermal stress.

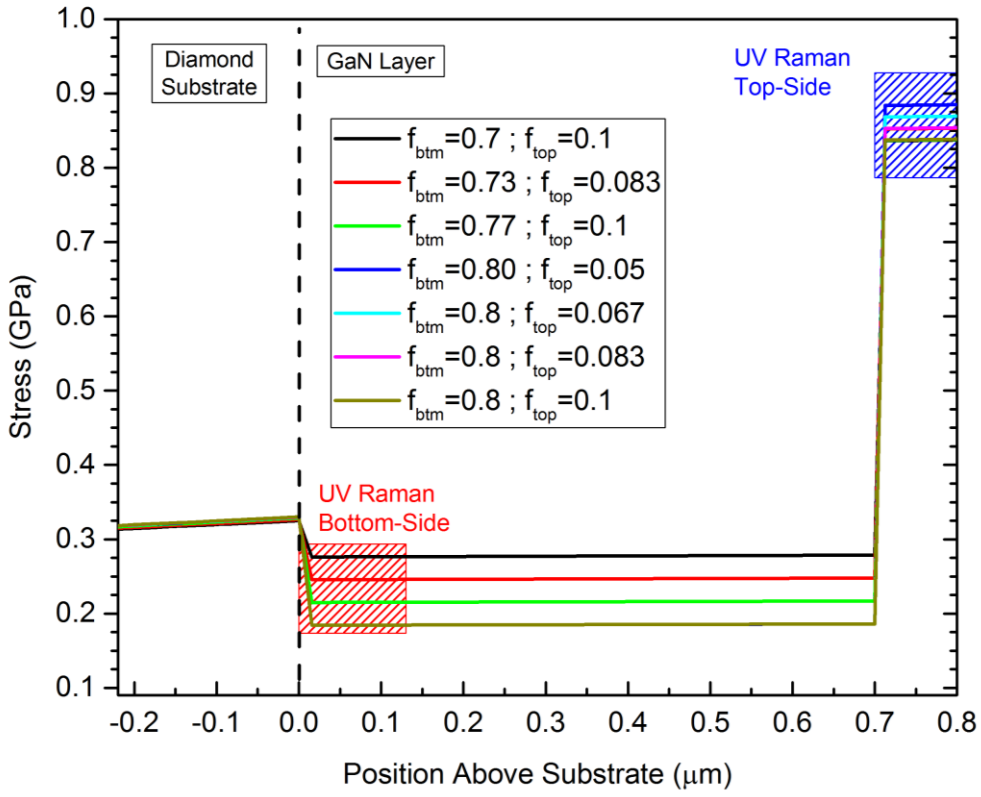

Figure 2.5. Data fitting using finite element. Results from FE simulation of thermal stresses in GaN-on-diamond wafer, discussed in Chapter Six. The plot demonstrates the technique for data parameterization used to fit experimental data with simulated stress results for different values of stress relaxation factor f_i.

3. INVESTIGATION OF SELF-HEATING IN INGAN/GAN HIGH-BRIGHTNESS LEDS

3.1 Abstract

In this chapter, the junction temperature of InGaN/GaN MQW high-brightness light-emitting diodes (LEDs) is measured using an electrical method based on the dependence of diode forward voltage, V_f, on the junction temperature T_j. Electroluminescence (EL) data collected during this measurement is presented and used to compare the efficacy of this method for measuring T_j to the electrical technique. In devices based on polar III-nitride materials, the temperature dependence of the EL peak energy is obscured by carrier screening and band-filling; the contributions of these effects are explored and presented. Additionally, the experimental method presented offers an application for extrapolating a thermal relaxation time during the junction temperature measurement. The results from this thermal time constant study are presented and discussed as well as future applications of the technique toward other high-power III-nitride devices and materials.

3.2 Motivation

III-V nitride-based materials have proven to be valuable in light-emitting diodes (LEDs) in the violet to near-ultraviolet (UV) wavelength range. Self-heating in the active region of these devices is a critical concern as it directly affects the internal quantum efficiency, peak emission energy, degradation, and overall operating lifetime. For this reason, monitoring the junction temperature in these devices is important.

Due to the size of the LED active region and encapsulation of modern packaging, direct measurement of the accurate junction temperature is not entirely possible using traditional methods such as resistive thermal detectors. The distance from the active region and the intermediate layers separating the LED materials from the detector also limit the precision and speed of these measurement techniques.

Spectroscopic measurements of the junction temperature can be accomplished several ways, including Raman spectroscopy [54], photoluminescence [55], and electroluminescence (EL) [18]. Apart from the experimental complexity of these measurement schemes, spectroscopic measurements reliant on the temperature-induced changes in band gap energy suffer from competition with carrier screening and band-filling in polar III-Nitride materials.

Xi and Schubert [17] presented an indirect method for establishing junction temperature based on the temperature dependence of the diode forward voltage in the active region for UV GaN LEDs. This method was extended and modified by Keppens et al. [21], who demonstrated an alternative experimental technique based on similar semiconductor principles for various packaged III-V LEDs.

The study presented in this chapter involves an experimental determination of junction temperature for packaged InGaN/GaN MQW high-brightness LEDs. The experimental approach is simplified when compared with previous reports [17], [21] and the expression derived for the forward voltage temperature dependence avoids the use of an empirical band gap dependence. An investigation of the effects of band-filling and carrier screening on the electroluminescence in these devices is also explored, offering a verification of the efficacy of the forward voltage method as compared to spectroscopic

techniques. Finally, the experimental setup utilized in this study provides an alternative means for extrapolating a thermal time constant for the material during the junction temperature measurement. Much of the work in this study has been reported in Ref. [53].

3.3 Experimental Procedure

Commercially-available high-brightness, blue (475 nm) InGaN/GaN MQW LEDs were investigated. Fig 3.1 shows a schematic of the experimental setup. Forward voltage and drive current measurements were accomplished using a Keithley 2400 SourceMeter in conjunction with a NI PCI-4472 data acquisition (DAQ) board voltmeter controlled via custom LabVIEW programs. Temperature calibration was performed with the LED mounted on a heat sink inside a standard temperature-controlled laboratory furnace. For electroluminescence measurements, the LED output emerging from a small aperture in the furnace wall was collected and focused into the fiber optic cable of an Ocean Optics miniature spectrometer.

3.3.1 Forward-Voltage Method

Figure 3.2(a) shows forward voltage, V_f, versus oven temperature obtained to calibrate the effect of junction temperature (T_j) on V_f. For these measurements, the LED was mounted on a heat sink inside a conventional laboratory oven. Temperature was set and allowed to stabilize at each temperature setting prior to the voltage measurement. A drive current of 2.0 mA at a frequency of 0.33 Hz with a 0.1 % duty cycle was used to minimize current-induced self-heating. A schematic of this pulsed drive current is shown in the inset of Fig. 3.2(a). The dependence in Fig. 3.2(a) allows us to obtain the negative linear temperature coefficient $\kappa = dV_f/dT$ as in Refs. [17], [18]:

$$V_f = V_0 + \kappa T_j \tag{3.1}$$

Once the linear regression in Eq. 3.1 has been established experimentally, the junction temperature T_j is readily obtained based on subsequent measurements. We obtained a value of κ = -1.64 $\pm$ 0.03 mV/K for the device studied, in good agreement with previously published results for GaN-based LEDs [6], [17], [18], [21].

Figure 3.2(b) summarizes the temperature dependence of the EL emission peak. These measurements were carried out simultaneously with the V_f calibration measurement discussed above, under identical low current drive conditions to avoid unwanted self-heating. Because the current is kept low during calibration, the emission is low in intensity. However, reasonable spectra are obtained over multiple cycles using an open shutter approach and a systematic red shift is obtained with slope dE_g/dT = -0.43 $\pm$ 0.01 meV/K. Because these data were obtained under low drive conditions, this shift corresponds to the temperature dependence alone. In non-polar quantum well structures, the EL shift may be used to determine device temperature even under normal operating conditions, as previously demonstrated in GaAs-based LEDs [1], [21], [56]. As discussed below, this is not the case for InGaN quantum wells due to screening of the built-in field and band-filling at high drive current. Figures 3.2(c-e) qualitatively depict the separate effects of heating-induced shrinkage of the band gap and carrier screening under applied forward bias. These effects combine to shift the overall EL peak, thereby preventing the straightforward use of optical measurements to estimate temperature rise in polar devices.

3.3.2 Calculations

The forward voltage temperature coefficient has been previously investigated [17], [21]. Based on the Shockley diode equation, Xi and Schubert [17] show that

$$e\frac{dV_f}{dT} \approx k_B \ln\frac{N_D N_A}{N_C N_V} + \frac{dE_g}{dT} - 3k_B, \tag{3.2}$$

Where N_D and N_A represent the donor and acceptor concentrations for electrons, respectively. N_C and N_V are effective densities of states at the conduction and valence band edges, respectively. E_g is the temperature-dependent energy gap, k_B is the Boltzmann constant, and e is the elementary charge.

Here, we describe the temperature dependence of E_g based on the phonon occupation [113], [114] rather than the empirical Varshni model. When the electron-phonon interactions may be grouped into acoustic and optic branches, the band gap shifts according to

$$E_g(T) = E_g(0) - \frac{\delta}{k_B}\left\{W_{ac}\varepsilon_{ac}n(\varepsilon_{ac},T) + W_{opt}\varepsilon_{opt}n\left(\varepsilon_{opt},T\right)\right\}$$

$$-\int_0^T[\xi_c\alpha_c(T') + 2\xi_a\alpha_a(T')]dT', \tag{3.3}$$

where δ is the high-temperature slope of the band gap, W_{ac} and W_{opt} are the acoustic and optic phonon weighting factors, subject to $W_{ac} + W_{opt} = 1$, ε_{ac} and ε_{opt} are the acoustic and optic phonon energies, and n is the Bose function. The last term in Eq. 3.3 accounts for thermal expansion; deformation potentials along the c (a) crystal axis of the active region material are ξ_c (ξ_a) and the corresponding thermal expansion coefficients are α_c (α_a). Across the temperature range studied here, this integral term in Eq. 3.3 is negligible

in comparison to the quantity in brackets [96]. In the temperature range where $k_B T > \varepsilon_{ac}$ the first term in brackets may be approximated as $W_{ac} k_B T$. In GaN, for which the phonon spectrum is similar to that of InGaN, ε_{ac} ~ 22.5 meV corresponding to a temperature of 260 K [96]. At even higher temperature, $k_B T > \varepsilon_{opt}$ and the second term in brackets becomes $W_{opt} k_B T$. The value of ε_{opt} ~ 69.3 in GaN with a corresponding temperature of 800 K [96]. For temperatures in this high range, the term in brackets in Eq. 3.3 simplifies to $k_B T$ so that we retrieve the linear dependence $E_g(T) \approx E_g(0) - \delta T$.

Values in the range 0.1 – 0.5 meV/°C have been reported in the literature for δ in InGaN [1], [6], [21], [115]–[117]. Despite our measurements being in the intermediate temperature range $\varepsilon_{ac} < k_B T < \varepsilon_{opt}$, our value of $\delta \approx 0.43$ meV/°C is reasonably within the published range.

A value for dV_f/dT can be calculated from Eq. 3.2 using our value for $\delta \approx 0.43$ meV/°C, assuming $N_D = N_A = 2\times10^{16}$ cm^{-3} and using GaN values for $N_C \approx (4.3\times10^{14})\, T^{3/2}$ cm^{-3} and $N_V \approx (8.9\times10^{15})\, T^{3/2}$ cm^{-3} from Ref. [17]:

$$e\frac{dV_f}{dT} \approx k_B \ln\frac{N_D N_A}{N_C N_V} - \delta - 3k_B \,. \tag{3.4}$$

This results in a slope $dV_f/dT \approx$ -1.77 mV/°C for this type of device, in agreement with the measured value of -1.64 $\pm$ 0.03 mV/K from Fig. 3.2(a).

3.4 Junction Temperature Results

The junction temperature was measured with the LED mounted in thermal contact with a standard heat sink and operated with a drive current ranging from 10 to 600 mA. DC current at this value was initially applied for 2 minutes to establish steady-state

conditions, as monitored via the V_f value. The current was then abruptly switched to 2 mA to match what was used in the calibration step, as illustrated in the inset of Fig. 3.3. By taking a forward voltage measurement at the low current, the linear regression obtained from calibration, Fig. 3.2 (a), can be used to calculate the junction temperature for the LED. We find that determining V_f at a time < 3 ms after switching to low current allows the setup to pass the Gibbs overshoot while preceding significant cooling in the active region. In Fig. 3.3 we show results of the dynamic junction temperature measurement as a function of drive current. The T_j increase is slightly faster than linear with current due to the diminishing thermal conductivity as temperature increases and the higher fraction of input power generating heat rather than optical output.

3.5 Effects of Self-heating on EL Spectrum

Figure 3.4(a) shows EL spectra obtained at different drive currents under identical conditions to those used for measuring T_j. The low-current spectrum shows an EL peak at 2.595 eV. As drive current is increased, intensity rises and we observe a systematic blue shift in the EL peak position. The blue shift is seen clearly in Fig. 3.4(b), where we plot EL peak energy as a function of drive current. Since T_j is increasing with drive current (Fig. 3.3), and the band gap, as seen in Fig. 3.2(b), demonstrates a red shift with increasing temperature, the observed blue shift is not attributable to a rise in temperature. Band-filling is one possible cause for the overall shift, an effect which would also result in broadening of the EL emission [3], [6], [118], [119]. In addition, the blue shift is expected from carrier-induced screening of the built-in field within the (0001)-oriented III-nitride quantum wells [3], [119].

3.6 Effects of Screening and Band-filling on EL Spectrum

As previously illustrated in Figs. 3.2(c-e), the combined effects of band-filling and carrier screening make a significant contribution to the behavior of the EL spectrum for InGaN MQW devices; this can be seen in the data in Fig. 3.4(b). The influence of these effects is further demonstrated in Fig. 3.5. The data in black represents the shift in EL peak energies from Fig. 3.4(b) relative to the room-temperature peak position. The solid curve in red corresponds to the expected shift in EL peak energy due to temperature rise; the T_j values are measured at each drive current. This was determined using the linear trend from Fig. 3.2(b) for temperature-induced band gap shrinkage. The blue points are the result of correcting the measured shift (in black) for the effects of temperature on the band gap to illustrate the effects of band-filling and screening. As deduced from the plot, band-filling plus carrier screening impart a relative blue shift of approximately 28 meV on the EL for these devices. This illustrates the necessity for using an electrical approach, like the forward voltage method, for determining the junction temperature in InGaN LEDs (and similar devices based on other polar semiconductors) as opposed to measurements based solely on EL measurements.

3.7 Extraction of Thermal Time Constant

Heat generated in the LED active region due to non-radiative recombination and resistive losses is transferred to the substrate by means of thermal conduction. The time-dependence of this heat transfer can be described by the familiar relation

$$\frac{dQ}{dt} = h\,A\,[T(t) - T_{ambient}]\,, \tag{3.5}$$

where dQ/dt represents a heat flux, h is the heat transfer coefficient in units W/m^{2}K, and A represents the surface area where the heat flux takes place. Expressing this in terms of the heat capacity $C = dQ/dT$ and using the thermodynamic relationship $dQ/dt = C(dT/dt)$, the above relation can be rewritten:

$$\frac{dT(t)}{dt} = -\frac{hA}{C}[T(t) - T_{ambient}] \equiv -\frac{1}{\tau}\Delta T(t). \tag{3.6}$$

The quantity C/hA corresponds to a thermal time constant, τ, characteristic of the device and the term $\Delta T(t) = T(t) - T_{ambient}$. The solution to this differential equation can be written as

$$\Delta T(t) \sim \exp\left(-\frac{t}{\tau}\right). \tag{3.7}$$

When multiple factors contribute to the cooling, each with different time constants τ_i, they may be taken into account by adding further terms to Eq. 3.7 with coefficients β_i corresponding to their relative contributions. For the case of III-V LEDs, identification of the thermal time constant is useful as this material-characteristic value gives insight into the underlying behavior of the heat dissipation throughout the device. In Ref. [120], Vitta *et al.* present a method for extracting the time constant in various LED materials using a frequency modulation technique. Shan *et al.* in Ref. [5] calculate the thermal time constant by considering a thermal resistor in analogy to RC circuits. They measure the quantity during the cooling period following a DC drive current. A similar experimental extraction of this time constant for AlGaN/GaN HEMTs during pulsed operation is presented by Lancry et al. in Ref. [9].

During the low-current pulse of our junction temperature measurement, an immediate rise in forward voltage is observed, as shown in Fig. 3.6. This rise is attributed to cooling in the device as heat diffuses from the active region into the subsequent mounting layers and into the heat sink. This voltage data may be translated into a time dependent temperature using the calibration data in Fig. 3.2(a). Previous investigations [5] have used analogous results to estimate the thermal time constant, τ, by fitting temperature as a function of time with an exponential decay similar to Eq. 3.7. In agreement with these prior reports, the exponential decay model which best fits our data involves two time constants, of the form:

$$T(t) = \beta_1 \exp\left(-\frac{t-t_0}{\tau_1}\right) + \beta_2 \exp\left(-\frac{(t-t_0)}{\tau_2}\right), \tag{3.8}$$

where τ_1 and τ_2 are the thermal time constants and t_0 is the time at which the drive-voltage is switched to begin the T_j measurement.

Figure 3.7 shows the thermal time constant results (lower panel) and R^2 of the fit for various drive conditions. It is apparent from the plot of R^2 that the fit is superior for higher drive currents, above 200 mA. This is expected, as the temperature difference from ambient is greatest at higher drive so the measured voltages are more significant. The dotted line is a guide to the eye for the two average thermal time constant values: τ_1 = 3.26 $\pm$ 1.16 ms and τ_2 = 26.1 $\pm$ 3.77 ms, which are in agreement with related studies for these materials [5], [120], and the ratio $\beta_1/\beta_2 \sim 2$. The presence of two time constants can be attributed to the lateral and vertical heat flow through the LED chip itself, and then into underlying sub-mount material, acting as parallel heat conduction paths from the device active region. This signifies that the experimental method

presented here is a viable means of extracting the thermal time constant during operation and is prospectively useful for predicting failure during operation.

3.8 Chapter Summary

In summary, the junction temperature for InGaN/GaN MQW high-brightness LEDs was determined using a straightforward electrical technique. The approach was checked up to a temperature rise of ~ 90 °C above ambient in a commercial blue LED. The observed blue shift in the EL spectra, under typical drive conditions, confirms the presence of band-filling and carrier screening in the polar III-nitride materials for these devices in addition to the ubiquitous self-heating. These combined effects preclude the use of EL for estimating temperature in these polar device materials. By comparing the behavior of the EL peak energy under high drive currents and at low-pulse currents, the extent of these competing effects was quantified. The presence of these effects on the peak output energy further confirms the efficacy of using an electrical technique such as the forward voltage method for accurate junction temperature measurements in III-N high-brightness LEDs and its superiority over spectroscopic methods for devices incorporating polar materials. Finally, it is demonstrated how the forward voltage technique offers the potential of enabling an experimental means for extracting the thermal relaxation time for the device material.

3.9 Figures

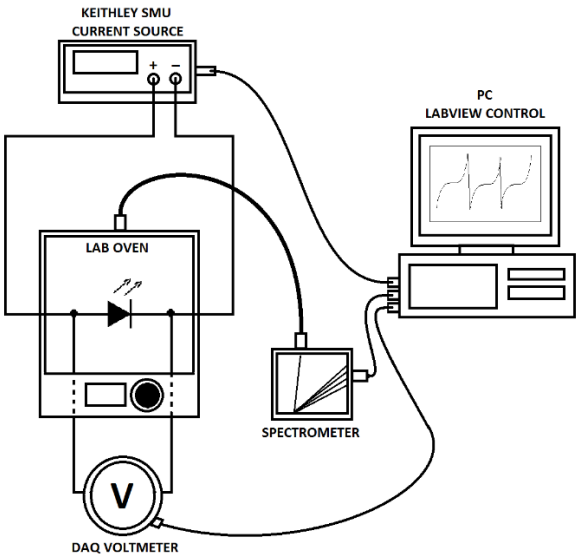

Figure 3.1. Experimental setup. Schematic drawing of experimental setup for calibration and junction temperature measurement in high-brightness LED.

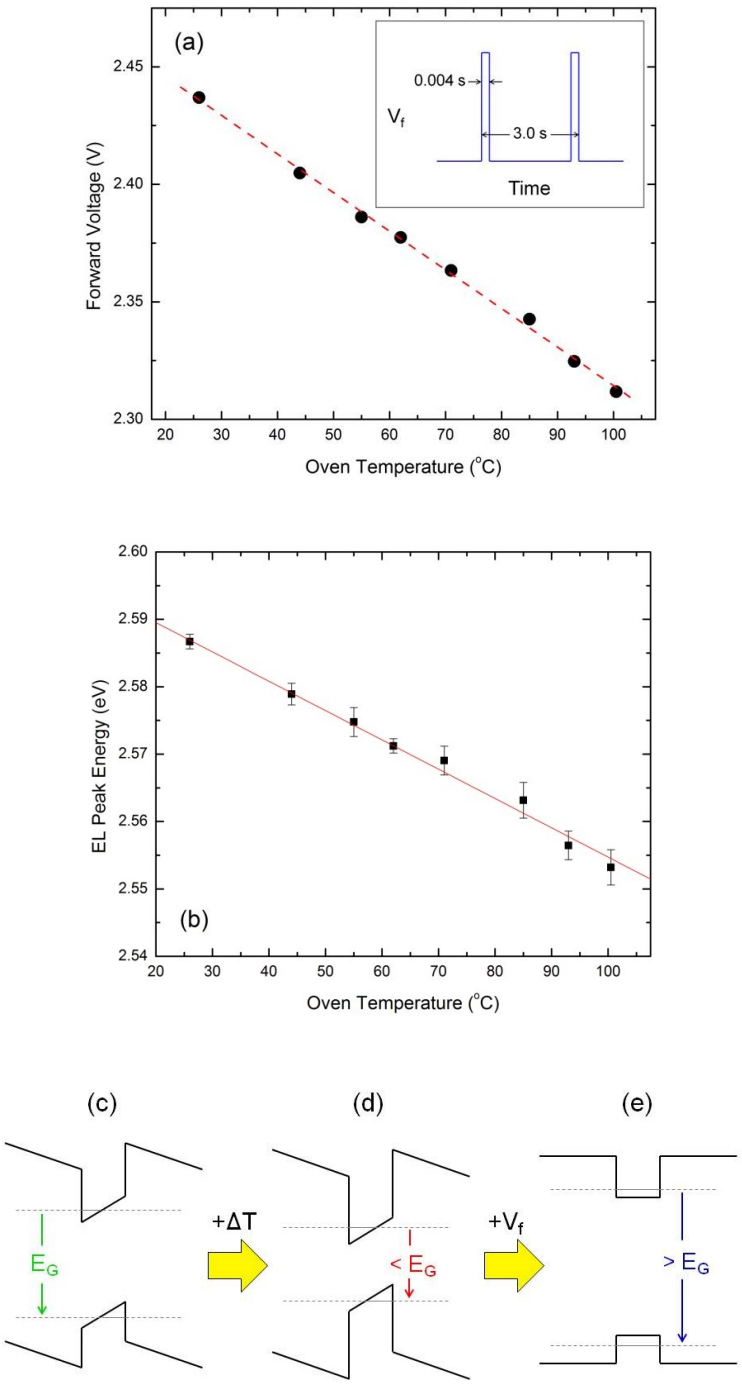

Figure 3.2. Results from calibration step of forward voltage method. (a) Calibration of measured forward voltages for changes in ambient temperature. The inset illustrates the pulsed current used to operate the device while minimizing self-heating. (b) Electroluminescence peak energies obtained during calibration. (c) Depiction of band edges in polar InGaN MQW without external drive. (d) Illustration of the effects of increasing only temperature on the band gap energy and (e) Effect of voltage-induced carrier screening on changes in the band gap energy.

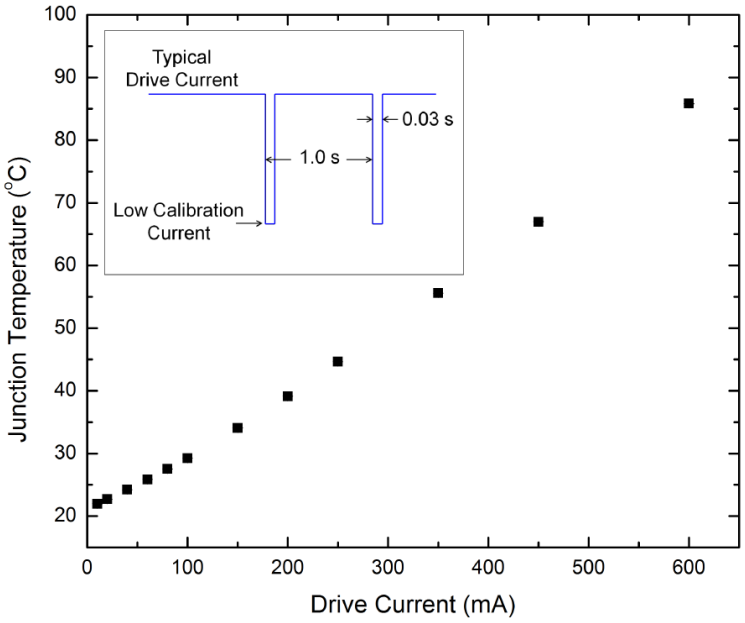

Figure 3.3. Junction temperature as a function of drive current. Measured junction temperature values for various LED drive currents. The inset illustrates the lineshape of the applied drive current; the junction temperature is measured in the notch when low calibration current is applied.

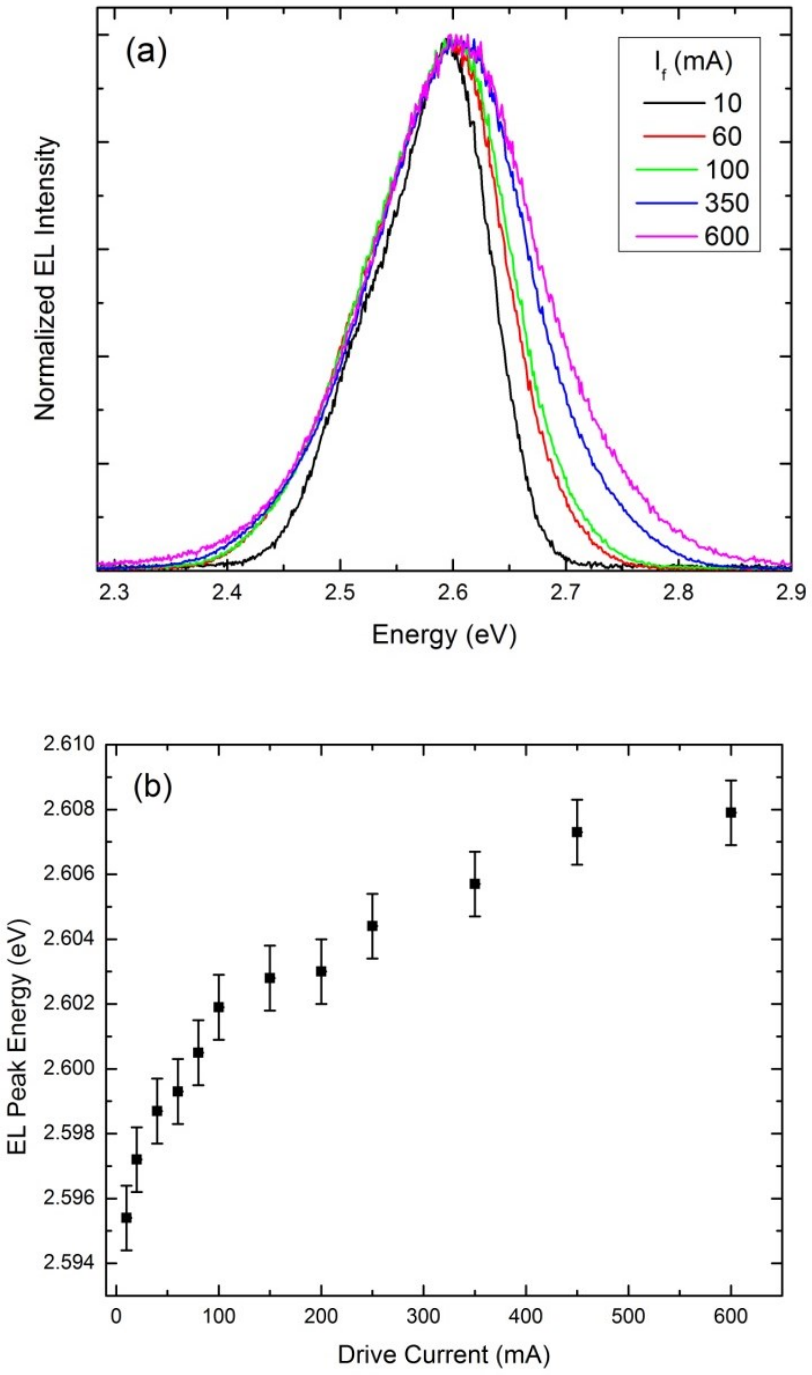

Figure 3.4. Electroluminescence data for typical drive currents. (a) EL spectra collected during the junction temperature measurement. (b) Summary of the EL peak energies at each applied drive current during the measurement.

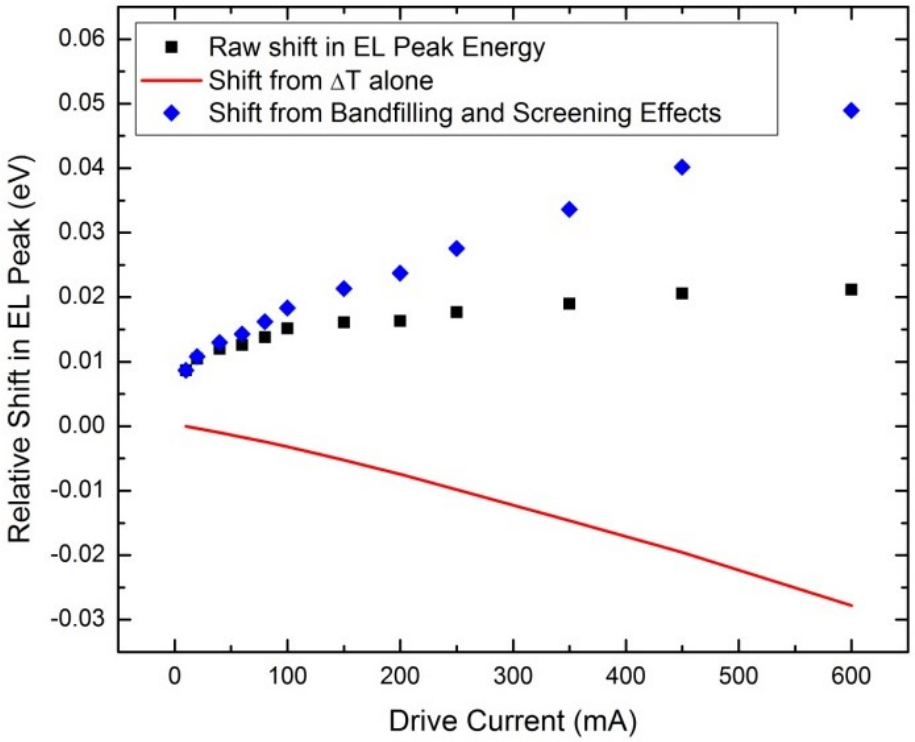

Figure 3.5. Demonstration of the effects of band-filling and carrier screening on EL. Square data points (black) represent the relative shift of the EL peak energies. The solid curve (red) shows the expected shift for only temperature-induced changes in the band gap energy based on data in Fig. 1. Diamond data points (blue) show the effect of bandfilling and carrier screening.

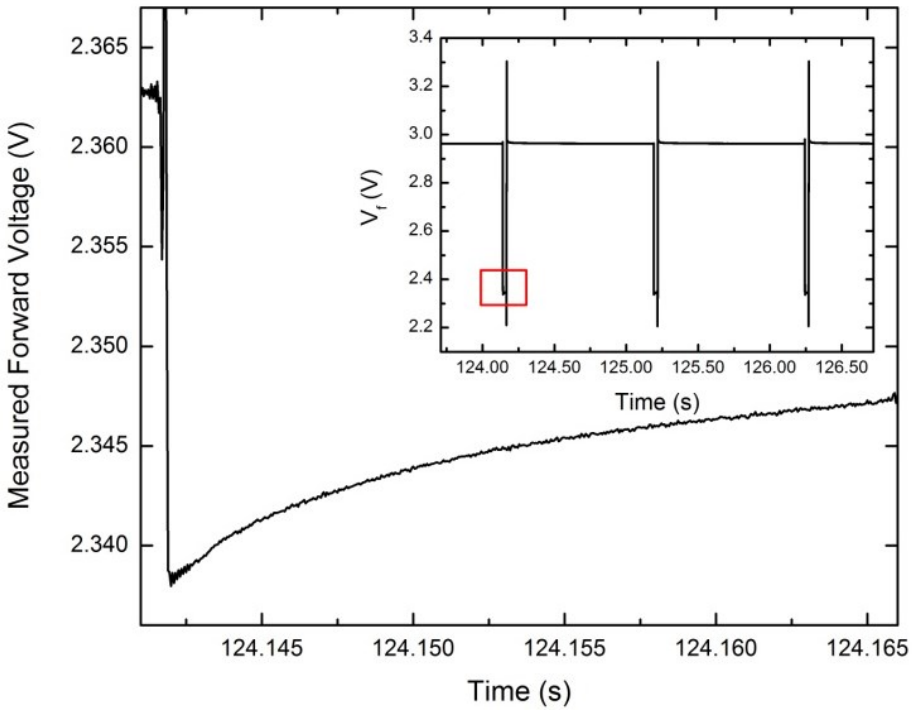

Figure 3.6. Output of DAQ voltmeter used to measure junction temperature. The inset highlights the region of the pulsed current plot used to extract the cooling in the device.

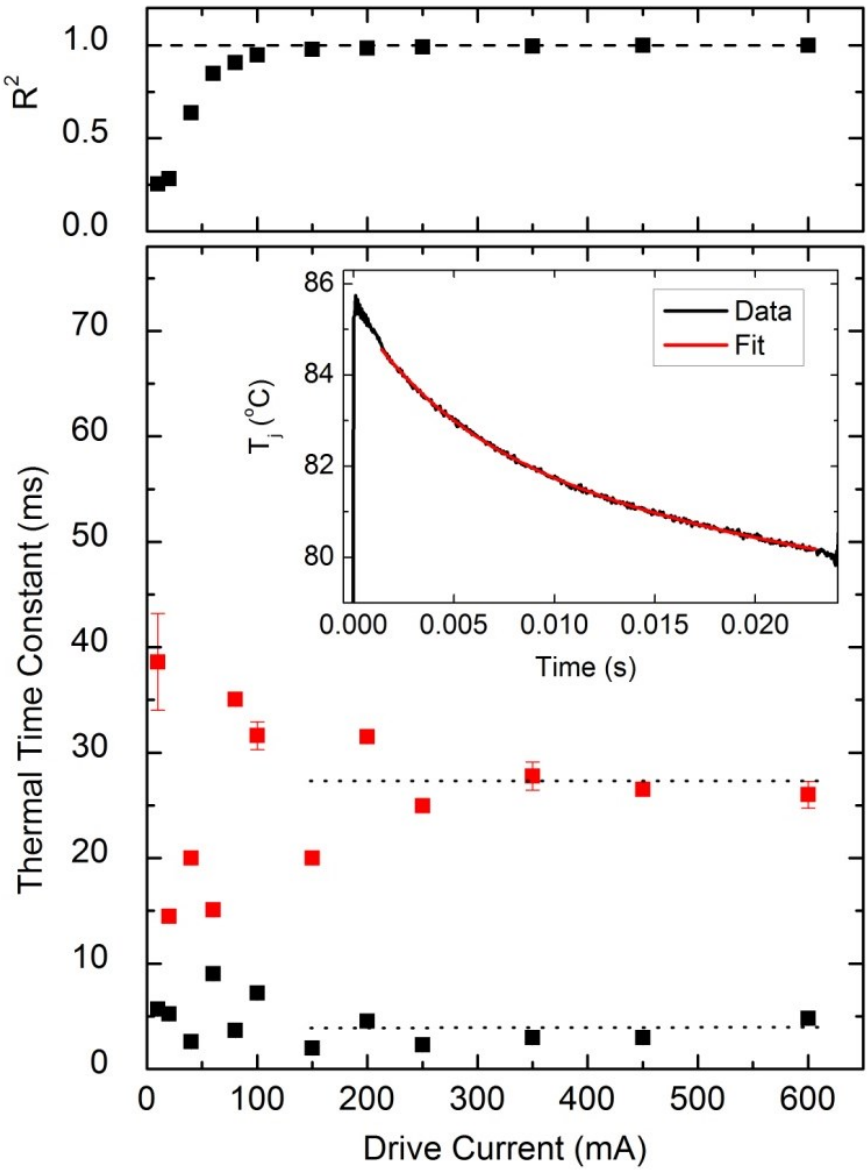

Figure 3.7. Plots of measured thermal time constants for the LED. The dotted line indicates average values for the two time constants resulting from the fitting illustrated in the inset. The top panel shows R2 values for each drive current.

4. MICRO-RAMAN INVESTIGATIONS OF SELF-HEATING IN ALGAN/GAN HEMTS

4.1 Abstract

The process of examining thermal behavior of AlGaN/GaN high electron mobility transistors (HEMTs) using ultraviolet (UV) and visible micro-Raman spectroscopy is discussed in this chapter. Utilizing the different optical penetration depths for UV and visible excitation, temperature rises during operation are extracted from the various material layers throughout the HEMT vertical cross-section to obtain a temperature depth profile for the device. Temperature rises are observed in the region near the 2-dimensional electron gas (2DEG) in excess of 350°C above ambient for an input power of 7.8 W/mm. Finite element analysis is utilized to simulate the temperature as a function of depth and used to gain insight into heat transfer and thermal boundary resistance across the layer stack.

4.2 Motivation and Background

Self-heating in GaN-based transistors is a critical concern. With output power densities upwards of ten times that of those seen for Si or GaAs technologies, the consequences of local temperature rises and self-heating are much higher as well [9]. For the specific case of AlGaN/GaN heterostructure field-effect transistors (HFETs) and high-electron mobility transistors (HEMTs), the majority of current flow is confined within a small (< 10-nm) channel due to the presence of the two-dimensional electron gas (2DEG) at the AlGaN-GaN interface. As a result, significant temperature rises are tightly localized to the small active region of the device. For this reason, gaining accurate

knowledge of the temperature effects in these devices is crucial to advancements in reliability and performance.

Several methods exist, both in research and industry, for observing the operation temperature in transistors and similar devices, such as IR thermography, thermocouples, scanning thermal probes, and thermographic phosphors [9], [52], [57]. Many of these techniques exhibit considerable drawbacks, including the requirement of direct physical contact with the device, invasive or destructive fabrication procedures, limitations in temperature and spatial resolution, or slow collection response times and complex analyses [57].

Micro-Raman spectroscopy has been well-established as a successful tool in semiconductor thermography by a number of groups [22], [24], [25], [27], [28], [52], [90]. Raman spectroscopy is indirect, non-invasive, and offers a precise assessment of changes in temperature for the epilayers and substrate materials. With enhanced spatial resolution (~ 1 μm), the technique also allows for accuracy in both single sample studies as well as real-time spatial mapping capabilities [25]. The majority of micro-Raman temperature studies are performed using visible excitation. As GaN is transparent to visible light, these measurements offer an estimate of the average temperature rise throughout the bulk of the GaN layer [27], [28], [90].

By using ultraviolet (UV) excitation above or near the band gap of GaN, the shallow optical penetration depth (~100 nm) allows the GaN to be probed near the thin 2DEG region at the AlGaN/GaN interface. This has been previously demonstrated for AlGaN/GaN HFETs on SiC substrates [27], [28]. By combining the visible and UV

micro-Raman techniques, a profile of the temperature rise through a device during operation can be obtained.

In this chapter, UV and visible micro-Raman are utilized in conjunction to investigate temperature rises in high-power AlGaN/GaN HEMT devices grown on silicon substrates. A vertical temperature-depth profile is obtained based on combining the data from these two techniques under typical drive conditions for the device. The temperature rise, ΔT, is measured in the GaN near the 2DEG region, an average ΔT in the GaN, in the AlN nucleation layer above the substrate, and in the silicon substrate. Finite element simulation is used to support the data in examining vertical heat dissipation through the HEMT material stack and estimating the thermal boundary resistance (TBR) between the nitride MOCVD layers and the substrate. Much of the work presented here has been reported in Ref. [58].

4.3 Experimental Procedure

The AlGaN/GaN HEMT studied was grown by MOCVD on a 100-mm silicon wafer with 500-μm thickness. The epilayer materials and thicknesses are as follows: AlN nucleation layer (0.45 μm), $Al_{0.60}Ga_{0.40}N$ transition layer (0.45 μm), $Al_{0.30}Ga_{0.70}N$ transition layer (0.25 μm), GaN buffer (0.8 μm), $Al_{0.26}Ga_{0.74}N$ confinement layer (17.5 nm), and GaN cap layer (1.5 nm). Figure 4.1(a) shows a transmission electron microscope (TEM) image of the layer structure with a magnified cross-section at the AlN-Si interface. The device studied was a HEMT or HFET single-finger test structure from Nitronex Corporation, produced using standard commercial fabrication techniques, consisting of a single 0.5-μm gate (G) centered between source (S) and drain (D) structures with a source-drain separation of 5 μm and channel width of 100 μm. An

optical micrograph of the test structure is shown in Fig. 4.1(b). Further details of the device structure and fabrication can be found in Ref. [121]. For the investigations presented here, a single transistor was powered, accomplished through wire-bonding of the S, G, and D contact pads to a commercial chip carrier upon which the sample die was mounted using indium for good thermal contact.

The micro-Raman experiment was carried out using a back-scatter configuration with visible (514.5 nm) and UV (363.8 nm) excitation with respective spot diameters of ~2 and 3 μm. Excitation was focused between the gate and drain contact, as this has been recognized as a region of localized heating [27], [28]. Raman measurements were accomplished at various drain-source voltages (V_{DS}), maintaining a gate-source voltage V_{GS} = 0 for all cases. Figure 4.1(c) provides a schematic of this measurement setup, indicating the probe depths for both optical measurements. Optical power density for the UV excitation was maintained below 0.4 μW/μm^2, as this has been identified as a range for which local heating due to laser excitation is negligible [122]. For λ_L = 363.8 nm, the optical penetration depth in GaN is estimated from the attenuation coefficient α of the laser excitation (L) and scattered light (S) using $d_{opt} = 1/(\alpha_L + \alpha S) \sim 100$ nm [123]. This makes the measurement suitable for observing temperature rises near the 2-DEG in the GaN.

Figure 4.2 shows a plot of drain-source current (I_{DS}) as a function of drive voltage (V_{DS}) for various values of gate-source voltage (V_{GS}), demonstrating typical output characteristics for the device studied. For a specific V_{GS}, current increases with V_{DS} in a narrow range of applied voltage before saturating and eventually decreasing. The current droop in this case is a direct consequence of reduced carrier mobility due to self-heating

in the 2-DEG. Positive gate voltage increases I_{DS} in these depletion-mode field-effect devices and decreases the current for negative bias, with a complete channel shut-off at $V_{GS} = -1.5$ V.

4.4 Micro-Raman Results and Discussion

Figure 4.3(a) shows visible Raman spectra collected at different values of V_{DS} with $V_{GS} = 0$, with the distinct Raman features labeled for each material. For $V_{DS} = V_{GS} = 0$ V, the GaN E_2^2 and A_1(LO) modes of the 0.8-μm GaN layer are observed at 564.5 and 731.4 cm^{-1}, respectively. The AlN nucleation layer exhibits an E_2^2 band at 648.7 cm^{-1} and a weak A_1(LO) feature near 880 cm^{-1}. The strong peak from the Si substrate peak in each spectrum is seen at 520 cm^{-1}. For visible excitation ($\lambda_L = 514.5$ nm), the optical penetration depth in silicon, $d_{opt} \sim 0.8$ μm [124], allowing redshifts in this Raman line to be used for estimating the average temperature rise, ΔT, at this depth in the substrate near the interface with the AlN nucleation layer. Broad second-order features from the silicon and from the transition layers are also noted in the figure. The inset of Fig. 4.3(a) and Fig. 4.3(b) demonstrate how the Si, GaN, and AlN phonon peaks are observed to redshift with increases in input power.

The near-band gap UV excitation ($\lambda_L = 363.8$ nm) used for UV Raman produces a strong photoluminescence (PL) in the GaN. Figure 4.4 shows a typical room-temperature PL spectrum of the device investigated, acquired using a pulsed Ti:Sapphire laser with $\lambda_L \sim 266$ nm. The vertical lines in the plot show the positions for the 363.8-nm excitation and the corresponding positions for the E_2^2 and A_1(LO) Raman Stokes shifts studied here. The inset of Fig. 4.4 demonstrates how the Raman features are superimposed on the

strong PL features for the UV measurement. Excitation power was kept low to minimize the effects of heating and to keep the detector exposure well below saturation. Despite the PL background, which is 4–5 times the intensity of the Raman bands, these features remain discernible and useful for estimating temperature rise in the GaN near the AlGaN barrier layer.

Temperature rises in the 2-DEG channel between the source and the drain structures cause a redshift and linewidth broadening in the phonon modes for the material. The redshift in the different phonon energies, ω, for each layer is used to estimate the rise in temperature $\Delta T = T - T_0$. The temperature dependence of phonon energy is expected to be linear in the range investigated here according to

$$\omega - \omega_0 = k_T(T - T_0)\,, \tag{4.1}$$

where ω_0 is the phonon energy for the material at ambient room temperature T_0 and k_T is the phonon-dependent temperature coefficient with units cm^{-1}/K. The temperature dependences of each phonon investigated in this study have been established [98], [125]. These values were verified for this device as well, using a Peltier heater in conjunction with a calibrated thermistor. Measured values of ω and ω_0 for each material are used with corresponding coefficient k_T for each phonon to estimate ΔT during device operation. Figure 4.5 shows a summary of the temperature rise in each layer for the device as a function of input power.

Figure 4.6 displays the temperature depth profile for two specific input powers. The horizontal ranges for these data points correspond to the thickness averaged by each measurement and the vertical range corresponds to uncertainty in the peak position from

Raman data-fitting. As expected, the temperature rise is significantly higher near the 2-DEG region in the GaN, with ΔT ~ 350°C. The maximum temperature rise observed in the GaN for visible excitation (based on visible Raman) is ~ 225 °C at an input power of 7.8 W/mm. Variations in design (packaging, layout, device density, etc…), layer compositions and thicknesses, and substrate materials make it difficult to directly compare this result to values found in literature. In Ref. [126], for a similar device structure, visible Raman temperature measurements yield ΔT ~ 300 °C for ~2.8 W/mm input power. This higher ΔT is possibly due to differences in layer compositions, thicknesses, and TBR. Similarly in Ref. [127], for a device with thin 150-nm GaN buffer layer, a temperature rise of ΔT ~ 300 °C was observed in the GaN and ΔT ~ 80 °C in the silicon substrate for input power of 6.8 W/mm. They attribute this high ΔT to a low thermal conductivity in the GaN.

Results from a 3D finite element simulation for the device are also included in Fig. 4.6. Thermal conductivities for 35 and 290 W/mK were used for the AlGaN and AlN, respectively [128], [129] and 130 W/mK for silicon [130]. Because of the large temperature rise in the GaN near the 2DEG a temperature-dependent thermal conductivity was utilized according to $\kappa_{GaN}(T) = 220(300/T)$ [130].

A TBR was also incorporated into the finite element model at the AlN/Si interface. TBR values in the range of 0.5 – 1 × 10^{-8} m^2K/W adequately simulate the observed ΔT dependence, with best agreement for TBR ~ 1 × 10^{-8} m^2K/W for the data sets shown in Fig. 4.6. It should be noted that at higher operating powers, the temperature dependence of κ_{GaN} becomes more important as the ability of the 2-DEG material to effectively dissipate heat begins to degrade.

The TBR for GaN-on-Si devices has been previously reported as 3.3×10^{-8} m^2K/W [26]. The lower TBR obtained in this study may be a consequence of superior interface quality between the substrate and AlN nucleation layer. The acoustic mismatch model (AMM) [131] can be used to calculate the expected TBR between AlN and Si. This yields a lower TBR of ~ 0.9×10^{-9} m^2K/W, comparable with prior calculations for GaN on Si, SiC, and AlN [68]. The use of diffuse mismatch model (DMM) results in an increased estimate for TBR by ~40%–50% higher than AMM estimates for GaN on Si [131]. Calculations from AMM and DMM results are well below the experimentally determined values here and reported by others [26], [90], [132], [133]. This is most likely due to the theory not being able to account for lattice imperfections at the interface, formation of immediate nucleation region where AlN growth begins, or the presence of native defects in the III-nitride layer close to the interface.

4.5 Chapter Summary

In summary, a depth-dependent profile of temperature rise is investigated for an AlGaN/GaN HEMT using visible and UV micro-Raman spectroscopy. The combination of UV and visible excitation provide insight into the behavior of heat flow for the various layers of the device during operation. Measurements near the 2DEG region of the GaN reveal a temperature rise of ~350 °C for 7.8 W/mm input power, almost twice that seen in the bulk of the GaN from visible Raman. Finite element simulations are used to interpret the temperature depth profile and to establish a value for the TBR present between the AlN nucleation layer and Si substrate.

4.6 Figures

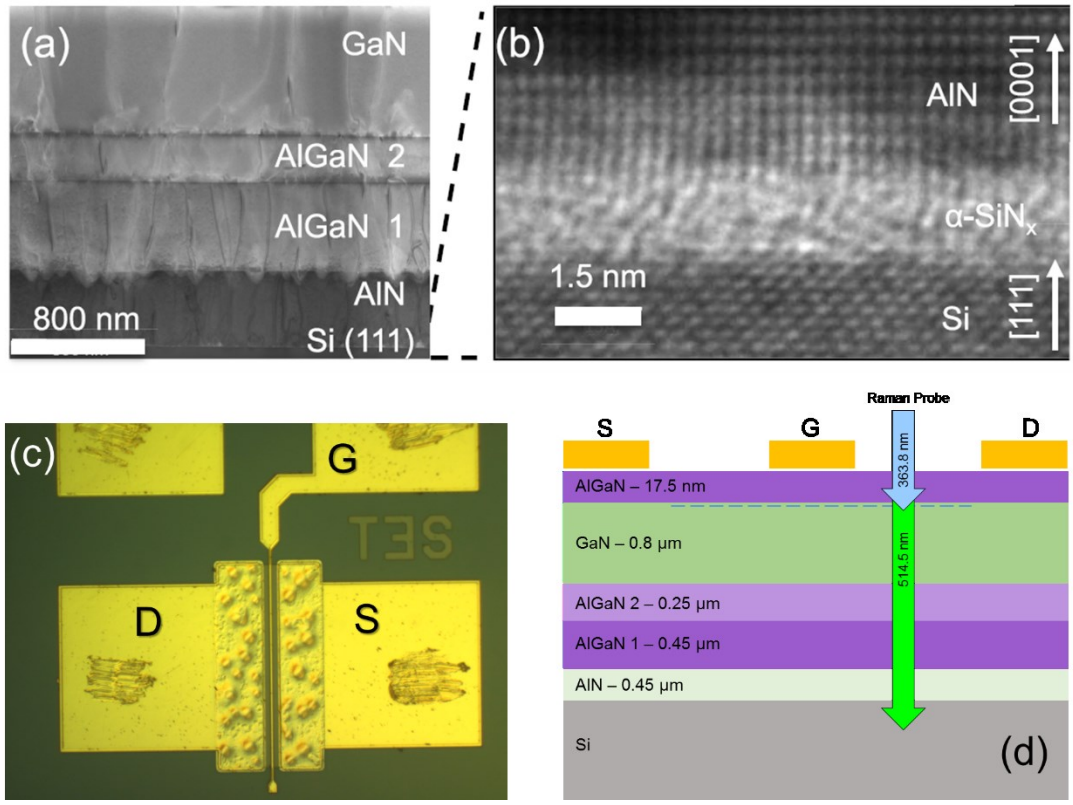

Figure 4.1. HEMT material details. (a) TEM images of the device layer structure. (b) Magnified TEM cross-section of the AlN/Si interface. (c) Optical microscope image of the device studied here, with source (S), gate (G), and drain (D) contact pads labeled. (d) Schematic of the material cross-section for the device studied with epilayer thicknesses. The penetration depths for UV (363.8-nm) and visible (514.5-nm) excitation are illustrated.

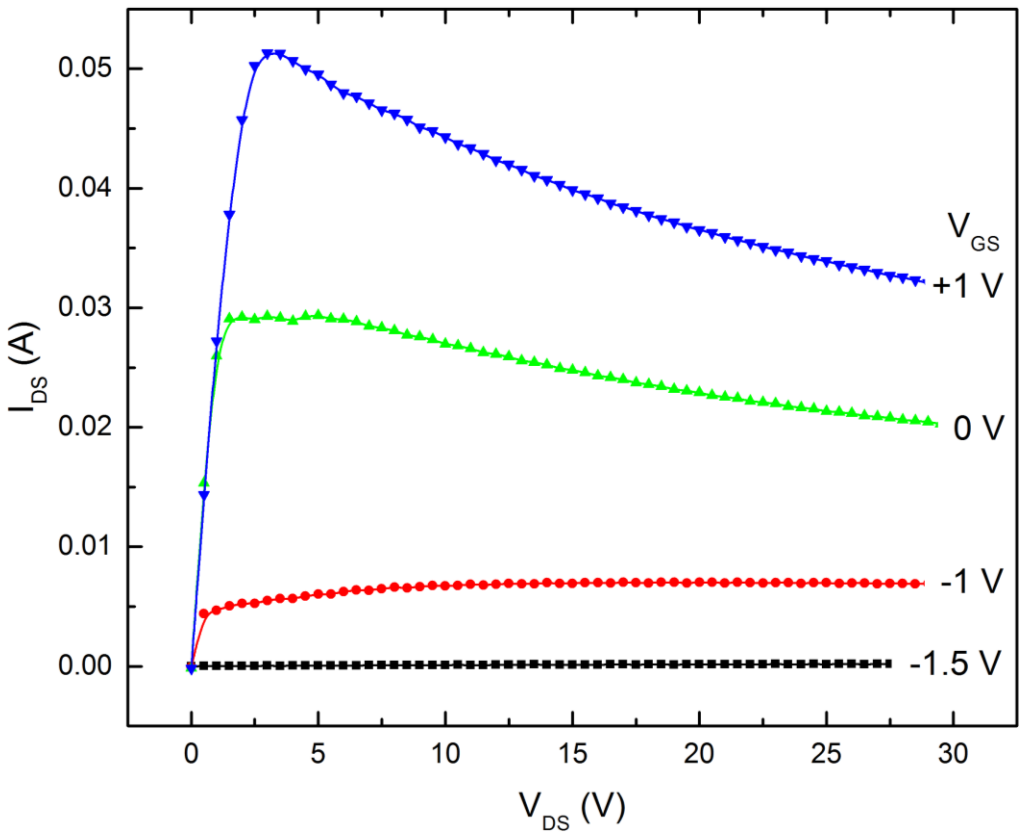

Figure 4.2. Typical I-V behavior for AlGaN/GaN HEMT device operation. Drain-source current (I_{DS}) as a function of drain-source voltage (V_{DS}) at different values of gate-source voltage (V_{GS}) for the HEMT device studied.

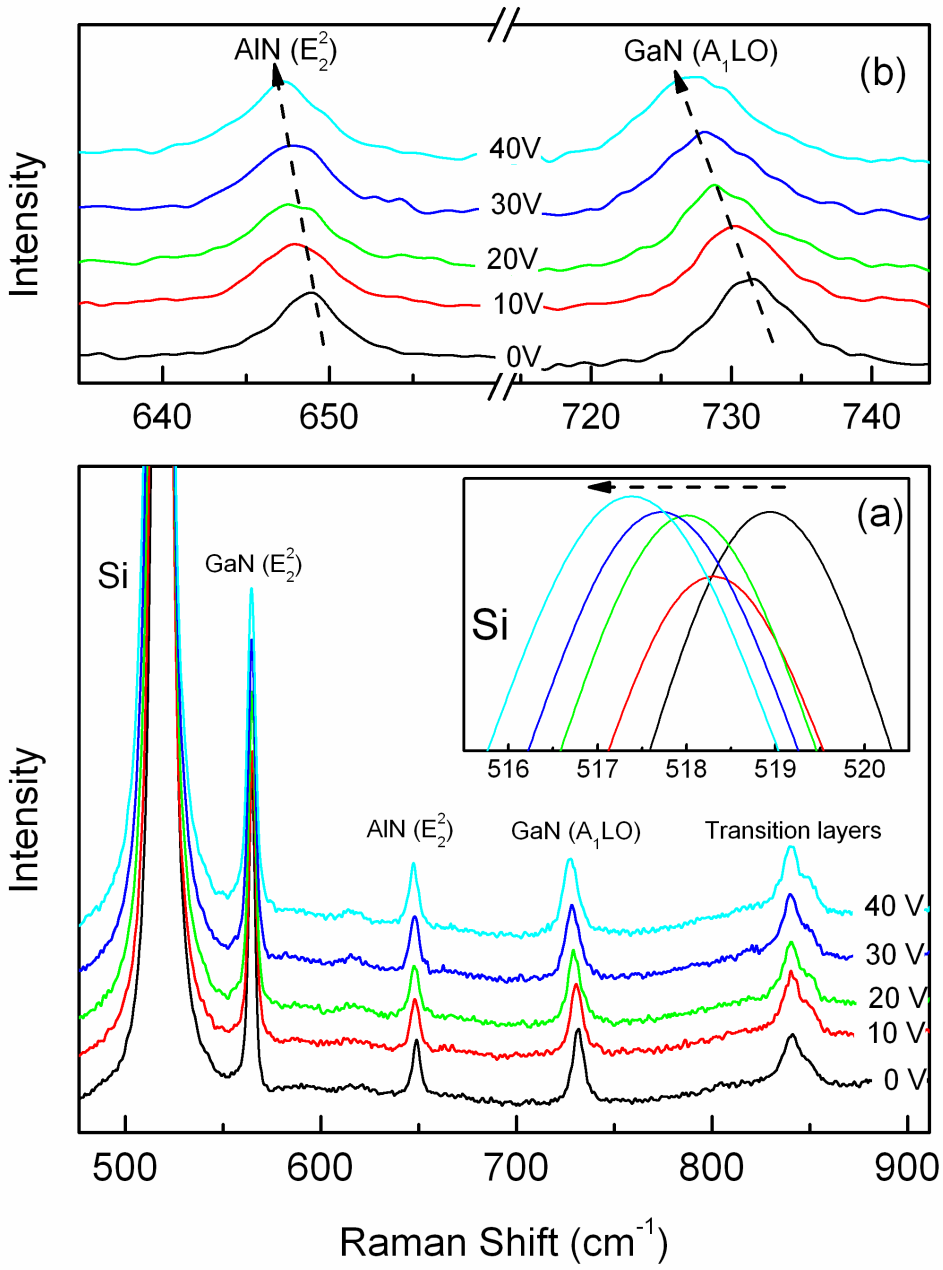

Figure 4.3. Visible Raman spectra at different drain-source voltages. (a) Visible spectra collected at various values of V_{DS} displaying the various Raman features for GaN, AlN, transition layers, and Si substrate. The inset shows a magnification of the behavior for Si ~ 520 cm^{-1} as a function of voltage. (b) Behavior of AlN E_2^2 and GaN A_1(LO) phonons at each V_{DS} value with arrows emphasizing the redshift seen for increasing input power. All measurements collected for V_{GS} = 0 V.

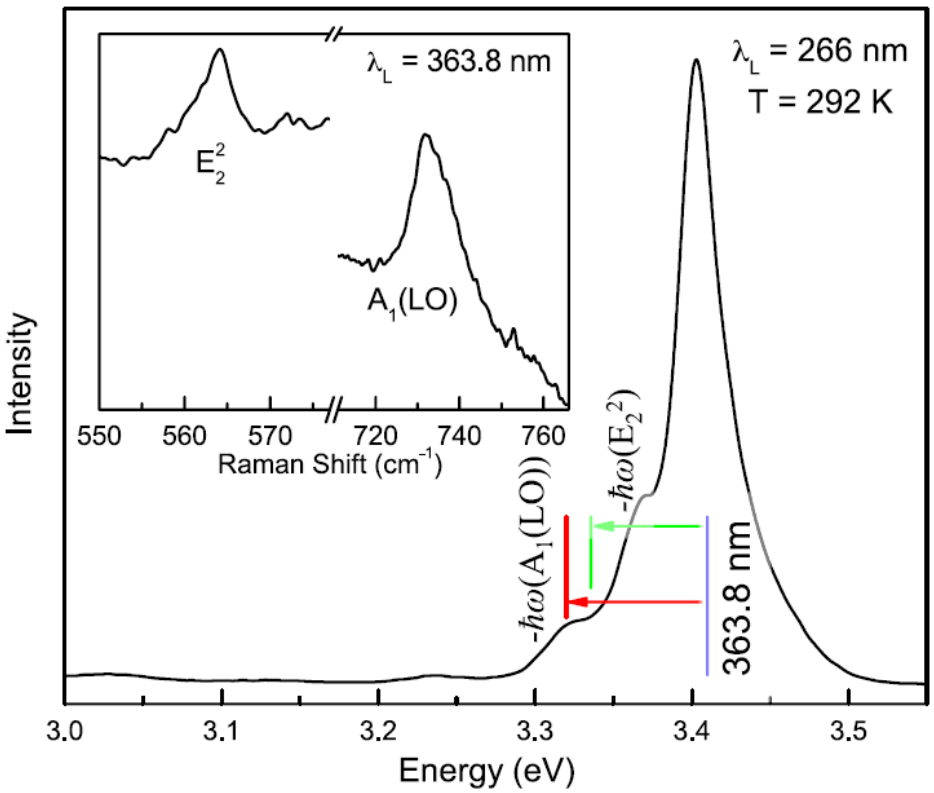

Figure 4.4. Room temperature photoluminescence of HEMT device. PL spectrum of the device is shown with vertical lines denoting laser excitation (363.8 nm), GaN E_2^2, and A_1(LO) phonon energy positions. The inset shows UV Raman spectrum for the condition $V_{DS} = V_{GS} = 0$.

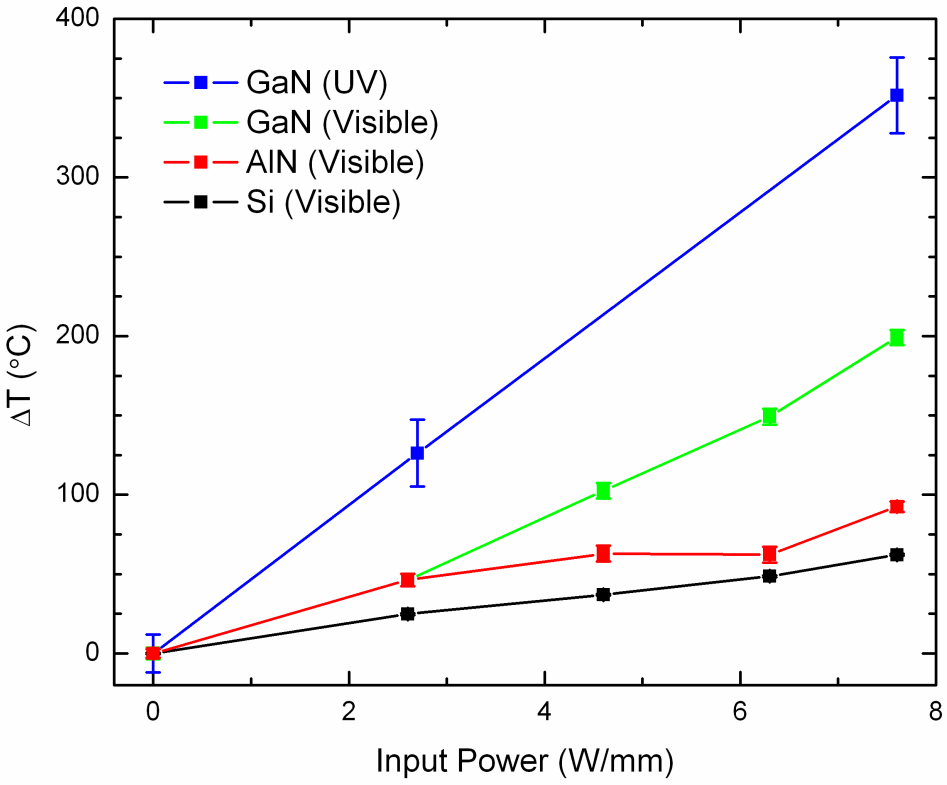

Figure 4.5. Visible and UV Raman data for different input powers. Summary of the temperature rise seen in each layer of the device from UV and visible measurements for increasing input power.

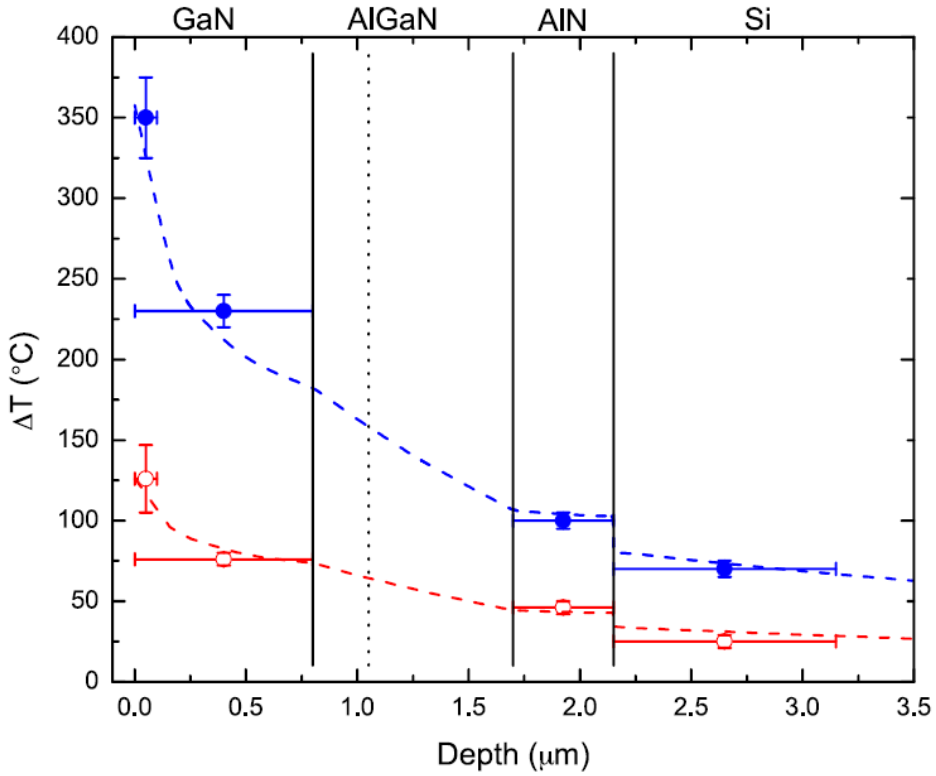

Figure 4.6 Temperature depth profile for the HEMT structure. Temperature rise as a function of vertical depth through the device with each material layer labeled. UV and visible Raman data are plotted for two specific input powers: ~7.8 W/mm (blue filled squares) and ~2.6 W/mm (red open squares). Thermal simulation data is incorporated for each drive condition, shown as dashed lines.

5. THERMAL CONDUCTIVITY OF CVD DIAMOND FOR NITRIDE APPLICATIONS

5.1 Abstract

In this chapter, experimental work is outlined involving the investigations of thermal conductivity, κ, in CVD diamond for its efficacy as a heat-spreading substrate in III-nitride electronic applications. Micro-fabricated heaters positioned over thin diamond (~ 1 μm) membrane structures on silicon substrates are used to measure in-plane thermal conductivity for diamond using UV micro-Raman spectroscopy. Thermal conductivity is first determined experimentally and then verified using finite element simulations incorporating an optimization approach for fitting the data and extracting values of κ as well as TBR.

5.2 Introduction and Overview

The issue of excessive self-heating in high-power electronics is a prominent one, leading to detrimental losses in output power and efficiency, as discussed in the preceding chapters. The use of diamond as a heat-spreading substrate for devices offers a promising potential for addressing these issues of thermal management. A diamond substrate provides a means of effective heat-dissipation very near the active region of the device where the greatest need for heat extraction is seen.

As discussed in the first chapter, diamond grown via chemical vapor deposition (CVD) has made significant strides in diversity of materials applications. In regard to applications for III-nitride technologies, the material property of particular interest is the thermal conductivity, κ. Natural diamond boasts one of the highest reported thermal

conductivities, upwards of 2000 W/mK with synthetic single-crystal capabilities in close competition [77]. For CVD diamond, however, the recorded values for κ are much lower – in the range of 20 – 500 W/mK for in-plane thermal conductivities and 80 – 800 W/mK for cross-plane thermal conductivities [66], [134]. This is partly attributed to the polycrystalline nature of the material causing poor thermal transport in the in-plane direction as well as the poor material quality within the first few hundred nanometers of the layer [66], [134]. The existence of higher grain boundary density, smaller grain sizes, and higher non-diamond carbon content in this region has been ascribed to hindering thermal conductivity in the cross-plane direction as well [135], [136]. Research efforts focusing on optimizing growth conditions and improving material quality for CVD diamond are important for the full potential of this material as an effective heat-spreading substrate.

The purpose of this chapter is to summarize a few of the on-going efforts for investigating thermal conductivities in CVD diamond and how these studies intend to further the development of thermal management technologies in III-nitrides. The studies presented below, involving diamond membrane heaters on silicon, were conducted with financial support and guidance from DARPA as part of a collaborative round-robin study of diamond thermal conductivities. The diamond and fabricated heater structures were provided by U.S. Naval Research Laboratory (NRL) in conjunction with this collaboration.

5.3 Experimental Description

Thermal conductivity test structures comprised of resistive micro-heaters fabricated on nano-crystalline diamond membranes were provided by NRL to study lateral (in-plane) heat transport in the diamond. The construction of the membrane is illustrated in Fig. 5.1(a). The supported membrane in the diamond film (~ 1-μm thickness) is formed by back-etching the silicon substrate directly beneath the line-heater, as illustrated in Fig. 5.1(b). The intention of this design is to encourage lateral heat flow away from the heater through the diamond and into the substrate at the edges of the membrane [66]. The use of these structures for thermal conductivity investigations have been recently explored [66], [137]. Some of the results presented here have also been recently submitted for publication [138].

By limiting heat flow to the lateral plane, the analysis of the experiment simplifies into a one-dimensional problem. The thermal conductivity, κ, can be determined from Fourier's law:

$$\dot{q} = -\kappa \nabla T \,, \tag{5.1}$$

where $\dot{q}$ represents heat flux in the lateral direction and the temperature gradient, ∇T, can be simplified to dT/dx in this case. To illustrate this, Fig. 5.2 shows a three-dimensional finite element model of the diamond membrane for power driven in the central heater. Fig 5.2(a) shows temperature rise across the membrane and Fig. 5.2(b) displays the lateral (x-component) heat flux. In the magnified cross section, the heat flux is largely constant in the positive x-direction, illustrating how this heater geometry restricts heat flow in the lateral dimension of the diamond toward the membrane edges. It is only near

the corners of the membrane where the y-component of the heat flux begins to contribute to dissipation away from the heater, as seen by a diminishing magnitude in the x-component value. Temperature measurements in the ± x-direction using micro-Raman spectroscopy result in a map of the temperature rise, dT, for changes in postion, dx, across the membrane. From this, the in-plane thermal conductivity (often denoted $\kappa_{||}$) can be readily determined using Eq. 5.1 [66], [138].

Micro-Raman measurements were accomplished using near-ultraviolet excitation with λ_L = 363.8 nm in a back-scatter configuration, similar to the setup described in Chapter Four. Temperature rise is determined from shifts in the diamond Γ(O) phonon energy, ω, according to $\Delta T = (\omega - \omega_0)/k_T$, where ω_0 is the phonon energy at ambient temperature and k_T is the Raman temperature coefficient in units cm^{-1}/K. Calibration of the Raman temperature coefficient is accomplished by heating the sample using a commercial stage and measuring the linear $d\omega/dT$ slope across a relevant temperature range for the subsequent membrane measurement.

For determination of κ, the line heater is driven using a probe stage and Keithley source meter and micro-Raman spectra are collected at various points across the membrane. The spectrum for each point is compared to the corresponding spectrum from that position with the heater off and a relative temperature rise is established for each point across the membrane.

5.3.1 Stress Considerations

Calibration measurements of $d\omega/dT$ are observed to differ when measured in the diamond over the suspended membrane compared to measurements over the silicon. The

difference is attributed to substrate-induced stresses, arising due to disparities in the coefficients of thermal expansion for diamond and silicon. To account for this, thermal stress (σ_{xx}) is incorporated into the calculation of net phonon shift:

$$d\omega/dT = k_T + k_S(d\sigma/dT)\,, \tag{5.2}$$

where the temperature (k_T) and stress (k_S) coefficients for the diamond are determined by first measuring the diamond phonon energy, ω, on the membrane and over the silicon substrate. Thermal stresses for the calibration conditions of uniform heating are simulated as a function of temperature to obtain a value for $d\sigma/dT$ both on the membrane and off the membrane, over the silicon. For these simulations, thermal expansion is simulated for heating the membrane structure under *ambient* conditions. It is worthwhile to note that these stresses are inherently different from those observed when power is driven in the heater. During operation, as the heat flux is not constant over the entire volume, the thermal expansion and stresses are much less uniform. Using the two values for $d\omega/dT$ and $d\sigma/dT$ for positions on- and off-membrane, we can determine k_T and k_S from Eq. 5.2. For a 200-μm membrane width, values of k_T = -0.015 $\pm$ 0.001 cm^{-1}/K and k_S = -0.50 $\pm$ 0.04 cm^{-1}/GPa are obtained. For a 400-μm membrane width, k_T = -0.018 $\pm$ 0.002 cm^{-1}/K and k_S = -1.17 $\pm$ 0.07 cm^{-1}/GPa. These coefficients are close to values seen in literature [139] with the differences in magnitude attributed to diamond layer quality.

5.4 Representative Results

Figure 5.3 displays the results for membrane measurements for two samples consisting of different test structure symmetries and membrane widths. For the symmetric heating profile in Fig. 5.3(a), 590 mW was applied across the heater and a temperature

profile is mapped across the 400-μm membrane, where a maximum temperature rise of ~250 °C is observed. Using the slope of temperature rise dT/dx from this graph, the known drive power, and membrane geometry, κ can be calculated using Eq. 5.1. For this analytical method, κ = 153 W/mK is obtained. For the 200-μm membrane with asymmetric heater in Fig. 5.3(b), a drive power of 406mW results in temperature rise of ~ 96 °C. For this case, Eq. 5.1 can be adjusted to account for an asymmetric heat flow, where approximately 86% of the power flows in the negative x-direction on the membrane (closest to the silicon membrane edge) and 14% in the positive x-direction. This calculation results in a value for κ ~ 124 W/mK.

5.4.1 Chi-Square Minimization and Confidence Intervals

To validate the assessment of κ from Raman measurements, two-dimensional finite element (FE) simulations using COMSOL Multiphysics were developed to model the temperature profile for the diamond membranes. Heat transfer and solid mechanics were the two major model considerations implemented to properly represent the lateral heat flow in the diamond and incorporate stress into the simulation. Because our efforts here are primarily focused on the in-plane κ, an anisotropic thermal conductivity was built into the material with vertical and horizontal components. To address the presence of an interface thermal boundary resistance (TBR), a "thin thermally-resistive layer" was integrated between the diamond and silicon in the model. To account for stress, realistic physical boundary conditions were used in the modeling with fixed-edge constraints on the outer model edges in the ± x-dimension and on the chip base (-y).

Optimization capabilities in the FE software were utilized to fit the experimental Raman data and extract values for in-plane κ and TBR between the diamond and silicon substrate. The results of this simulation are incorporated into the plots of Fig. 5.2 along with the resulting values for TBR and κ.

The plot in Fig. 5.4(a) displays collected data for a 200-μm membrane with a nominal diamond thickness of ~ 1 μm and symmetric heater arrangement driven at ~ 200 mW. The thermal conductivity κ^{FE} = 78.4 W/mK and TBR = 1.6 × 10^{-7} m^2K/W displayed in the plot are the values determined by the finite element optimization technique. For this sample, hexagonal boron nitride (h-BN) micro-particles were utilized as on-surface Raman temperature sensors across the membrane. The h-BN particles offer a stress-free avenue for making precise measurements of temperature at the surface of the diamond. Temperature rises measured from the h-BN particles are represented by blue data points in Fig. 5.4(a) and the corresponding thermal conductivity is displayed in the legend, with a value κ^{hBN} = 76 $\pm$ 8 W/mK. This work has recently been submitted for publication [138] and was accomplished in collaboration with Texas State colleague Brian Squires, M.S. to whom credit is given for the h-BN deposition and measurement procedures. Its application to this dissertation is in the implementation of custom FE simulation and data optimization for extracting values of κ, TBR, and χ^2 – the importance of the latter discussed below.

The optimization technique established for the FE simulations incorporates a Monte Carlo algorithm for minimizing a particular objective function in the model. For the case of this study, the simulation was configured to compute a chi-square minimization between the simulation results and direct Raman $\omega - \omega_0$ data at particular

positions along the planar dimension of the model. Briefly, chi-square minimization provides a means of establishing a *goodness of fit* between a collection of expected results and observed results. For a set of measurements comparing a plot of observed results $(x_i, y_i \pm \delta y_i)$ to a theoretical objective function $f(x_i, a, b, \dots)$ – where $a, b, \dots$ represent fitting parameters – chi-square (χ^2) can be mathematically described as

$$\chi^2 = \sum_{i=1}^{n} \left(\left(y_i - f(x_i) \right) \Big/ \delta y_i \right)^2 \quad . \tag{5.3}$$

The *reduced* chi-square is determined by $\tilde{\chi}^2 = \chi^2/(d-1)$, where d represents the degrees of freedom, which for data-fitting d = (number of data points) – (number of fitting parameters) [112]. In this work, the reduced chi-square, $\tilde{\chi}^2$ is used.

For our simulations, the objective function used to establish reduced chi-square is our Raman phonon energy shift, $\Delta\omega = k_T \cdot (T - T_0) + k_S \cdot \sigma_{xx}$, and the fitting parameters are κ and TBR. The optimization is accomplished by adjusting the value of κ and TBR in the material properties for the model until a minimum value for χ^2 is attained. As a result, the values for κ and TBR at which χ^2 is minimized result in a simulation which best fits the collected data from micro-Raman measurements.

The COMSOL software features a number of optimization algorithms with varying advantages depending on the application. The Monte Carlo method is advantageous for this experiment, compared to other algorithms, as it avoids unwanted local minima. In the Monte Carlo methodology, a *random seeding* routine is administered where a multitude of starting points (values of κ and TBR) are produced at which point the solver begins the minimization process in successive iterations. Once a minimum is

reached from each starting point, establishing a number of *local* minima, a more accurate estimation of the *global* minimum can be determined. This technique results in a more time-consuming simulation, but a more accurate minimization. An additional benefit for this procedure is that the iterative nature of the optimization yields a comprehensive table of κ, TBR, and χ^2 values for each step of the simulation [140].

This approach is also useful as it provides a means of validating the uncertainty in the simulated values through statistical confidence intervals. Figure 5.5 shows a contour plot representing the 90% confidence intervals for our fitting parameters κ and TBR. The shape of the contour is formed by the minimization process and the value at the edge is determined as in Ref. [140]. For the measurement corresponding to the 400-μm membrane in Fig. 5.3(a), the resulting uncertainties in experimental values are κ: (+ 24 / - 15) W/mK and TBR: (+ 1.5 / - 0.61) $\times$ 10^{-5} m^2K/W.

It is evident from the plot that the dependence of $\tilde{\chi}^2$ along the TBR-axis is very broad and most likely indicating that this method has a poor sensitivity to TBR, possibly due to the low temperature rise established at the membrane edges over the silicon. For the curve shown in Fig. 5.4(b), the χ^2 dependence is shown for which the confidence interval is determined in the κ-dimension alone, at a constant value for TBR = 1.6 $\times$ 10^{-7} m^2K/W. It can be seen that the dependence on κ is much less shallow, compared to that for TBR in the full contour in the inset of Fig. 5.4(a), resulting in a much-improved value for uncertainty in κ: +8.6 / - 5.1 W/mK.

5.5 Line Focus Experimental Approach

One area where improvement can be made for this measurement is in the micro-Raman experimental setup. The studies presented above utilize a *point focus* technique, where Raman spectra are collected in subsequent measurements across the full membrane while the linear heater is driven. Due to the polycrystalline nature of the diamond thin films, a considerable amount of uncertainty is present in the measurement as direct comparisons of ω for power-on vs. power-off conditions are difficult to replicate exactly at each x-position across the membrane. Additional concerns in stress variations across the membrane impart uncertainties in the point-to-point values of ω_0 at various positions.

The incorporation of a line focus method would contribute greatly to simplifying this approach. Preliminary efforts have begun involving the focus of the laser excitation in a line across the membrane, in which Raman signal can be obtained from each point across the membrane in a single measurement. This experimental setup provides a number of advantages over the point-focus method. It decreases the total measurement time, improving uncertainty due to possible fluctuations in drive power in the heater during the Raman measurement and limits the exposure time of laser excitation on the surface. With the laser intensity distributed along a line across the sample, the laser power density per unit area is decreased across the sample, lowering the risk of unwanted laser heating at each point on the membrane. Additionally, the line focus method provides a better assessment of comparisons between ω and ω_0 due to any variations as a function of position across the membrane.

Figure 5.6(a) illustrates the implemented line focus setup. The linear beam profile is created using a laser line-generator lens, or *Powell lens*, which causes the laser spot to

diverge in one direction with uniform spatial intensity along the diverging line. The laser is unaffected perpendicular to the diverging line direction. This is preferable to a simple cylindrical lens, which does not produce uniform intensity profile as the laser beam converges to a focus or diverges after passing through the lens. Focusing on the excitation and collection side is accomplished using cylindrical lenses to achieve a narrow line focus on the sample surface and guide a sharp, vertical collection line into the entrance slit of the spectrometer. This line is dispersed through the spectrometer and an area is illuminated across the pixel array of the CCD detector with the horizontal position corresponding to spectroscopic energy and vertical position corresponding to spatial position from the sample. Figure 5.6(b) shows a simplified sketch of the excitation branch of the setup for creating a vertical line across the sample. The optics produce a linear profile in the vertical direction (side view) and maintain a sharp focus in the horizontal direction (top view).

Figure 5.7 shows a collected CCD image using the line focus approach. Each vertical pixel exposed on the CCD corresponds to a spatial coordinate across the sample, or the membrane in this case. In the figure, diamond and silicon Raman peak positions are highlighted, demonstrating the presence of the suspended diamond membrane. The line heaters are also distinguishable in the image as gaps in the Raman signal/background.

Future work to improve this setup and data collection technique should prove to simplify the diamond membrane measurement in regard to total measurement time as well as yield greater precision in point-to-point comparisons of the Raman-measured temperature for power-on vs. power-off conditions.

5.6 Chapter Summary

Studies involving the investigations of thermal conductivity in CVD diamond are presented with a goal of providing a useful understanding of heat transport in this material for its potential applications in thermal management technologies. Diamond membrane structures on silicon substrates are used to explore the thermal conductivity of the thin (~ 1 μm) diamond and diamond/silicon TBR. UV micro-Raman measurements are used to map temperature rises across the diamond membrane to establish an analytical determination of the in-plane thermal conductivity. Finite element simulations are utilized for fitting the Raman data using a Monte Carlo approach and chi-square minimization technique. Preliminary work has been established for implementing a new experimental setup involving a line focus across the sample to improve the precision of point-to-point data acquisition in the thermal conductivity measurement.

5.7 Figures

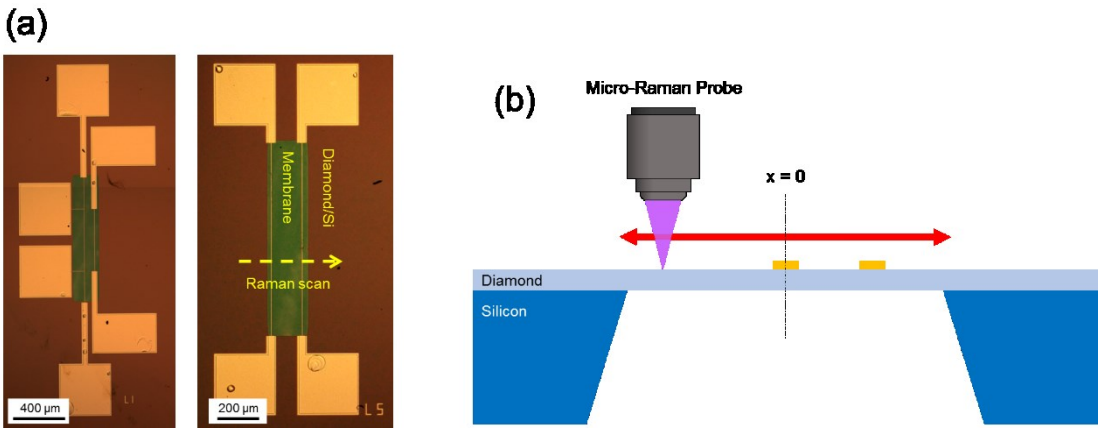

Figure 5.1. Diamond membranes on silicon. (a) Optical microscope images of two representative diamond membrane structures for symmetric and asymmetric heater geometries. (b) Illustration of the membrane in cross-section, demonstrating the UV Raman temperature measurement.

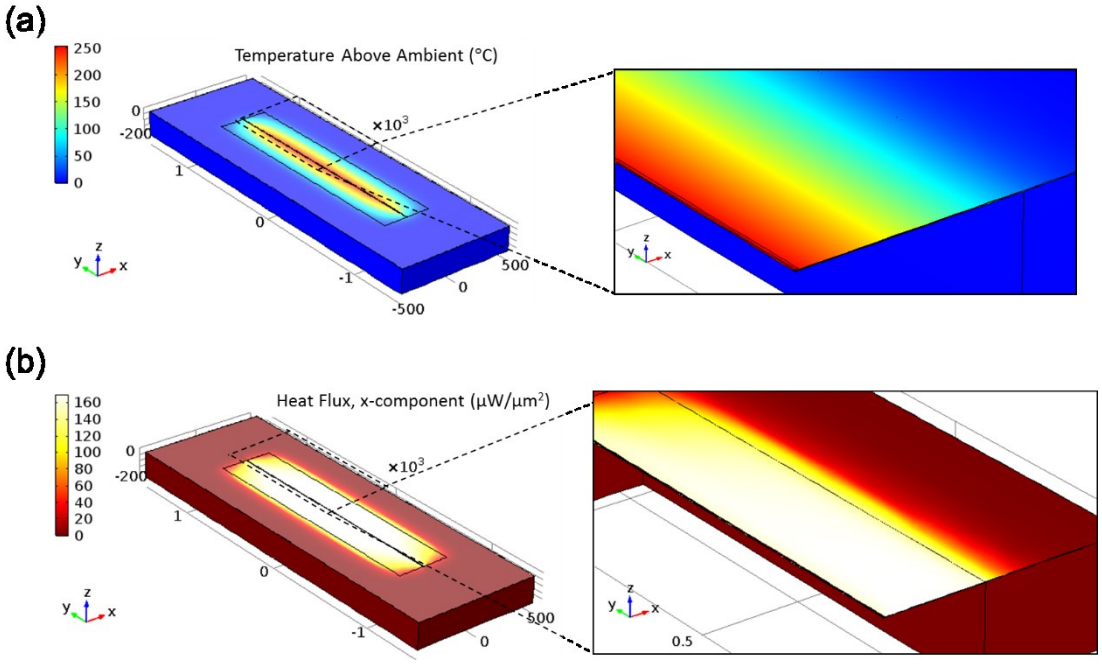

Figure 5.2. Model of temperature and heat flow on membrane. Three-dimensional finite element model of the membrane structure, displaying (a) temperature rise and (b) lateral (x) component of the heat flux for a current-driven line heater over the diamond membrane.

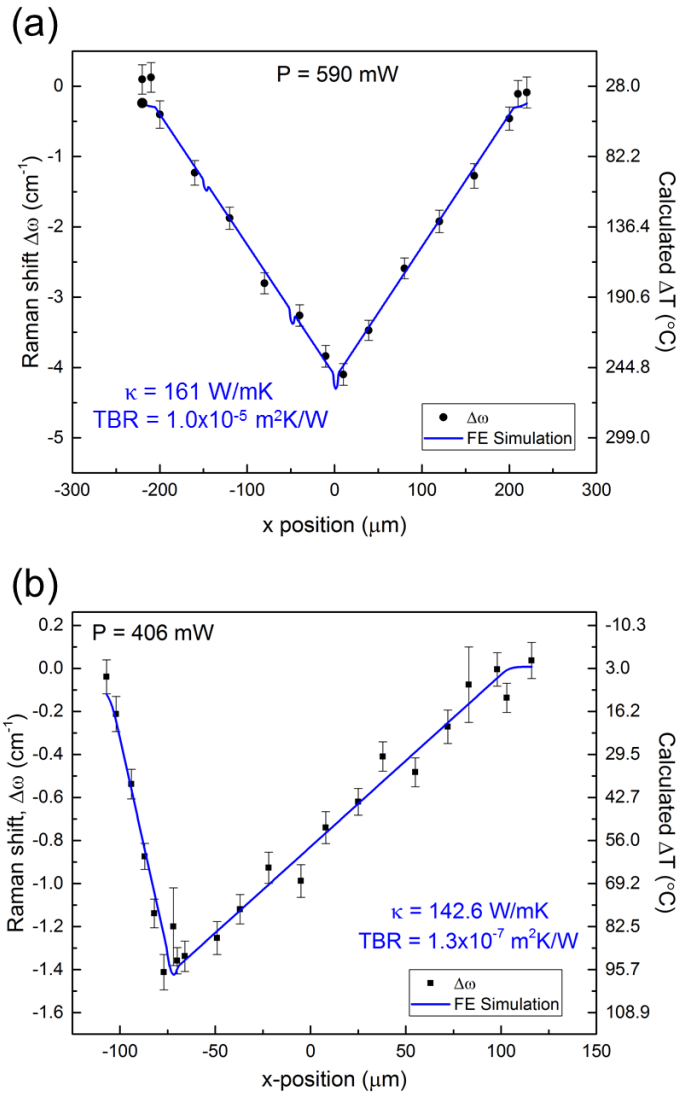

Figure 5.3. Raman temperature profile across membrane. (a) Micro-Raman results for temperature rise across the 400-μm membrane with symmetrical heater geometry. (b) Results for a 200-μm membrane with asymmetric heater geometry. Results from FE simulation are incorporated as a blue solid line in both plots with corresponding values for κ and TBR in blue text.

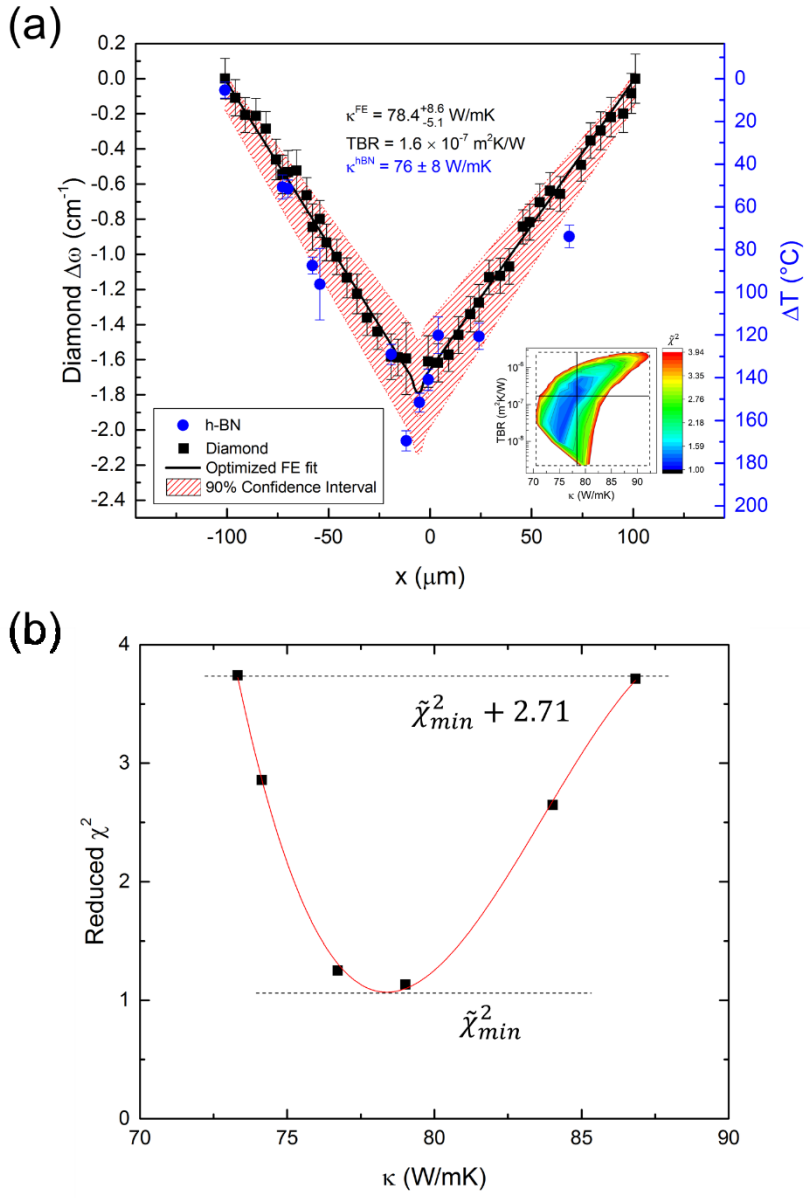

Figure 5.4. Simulation results for diamond membrane. (a) micro-Raman results for phonon shift and temperature rise in the diamond (black squares) across a 200-μm membrane for 200 mW drive power. The black line shows fitting from FE optimization. Also shown are the 90% confidence intervals for the fit with total contour plot for the confidence interval shown in the inset. The blue data points are temperature rise measured using h-BN microparticles on the diamond surface. Corresponding κ and TBR values are shown for both measurements. (b) The results of Monte Carlo simulations for $\tilde{\chi}^2$ vs. κ for a constant TBR = 1.6×10^{-7} m^{2}K/W.

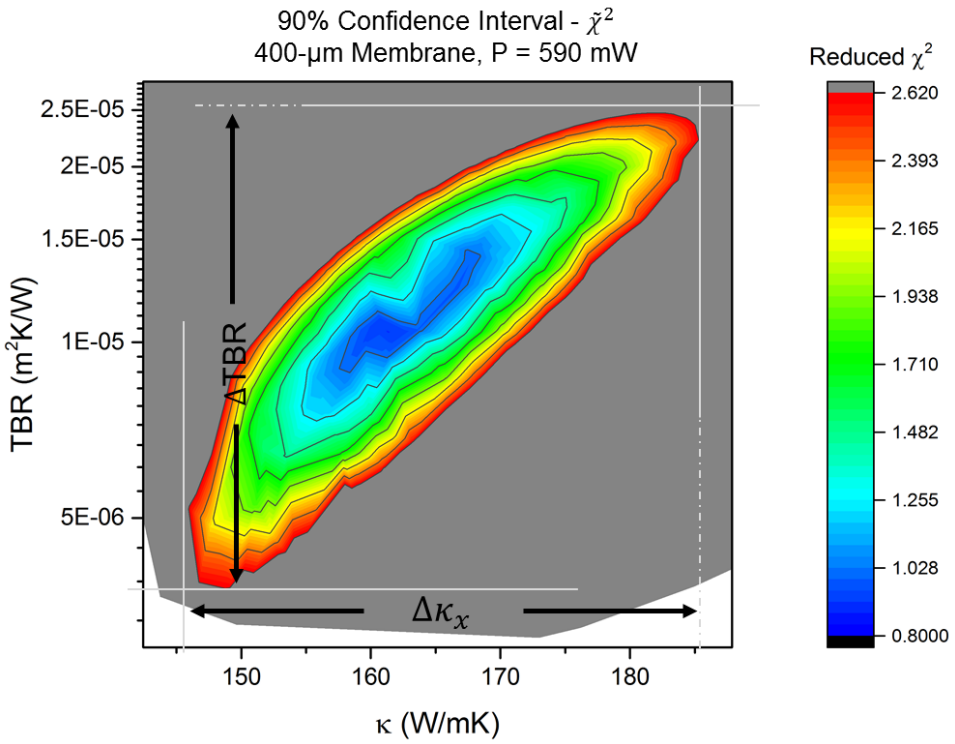

Figure 5.5. Confidence intervals from Chi-square minimum. Contour plot of the reduced chi-square, $\tilde{\chi}^2$, as a function of thermal conductivity, κ, and TBR for the 400-µm diamond membrane on silicon measurement. 90% confidence interval values are marked by $\Delta\kappa_x$ and ΔTBR in the figure.

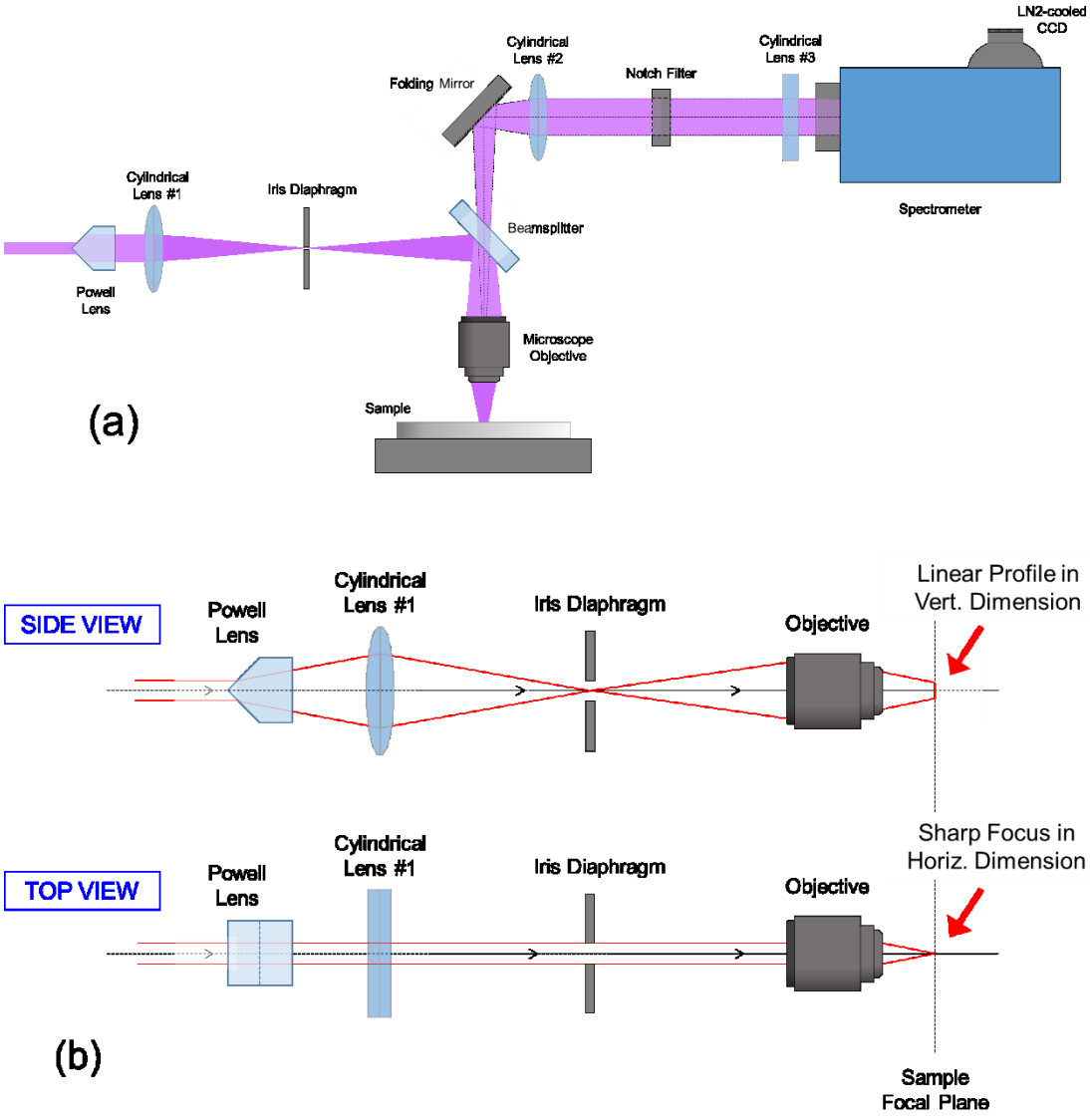

Figure 5.6. Line focus Raman experiment. (a) Drawing of experimental setup for line focusing micro-Raman setup. (b) Schematic of excitation branch for creating a line focus on the sample, illustrating the laser beam profile for the vertical (Side View) and horizontal (Top View) dimensions.

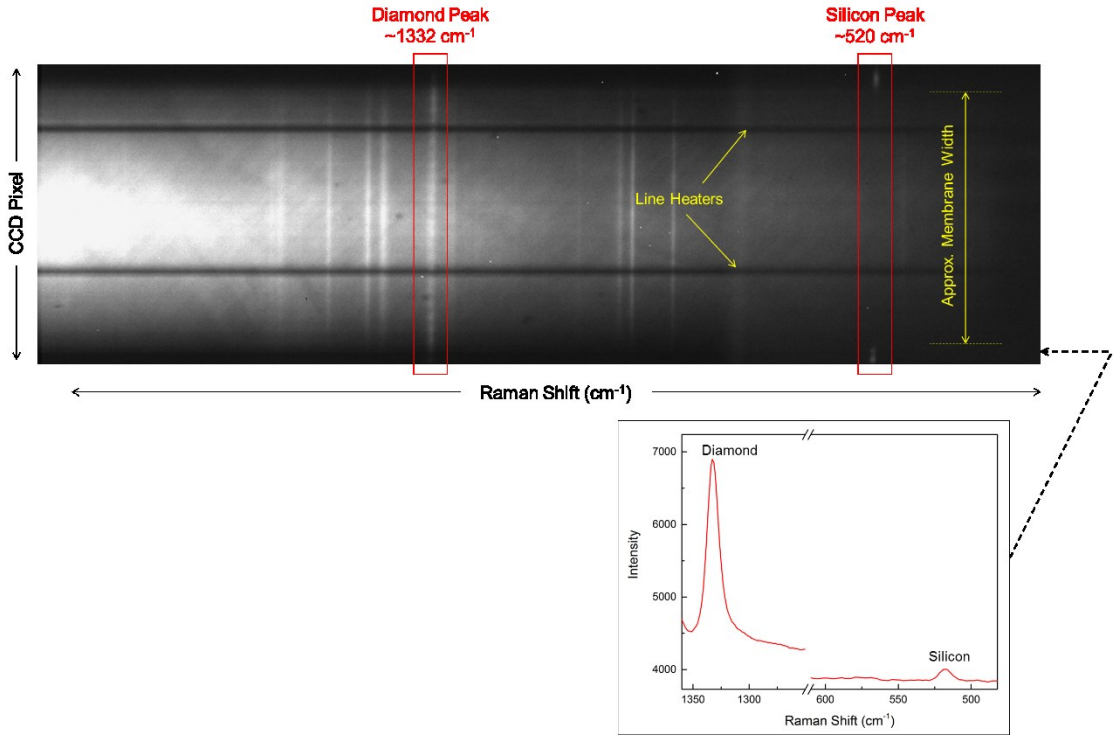

Figure 5.7. Preliminary results for line focus measurement. Collected CCD image from line focusing experiment for diamond on silicon membrane. The x-axis corresponds to Raman shift and y-axis pixels across the CCD, representing the spatial dimension of the scan. Also shown is a representative spectrum collected near the membrane edge, highlighting the peaks for diamond and silicon.

6. STRESS MAPPING OF GAN LAYERS ON DIAMOND USING MICRO-RAMAN SPECTROSCOPY

6.1 Abstract

In this chapter, investigations of stress distributions in GaN integrated with diamond grown by chemical vapor deposition is presented. Mapping of stress is accomplished using visible and ultraviolet (UV) micro-Raman spectroscopy across a 75-mm GaN-on-diamond wafer. The UV measurements are taken from both sides of the sample, and reveal a higher tensile stress at the free GaN surface compared to the stress near the GaN/diamond interface. This stress-gradient along the growth direction is unexpected for a uniform layer. Factors influencing the overall stress and stress gradient are understood based on relaxation from dislocations in the GaN which vary in density along the growth direction. Simulations incorporating a model for stress relaxation in the GaN elastic modulus adequately describe the observed dependence. Transmission electron microscopy (TEM) imaging reveals a discernable difference in the density of threading dislocations between the top and bottom regions of the GaN layer.

6.2 Motivation

Thermal management in electronics is currently the principle barrier to decreasing device size and increasing power densities. This is particularly the case in AlGaN/GaN high electron mobility transistors (HEMTs) where current flows within the < 10-nm thick two-dimensional electron gas. The resulting self-heating produces localized temperature rises as high as 350 °C [58]. Efforts for improving heat extraction from the active region,

such as incorporation of substrates with high thermal conductivity, have shown substantial promise for thermal management [141], [142].

Removing the growth substrate (e.g., Si) and integrating diamond as a heat spreader directly under the GaN layer for GaN-based devices is particularly attractive due to its high thermal conductivity (up to 2000 W/mK) when compared to traditional Si or 6H-SiC substrates [143]. Direct growth of diamond, using chemical vapor deposition (CVD), on device-quality GaN HEMT stacks has recently been demonstrated for wafer sizes up to 100 mm with diamond substrate thicknesses up to 100 μm [29], [141], [144]. As the scale-up processes for these wafers progress, investigations addressing the effects of growth methods on material quality are essential for future device development.

The focus of this study is to examine mechanical stresses and stress gradients present in the GaN layer for device-quality GaN-on-diamond, including full wafers, to understand the causes for observed variations in the through-layer stress across the wafer. Much of the work in this chapter has been recently reported in Ref. [84].

Stresses in III-nitride films and heterostructures arise from lattice mismatch and differences in the coefficients of thermal expansion (CTE) between the diverse layers during high-temperature processing [102]. Subsequent processing and development steps, such as the deposition of adhesion/passivation layers (e.g., SiO_2, SiN_x), wafer bonding to sacrificial handle wafers, and the growth of CVD diamond also contribute additional stresses to the epitaxial layers. The effects of stress on the material quality and ultimate device performance have been investigated; concerns include layer cracking [145], bow/warping [101], and changes in the electrical behavior for HEMTs [146]–[148].

6.3 Experimental Procedure

6.3.1 Visible and Ultra-violet Raman Spectroscopy

Raman spectroscopy is a non-contact, non-destructive method which can be used for measuring stress in GaN layers. With micron lateral resolution, micro-Raman techniques are advantageous for spatial mapping of non-uniformities and material quality across fabricated wafers. Biaxial compressive (< 0) and tensile (> 0) stresses σ_{xx} in the GaN layer are readily observed through blue (red) shifts in the Raman-active E_2^2-symmetry phonon [101]–[103]. The majority of micro-Raman investigations has been carried out using excitation in the visible wavelength range. Because GaN is transparent to visible light, these studies provide an average of the stresses throughout either the thickness of the GaN layer or within the beam waist of the focusing objective for thick materials.

In contrast, the optical penetration depth of the 363.8-nm near-UV excitation used here is 100 to 130 nm in GaN [123]. Performing measurements at this wavelength from each side of the finished wafer allows stress determination in the GaN near the AlGaN/GaN surface (denoted *GaN side*) and through the transparent diamond layer to interrogate the GaN at this interface (denoted *GaN/D side*). These studies are used to produce a map through coordinated measurements on a 10-mm grid from each side of the wafer with < 0.5-mm positioning precision, as illustrated in Fig. 6.1(a,b). By combining the UV results with visible (514.5 nm) micro-Raman measurements, we obtain, respectively, a stress map of the GaN and GaN/D sides and of average stress through the layer. Details of the UV micro-Raman apparatus are described in previous chapters and in [58].

6.3.2 Sample Preparation

The 75-mm wafer investigated was provided by Element Six, consisting of a CVD diamond substrate grown on AlGaN/GaN HEMT device layers grown separately by metalorganic CVD. The material stack is illustrated in Fig. 6.1(c). The GaN-on-diamond fabrication has been previously described [32]. Briefly, the GaN-side of the AlGaN/GaN-on-Si wafer is bonded to a sacrificial handle wafer. The silicon substrate and transition layers are then removed and a dielectric layer deposited on the exposed GaN to facilitate diamond seeding. The thick (~ 100 μm) polycrystalline diamond is grown via microwave-enhanced CVD. The handle wafer is then removed, resulting in a standalone GaN-on-diamond wafer.

6.4 Results

Typical UV micro-Raman spectra in Fig. 6.2, obtained from the GaN- and GaN/D-sides of the wafer, show the allowed E_2^2 and A_1(LO) phonons. The broad background originates from photoluminescence (PL) from the GaN. Incident excitation power at the sample surface was ~32 μW. When focused to a ~ 3 μm diameter spot, the corresponding power density is within the range of negligible laser heating [58]. Peak positions ω are determined by fitting Lorentzian functions to the data with typical uncertainty $\pm$ 0.1 cm^{-1}. Shifts from the un-strained phonon position, $\omega - \omega_0$, are used to determine biaxial stress values

$$\sigma_{xx} = (\omega - \omega_0)/\, k_R\,, \tag{6.1}$$

where k_R is the Raman stress factor. For the E_2^2 phonon we use $k_R^{E_2^2}$ = -3.4 $\pm$ 0.3 cm^{-1}/GPa [101], [103] and ω_0 = 567.3 $\pm$ 0.1 cm^{-1} measured from a strain-relaxed 55-μm GaN film. Uncertainty in the stress originates from the peak energies and k_R.

Figure 6.3(a) shows the map of E_2^2 phonon energy from the UV micro-Raman measurements from the GaN and GaN/D sides of the wafer. A red shift from ω_0 is observed in both cases. Moreover, a significant difference is observed in values obtained from the two sides of the GaN. The right-hand axis shows calculated stress from the E_2^2 peak position using Eq. 6.1. The resulting map reveals a significant gradient in the tensile stresses between the top and bottom interfaces of the GaN layer. The GaN-side tensile stress ranges from 0.67 to 1.0 GPa, with average value 0.86 GPa. For the GaN/D side, the tensile stress ranges from 0.075 to 0.37 GPa with average value 0.23 GPa. Typical uncertainties for the individual data points are $\pm$ 0.09 and 0.05 GPa for measurements from the GaN and GaN/D sides, respectively. The corresponding standard deviations in the mean stresses from the two manifolds are 0.07 and 0.06 GPa. As mentioned above, a large stress gradient is not expected for a uniform thin film.

The peak position map from visible micro-Raman measurements of the E_2^2 phonon is shown in Fig. 6.3(b), along with the corresponding stress values on the right-hand axis. The tensile stress from these measurements ranges from 0.12 to 0.44 GPa, plus one point at -0.04 GPa. An average tensile stress of σ_{ave} = 0.32 GPa was obtained across the wafer with uncertainty values of individual data points $\pm$ 0.06 GPa and standard deviation of 0.10 GPa from this map. At this laser wavelength, the measurement represents a volume-(thickness-) weighted average stress throughout the 730-nm thick GaN layer. This is in

contrast with the UV measurements, which provide stress values within the first 100–130 nm for the GaN and GaN/D sides.

6.5 Data Analysis and Simulations

6.5.1 Thermal Expansion

Processing of the GaN-on-diamond wafer involves multiple high-temperature steps [29] which may contribute to thermal strain between adjacent layers. Biaxial thermal stress, σ_{xx}, due to CTE differences between a deposited film and substrate can be described by Stoney's equation [149]

$$\sigma_{xx} = \frac{E_{film}}{1-\nu_{film}} \int_{T_0}^{T} \left[\alpha_{substrate}(T') - \alpha_{film}(T')\right] dT' , \tag{6.2}$$

where E_{film} is the Young's modulus, $\alpha_{substrate(film)}$ is the temperature-dependent CTE value for the substrate (film), ν_{film} is the Poisson ratio [101], [150], and T_0 (T) is the initial (final) temperature, subsequently reaching ambient T. To describe stress in our multi-layered scenario, we carried out finite element (FE) simulations using COMSOL Multiphysics. Because cooling in the fabrication steps covers large ranges in temperature, temperature-dependent CTE values were employed for each material in the simulations, using values along the a-axis for $\alpha_{GaN}(T)$ [150]–[154].

6.5.2 Two-Layer Finite Element Model

Simulations of a uniform GaN layer after high-T processing results in uniform thermal stress, as expected. The counterintuitive stress gradient, obtained via UV micro-Raman, suggests a variation in the GaN material properties may be responsible for the gradient. One plausible candidate is the ubiquitous presence of threading dislocations

(TDs) in the GaN. TD densities are known to vary considerably along the growth direction in GaN [155], [156]. It has been previously shown that *global* relaxation of biaxial strain in GaN is attributable to *local* relaxation near threading dislocations [101]. Assuming strain is relaxed in the immediate proximity of a TD, with characteristic length L, an average relaxation factor may be supposed

$$f = nL^2 \,, \tag{6.3}$$

where n represents the TD area density. The resulting mixture of "ideal" GaN interspersed with microscopic, relaxed regions has an effective elastic modulus

$$E_{GaN}^{eff} = (1 - f)E_{GaN}^{bulk} \,, \tag{6.4}$$

where E_{GaN}^{bulk} represents the *un-strained* elastic modulus for the material [157]. For GaN we use E_{GaN}^{bulk} = 324 GPa and $\nu = 0.2 \pm 0.02$ [101], [102]. The relaxation effects of Eq. 6.4 were incorporated into the simulations using f as a fit parameter for the GaN and GaN/D regions of the layer. Because we have two stress values from the UV (σ_{GaN} and $\sigma_{GaN/D}$) plus the average stress (σ_{ave}) from visible micro-Raman measurements, we adopt a simple model comprised of two regions with different relaxation factors and thicknesses denoted t_1 and t_2. This is reasonable for MOCVD-grown GaN in which the final (device) regime (thickness t_1) is typically less defective than the initial growth stages (t_2) adjacent to the transition layers [158]. Our model consists of three parameters (f_{GaN}, $f_{GaN/D}$, and t_1 or t_2, where $t_1 + t_2 = t$ = 730 nm) which are determined based on the three measured stress values. We estimate t_1 using

$$\sigma_{ave} = \left(t_1\sigma_{GaN} + t_2\sigma_{GaN/D}\right)/(t_1 + t_2) \,. \tag{6.5}$$

From this we determine t_1 = 100 $\pm$ 10 nm and t_2 = 630 $\pm$ 90 nm. Using these values, and incorporating Young's modulus from Eq. 6.4, the stress cross-section may be simulated to determine the remaining unknown relaxation factors f_{GaN} and $f_{GaN/D}$.

The step-by-step wafer fabrication was simulated to recreate the effects of thermal expansion at each major stage of the process upon cooling to room temperature: nitride MOCVD growth (~1100 °C), wafer bonding (~700 °C), and diamond CVD growth (~800 °C). Because the thicker layers play the dominant role in the overall thermal stresses, it is sufficient to only incorporate the silicon, diamond, and GaN layers into our simulations. Figure 6.4 shows the layered material stack used in the two-layer FE simulation here, magnified to properly display the thin layers. The GaN layer is divided into two layers, a *GaN* region and *GaN/D* region, to incorporate the effects of stress relaxation in each major portion of the full layer. The stresses shown in the color legend to the right are the results of the simulation following the growth of the CVD diamond substrate and cooling back to room temperature. Notice the handle wafer is still present in this step of the simulation, as would be the case for the realistic processing step.

By implementing the effective elastic modulus from Eq. 6.4, a major gradient in the stress across the GaN layer was seen in each step of the simulation. This implies that stress relaxation due to TDs is present from the initial phase of the wafer, i.e., following MOCVD growth of the nitride layers. The range of experimental stress values for UV and visible micro-Raman is shown in Fig. 6.5 using patterned rectangles with the vertical dimension corresponding to the standard deviations from each map and the horizontal dimension representing the optical probe depth for each particular measurement. Figure 6.5 presents the resulting simulated σ_{xx} as a function of vertical material cross-section.

The abrupt shape of this dependence is due to the simple two-region model used here. Good agreement with the measured stress is obtained using relaxation factors of $f_{GaN/D} = 0.76$ in the GaN close to the GaN/D interface and $f_{GaN} = 0.095$ near the AlGaN-GaN interface.

6.5.3 Electron Microscopy

The presence of TDs is confirmed using bright-field TEM imaging. A cross-section was prepared for TEM imaging by focused ion beam (FIB) milling. The sample was milled to electron transparency at 30 kV followed by polishing steps at 5 and 2 kV before being transferred to the TEM for imaging. Credit is due to Texas State colleague Jon Anderson for his assistance in sample processing and imaging. A representative image from the cross-section is shown in Fig. 6.6(a).

TDs are observed in the GaN layer with higher density on the GaN/D side. Approximate densities in both regions were accomplished by counting TDs across a cumulative TEM montage approximately 5 μm in length. An image of the entire sample studied is shown in Fig. 6.6(b); to create the montage for TD density calculations, images were obtained at higher magnification – such as shown in Fig. 6.6(a) – along this sample, to preserve image resolution and increase accuracy of the estimation. This approximation gives estimated values of 1×10^9 cm^{-2} and 9×10^9 cm^{-2} for the GaN and GaN/D portions of the layer, respectively. These are in agreement with prior work for GaN grown on silicon using MOCVD [159]. Within our analysis, the ratio $f_{GaN/D}/f_{GaN} \sim 8$ should be correlated with the relative TD densities ~ 9. This agreement is satisfactory given that the values are obtained using very different approaches.

6.5.4 Modeling Defects in GaN

Using the TEM estimates of density n and the f parameters from our simulations, Eq. 6.3 allows us to estimate $L \sim 100$ nm corresponding to the lateral size of the relaxation region surrounding the TDs. This value is comparable to previously published $L \sim 400 \pm 300$ nm obtained via studies of the temperature-dependent tensile stress in GaN grown on 6H-SiC [101]. To investigate the impact of L, FE simulations were carried out for a model of a single threading dislocation under thermal stress. The results of this, shown in Fig. 6.7, demonstrate the effective region of stress relaxation surrounding a single threading dislocation to be 100-200 nm across, in reasonable agreement with what was determined experimentally.

In the same regard, we explored the effect of microscopic voids at the GaN/diamond interface. To assess the possible consequences of these types of defects on the stress mapping measurements, FE simulations were accomplished to model the local effects of a void in the GaN-on-diamond complex. Figure 6.8(b) shows the stress results for the thermal expansion of the GaN on its initial silicon substrate during the step of original MOCVD nitride growth. This step in the GaN-on-diamond fabrication process was chosen to model for simplicity. The results for the same region of the model are displayed in Fig. 6.8(c) for the addition of a ~100 nm void at the GaN/substrate interface. From this it is apparent that the presence of a void in the GaN imparts a small rise in stress in the local regions surrounding the defect, but has little effect on the global stress average for the layer, as would be measured optically.

While the simple analyses here do not present an exhaustive evaluation of these defects, it does offer confidence to the results acquired from micro-Raman for average stresses measured across the 75-mm wafer.

6.6 Raman A_1(LO) Phonon Analysis

Lastly, we turn our attention to observed shifts in the A_1(LO) phonon energy. The mapping results of the A_1(LO) phonon for UV Raman are shown in Fig. 6.9. Using the Raman-stress factor for this phonon, $k_R^{A1(LO)} = -2.14 \pm 0.28$ cm^{-1}/GPa [103], and the stress-free reference frequency $\omega_0 = 733.9 \pm 0.1$ cm^{-1}, we estimate the stress-induced shifts on the GaN and GaN/D sides of the wafer. For the GaN-side, we expect a shift of -1.8 $\pm$ 0.2 cm^{-1}. The measured A_1(LO) shift is -2.1 $\pm$ 0.2 cm^{-1}, where the uncertainty is the standard deviation from our map measurements. The stress-induced and measured shifts are within total uncertainty of each other. For the GaN/D side, we expect a shift of -0.5 $\pm$ 0.1 cm^{-1} due to stress alone. However, the shift observed for the GaN/D side A_1(LO) phonon is +1.5 $\pm$ 0.5 cm^{-1}. This corresponds to a total discrepancy of ~ 2 cm^{-1}.

A plausible explanation for this blue shift is the presence of free carriers due to unintentional doping during the wafer processing [23]. In the presence of free carriers, phonon-plasmon coupling will blue shift LO phonons [160]. We estimate a carrier concentration ~ (1.88 $\pm$ 0.79) $\times$ 10^{17} cm^{-3} in the region near the GaN-diamond interface [160]. Possible sources for this unintentional doping are diffusion from the dielectric adhesion layer, from hydrogen which is present during CVD diamond growth, or from exposure during processing steps such as removal of the nitride transition layers [161].

6.7 Chapter Summary

To summarize, spatial mapping of stresses across a 75-mm GaN-on-diamond wafer was accomplished using visible and UV micro-Raman spectroscopy. Utilizing the shallow penetration depth of UV excitation and probing both sides of the wafer, E_2^2 phonon shifts yield average tensile stresses from the top and bottom 100 – 130-nm regions of the GaN buffer layer of 0.86 ± 0.07 GPa and 0.23 ± 0.06 GPa, respectively. These measurements reveal an unanticipated stress gradient between the top and bottom interfaces of the 730-nm GaN layer. FE simulations are used to incorporate the presence of threading dislocations in the GaN, with different densities in the GaN/D and GaN sides of the wafer. UV and visible micro-Raman results are well-described by the simulations with relaxation parameters as the only fit variables. UV Raman measurements of the A_1(LO) phonon suggest the presence of unintentional dopants on the GaN/D side subsequent to the multiple high-temperature processing steps that follow the GaN MOCVD growth.

6.8 Figures

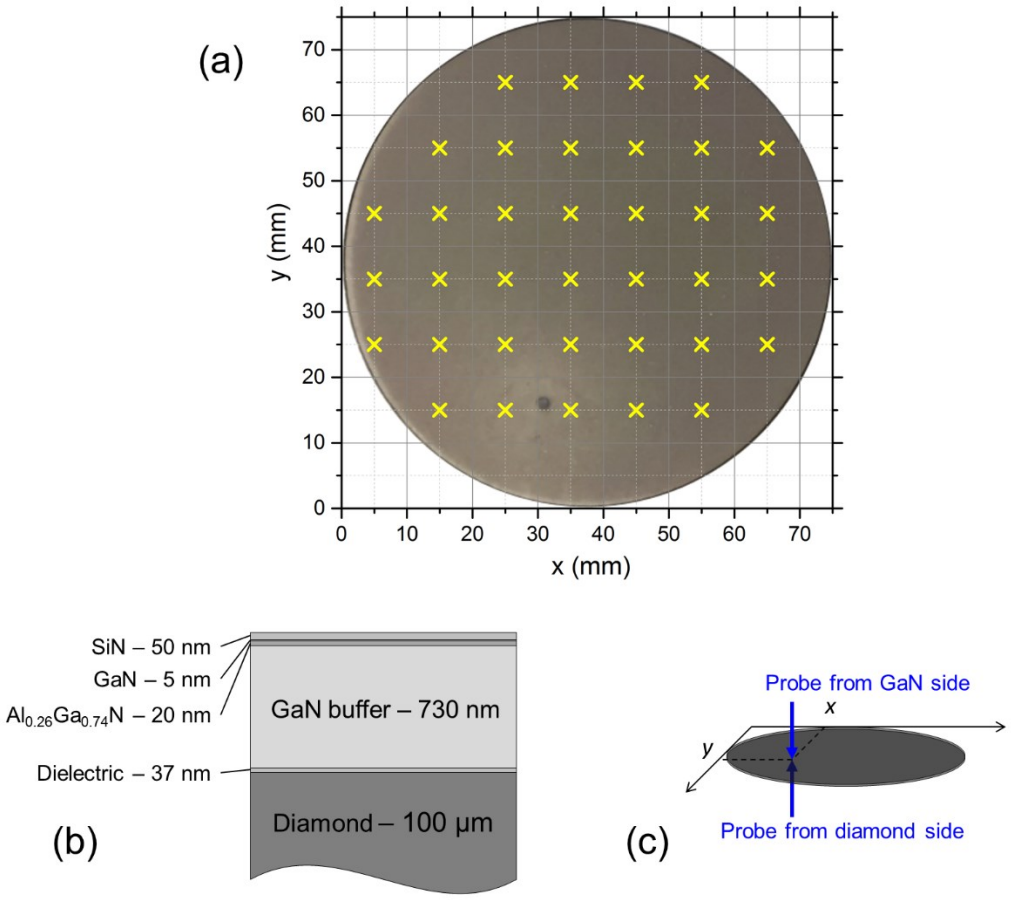

Figure 6.1. GaN-on-diamond wafer. (a) 75-mm wafer studied showing coordinate system used for stress mapping with "x" denoting measurement positions. (b) Depiction of wafer material stack with thicknesses shown for each layer. (c) Illustration of probing from either side of the wafer using near-UV excitation for UV micro-Raman

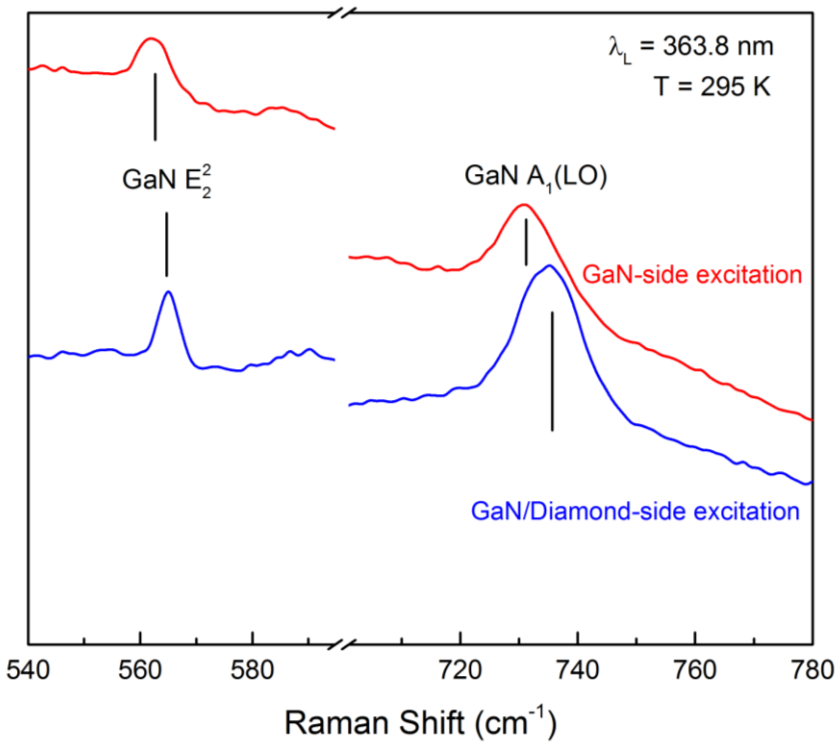

Figure 6.2. Typical UV micro-Raman spectra at room temperature. The spectrum for measurements with excitation from both sides of the wafer are shown, demonstrating the GaN E_2^2 and A_1(LO) phonons used to map stresses in the layer.

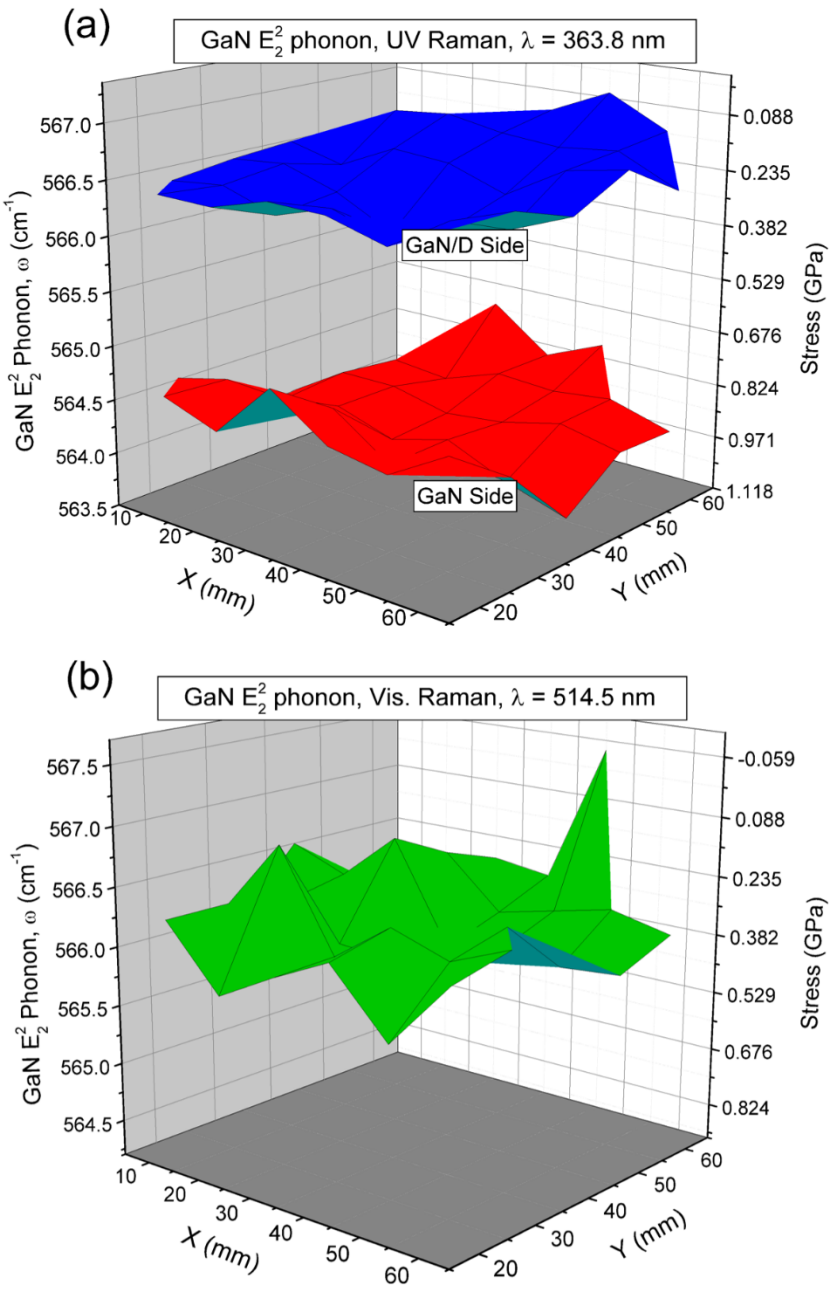

Figure 6.3. Micro-Raman full-wafer stress map. Map of the E_2^2 phonon energy from micro-Raman measurements using (a) UV and (b) visible excitation. The upper and lower surface manifolds in (a) correspond to measurements from the GaN/D and GaN sides of the wafer, respectively. The right-hand axis in both graphs show the calculated stresses for each measurement.

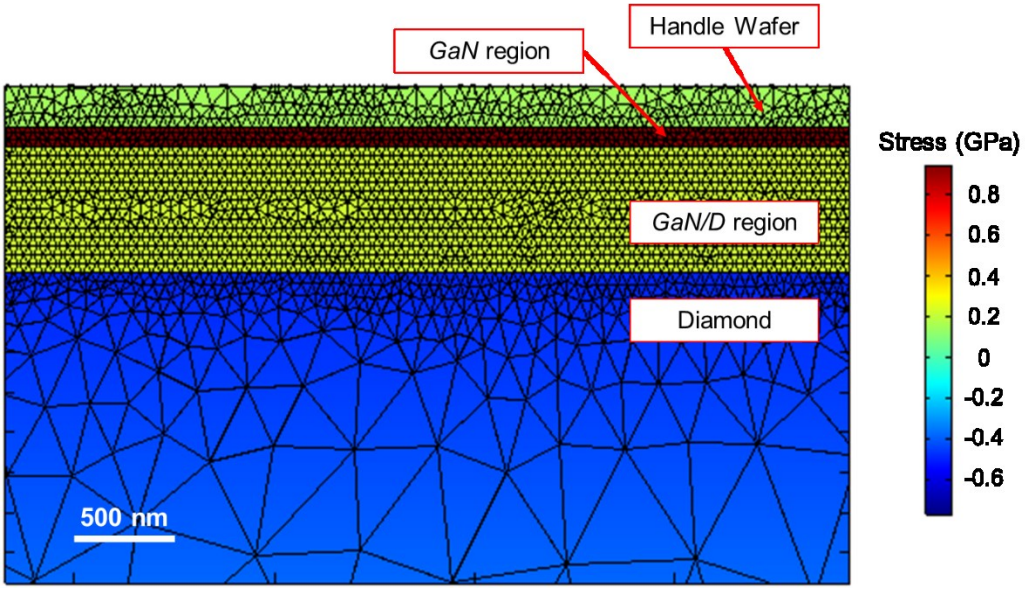

Figure 6.4. FE model for thermal expansion in GaN-on-diamond. Image of the material stack used (magnified to display all layers) in the COMSOL finite element simulation of thermal expansion for the two-layer model of stress-relaxation.

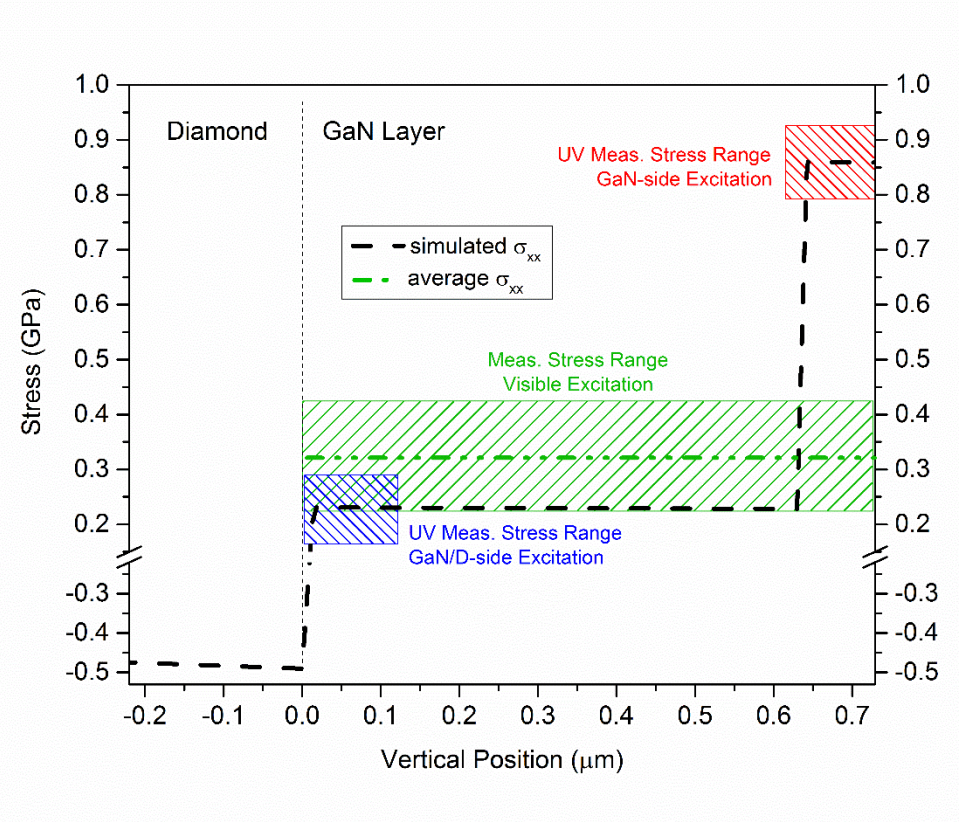

Figure 6.5. Comparison of data to simulation. Results from FE simulation for stress along the vertical cross-section of the GaN-on-diamond wafer is shown as a dashed line. Measured stress values from visible and UV micro-Raman for each side of the wafer are shown as patterned rectangles with the vertical dimension representing standard deviations and horizontal dimension representing the depth optically probed for each measurement.

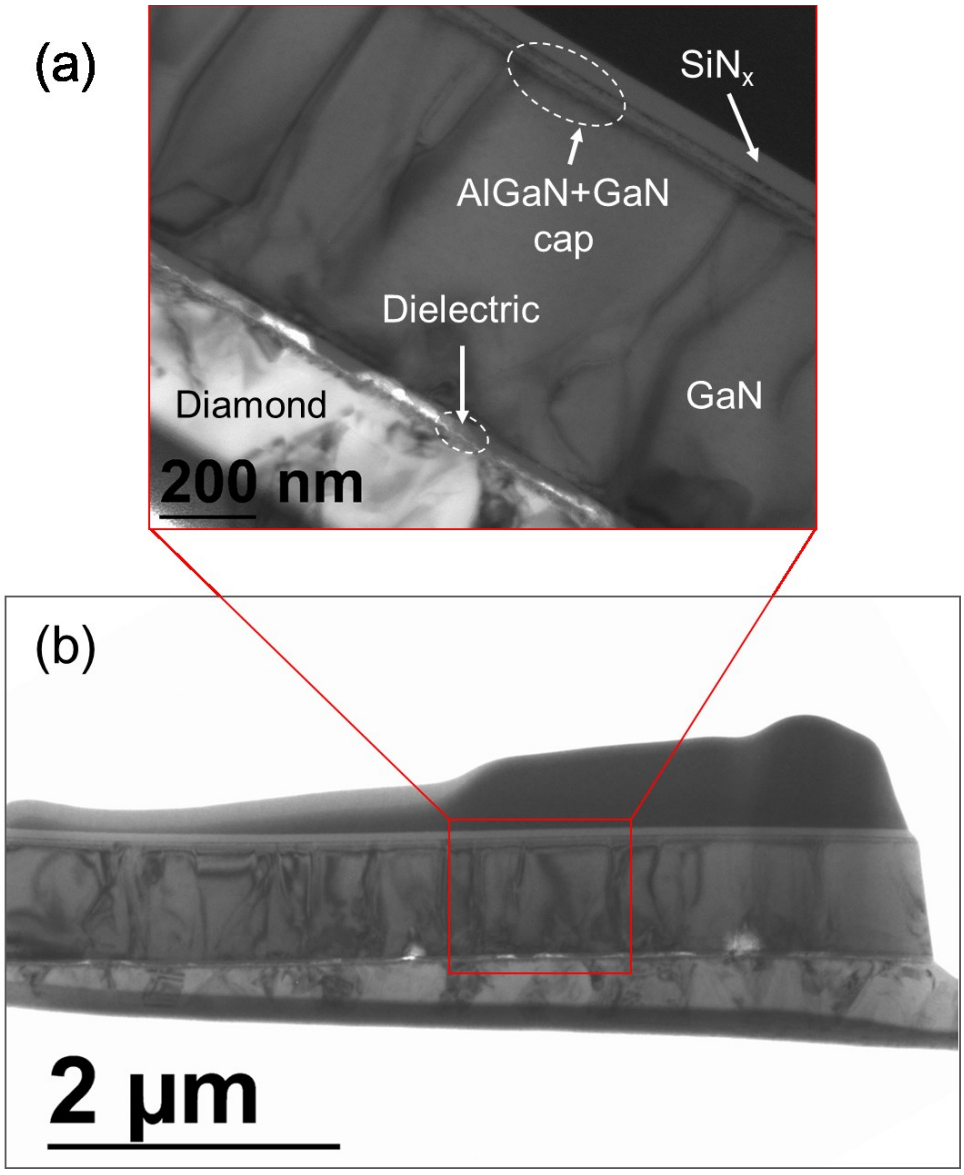

Figure 6.6. TEM cross-section of GaN-on-diamond layers. (a) Representative cross-section of the GaN-on-diamond wafer obtained by bright-field TEM with material layers identified. (b) Image of full sample prepared for microscopy by FIB milling.

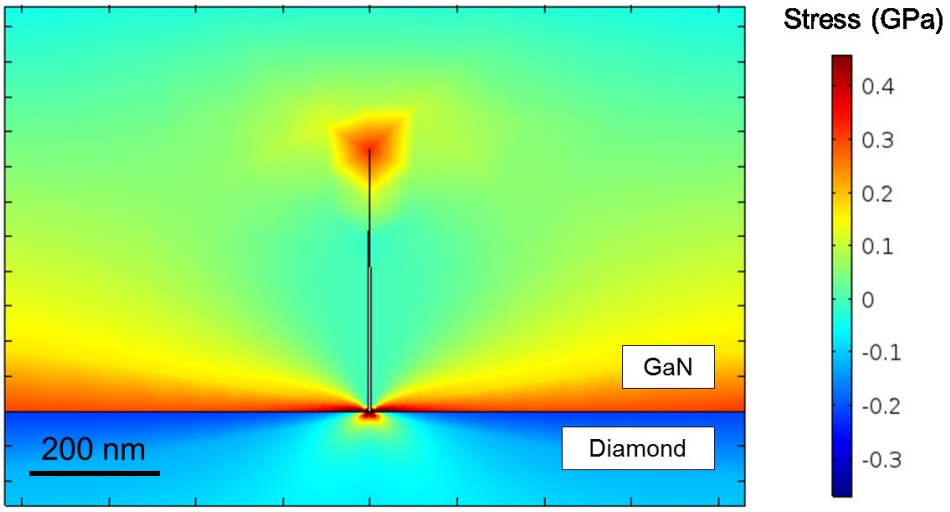

Figure 6.7. FE model for a dislocation in GaN. Magnified image of the model used to simulate the stresses and relaxation seen in the GaN layer surrounding a single linear dislocation.

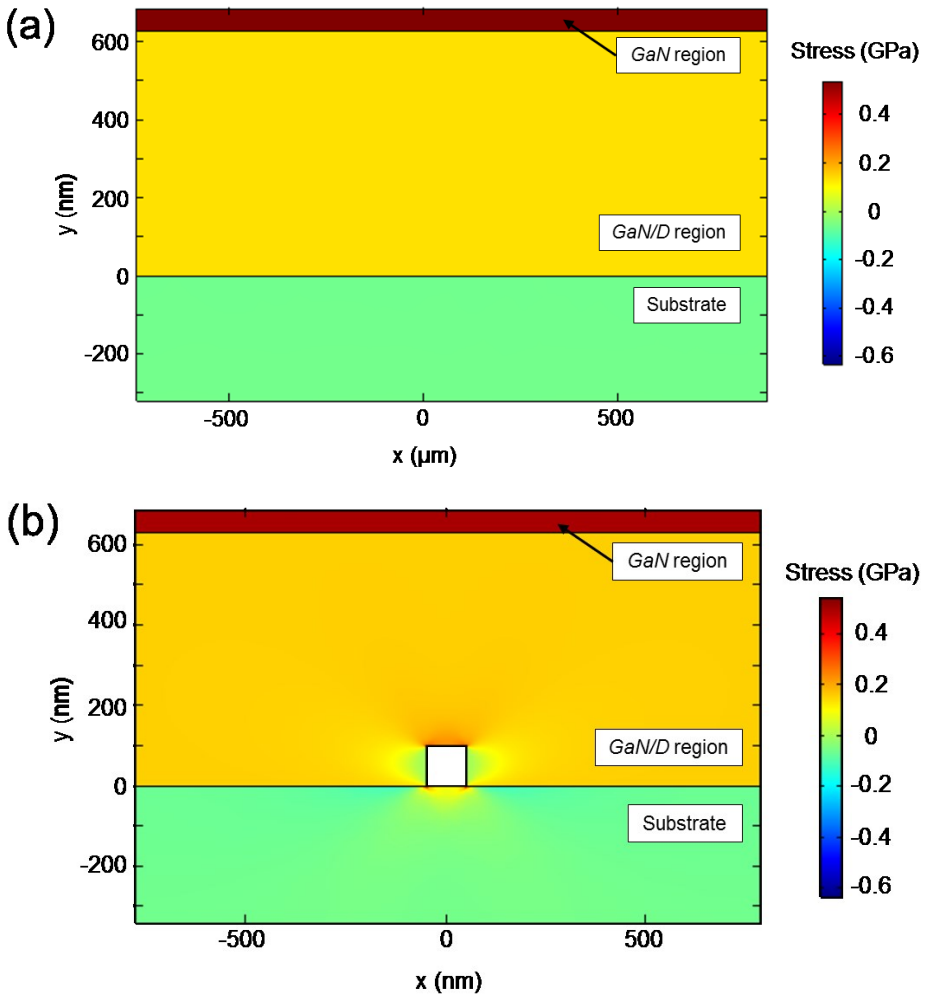

Figure 6.8. FE model for voids in GaN. (a) Results from FE model of GaN on silicon during MOCVD growth (b) FE results for same fabrication step as (a), but with the introduction of a 100-nm void at the GaN/substrate interface. FE results are magnified in geometric dimensions to properly display the thin GaN layers.

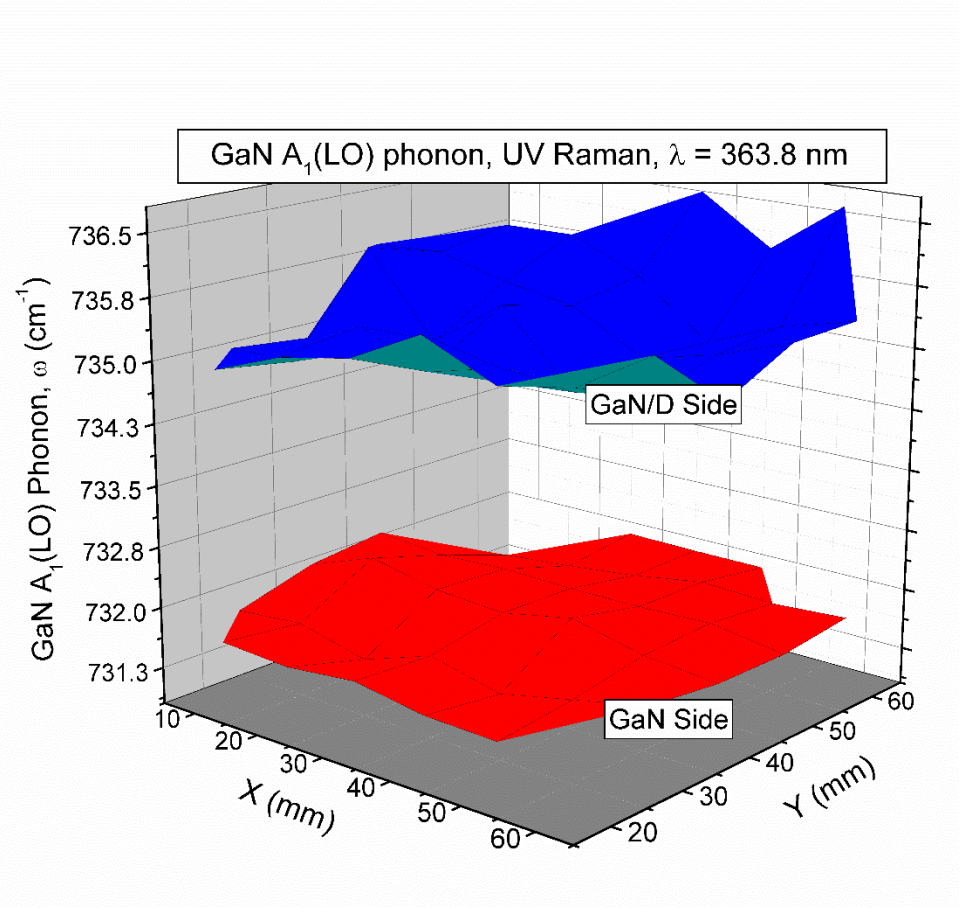

Figure 6.9. Micro-Raman map of GaN A_1(LO) phonon energy. Results for UV excitation from the GaN/D and GaN sides of the wafer represented by the upper and lower surface plots, respectively.

7. EFFECTS OF STRESS GRADIENT ON THE PHOTOLUMINESCENCE IN GAN-ON-DIAMOND

7.1 Abstract

The use of UV photoluminescence (PL) spectroscopy to accomplish stress mapping for a wafer consisting of diamond grown by chemical vapor deposition (CVD) on AlGaN/GaN high electron mobility transistor (HEMT) device layers is presented in this chapter. Measurements are performed from the top and bottom surfaces of the wafer to observe the stresses in the top (near the AlGaN-GaN interface) and bottom (near the GaN-diamond interface) regions of the GaN layer. A significant stress gradient of ~ 0.85 GPa is observed within the GaN layer, which is unexpected for a uniform layer. This gradient is potentially caused by stress relaxation near threading dislocations at the initial nitride growth interface.

7.2 Motivation

Techniques for proper thermal management have become a critical focus in research surrounding high-temperature and high-power electronics [24], [58]. In AlGaN/GaN high electron mobility transistors (HEMTs), the bulk of power production occurs within a sub-micron region near the device's two-dimensional electron gas (2DEG). This results in highly localized temperature rises, causing detrimental limitations to maximum operation power, output efficiency, and reliability. For this reason, it is important to develop improvements for heat extraction near the active region of these kinds of devices. Recent work has demonstrated the potential of heat-spreading substrates with high thermal conductivity for this capability in nitride device applications [30], [32], [141], [162], [163].

As mentioned in the chapters above, the use of diamond as a substrate for GaN HEMTs has been successfully demonstrated as an effective heat spreader due to its high thermal conductivity when compared to traditional growth substrates [19], [143], [164], [165]. This implementation has been shown using diamond grown by chemical vapor deposition (CVD) for GaN MOCVD layers via bonding or direct deposition for wafer sizes up to 100mm with substrate thicknesses up to 100 μm [29], [141], [144], [163].

Examination of material quality in this process is important to ensure the successful progression of this technique in future applications. Many of the steps involved in processing a GaN-on-diamond wafer involve large temperature differentials, leading to stresses and other non-uniformities (bow and warping) across the wafer. One root cause for underlying stress in the layers is the difference in thermal expansion coefficients between the GaN, silicon carrier, and diamond layers [144]. The initial epitaxy of the nitride MOCVD layers can also result in residual effects contributing to non-uniformities in the material quality, such as stress relaxation from threading dislocations in the thick GaN layer. Stress in material layers lead to difficulties in future device fabrication, as well as inhibit electrical performance in HEMTs [31], [166].

The study presented in this chapter focuses on the viability of optical techniques for monitoring the effects of wafer-scale diamond processing on the device layers for a free-standing GaN-on-diamond wafer, with the aim of identifying causes and potential issues arising from stress variations within layers across the wafer. The work here is intended to compliment the findings of the stress mapping using micro-Raman spectroscopy presented in the previous chapter, which was also reported in Ref. [84].

Results from studies in this chapter have also been recently submitted for publication [167].

Photoluminescence (PL) spectroscopy is a non-destructive, non-contact, optical characterization technique, for estimating band gap and material properties which affect the near-band edge states. The former is affected by factors such as stress, while the latter is influenced by defects and impurities. PL has proven to be a powerful tool for quantifying stress in GaN based on measurements of the peak energy [99], [102], [107]–[109]. The available lateral spatial resolution also qualifies this technique for micron-scale mapping of non-uniformities and material quality across fabricated wafers.

Above band gap UV excitation (λ = 291 nm) results in an optical penetration of ~ 65 nm in GaN [123], [168]. For this study, UV excitation allows the stresses in the GaN active layer to be measured near the top surface (near the AlGaN-GaN interface) and near the lower surface (near the GaN-diamond interface) by performing the measurement on either side of the finished wafer. This technique offers a look at the stress variations across the vertical profile of the material.

In-plane stress in the GaN, σ_{xx}, is determined from shifts in the measured peak position, E, in the PL spectrum, representing changes in the GaN energy band gap, E_g. A stress factor, k_{PL}, is utilized to evaluate the stress-energy relationship [103], [109]:

$$\sigma_{xx} = (E - E_0)/k_{PL}\,, \tag{7.1}$$

where E_0 represents the strain-free PL peak energy. We adopt the convention that $\sigma_{xx} > 0$ corresponds to a tensile stress. The values k_{PL} = 21.1 ± 3.2 meV/GPa and E_0 = 3.4180 ± 0.0008 eV from Refs. [107] and [103], respectively, were used in this study.

7.3 Experimental Procedure

The details of the 75-mm wafer investigated in this study and its fabrication process are described in the previous chapter, and is reported in Refs. [32], [84]. The GaN-on-Diamond wafer is created by first growing AlGaN/GaN HEMT nitride layers on a silicon substrate via MOCVD. A sacrificial carrier wafer is then bonded to the top side of the finished wafer and the silicon substrate is removed, along with the AlGaN transition layers, to expose the thicker (nominally 730 nm) GaN buffer layer. A thick layer (~100 μm) of polycrystalline diamond is grown on this surface via CVD using microwave-enhanced processes. The carrier wafer is then removed, leaving a standalone GaN-on-diamond wafer.

UV PL measurements were accomplished using a diode-pumped Ti:Sapphire femtosecond laser with a repetition rate of 8 MHz, frequency-tripled to 291 nm (4.26 eV). Excitation and collection were accomplished with a custom-built microscope using a 15X all-reflective objective with 0.4 NA and typical spot diameter of ~10 μm. PL spectra were collected using a 0.64-m spectrometer with a Hamamatsu R3809-50 microchannel plate photomultiplier and SR400 photon counter. The average laser power was maintained below 30 μW (0.40 μW/μm^2) at the focus on the sample to minimize local heating. Measurements were accomplished with excitation/collection on both the top-side (denoted *GaN side*) and bottom-side (denoted *GaN/D side*) of the GaN-on-Diamond wafer. As mentioned above, for λ_L = 291 nm, the optical penetration depth in GaN is approximately 65 nm [123], [168]. PL spectra were collected in 10-mm increments in an established x-y coordinate system, with < 0.5-mm spatial precision, to create a map of the observed stresses across the 75-mm wafer. Each PL spectrum is acquired in a single-

channel process with typical integration times of 1-2 seconds at each wavelength with a spectral resolution of ~ 0.2 nm (< 3 meV).

7.4 Results and Discussion

Typical PL spectra are shown in Fig. 7.1, for collection from both the GaN- and GaN/D-side of the wafer at room temperature. A shift in peak energy between each curve is visible from the graph, demonstrating the difference in stresses at each interface in the GaN layer. The GaN/D curve in Fig. 7.1 exhibits a PL shoulder previously reported in room temperature GaN measurements [106], [107], [109]. This has been attributed to the first phonon replica in GaN at ~60 meV from the strong near-band edge peak [122], [144], [169].

Due to the time-integrated nature of PL spectroscopy, marginal local heating from the laser can be a concern for these types of measurements. As described in Ref. [103], the contribution from laser heating is generally observed as a constant shift in peak energy and can be corrected by adjustments in the value of E_0 used, in principle not influencing the relative stresses observed from the measurement. To ensure that contributions from local heating are minimized, the laser power density was maintained below 0.40 $\mu W/\mu m^2$. This power density is well within the limits for mitigating laser heating, as demonstrated in Ref. [122].

Results for the spatial mapping of GaN PL peak energy across the full wafer are shown in Fig. 7.2 for excitation of the GaN surface directly and through the diamond. An overall red-shift from the "unstressed" E_0 value is seen in both the upper and lower map surfaces, with the corresponding stress values calculated from this shift on the right-hand

axis. It is also evident from the figure that there exists a significant difference in the measured values obtained from the top and bottom surfaces, which we attribute to the substantial gradient in the stresses between the two interfaces of the GaN layer from our prior studies using micro-Raman spectroscopy. Tensile stresses measured on the GaN-side have an average value of 0.90 GPa and standard deviation of 0.16 GPa. Stresses measured from the map of the GaN/D side have an average value of 0.05 GPa and standard deviation of 0.19 GPa. For individual measurements, typical uncertainties are $\pm$0.14 GPa and $\pm$0.09 GPa for the GaN and GaN/D sides, respectively.

Stress mapping for these materials using UV micro-Raman demonstrated a similar gradient in tensile stresses across the growth direction of the GaN layer, as discussed in the previous chapter [84]. Table 7.1 displays a comparison of the average stress values for these two studies, including the values for visible micro-Raman, representing an average measurement of the stresses throughout the GaN layer. The stresses seen in the previous report agree in magnitude to the values observed here for PL and are within the error for each measurement. To further illustrate, Fig. 7.3 presents a summary of the measured stresses across the wafer for both PL and micro-Raman techniques, as well as the simulated stress profile from finite-element (FE) analysis along the vertical cross-section of the GaN layer. The patterned rectangles represent the range of experimental stress values measured, with vertical dimension corresponding to the standard deviation and the horizontal dimension representing the optical penetration depth probed for each measurement. The excitation wavelength for UV micro-Raman (λ_L^{Raman} = 363.8 nm) results in a slightly deeper probe depth for the technique (~100-130 nm) compared to that of the PL excitation (λ_L^{PL} = 291 nm) probe depth of ~65 nm. Taking this into

consideration for the two methods, the results from PL further confirm the gradient, as greater stress relaxation is seen toward the GaN-diamond interface near a higher TD density.

Table 7.1 Comparison of stress mapping techniques for GaN-on-diamond

	GaN-side Stress (GPa)	GaN/D-side Stress (GPa)
UV Micro-Raman [84]	0.86 ± 0.07	0.23 ± 0.06
Visible micro-Raman [84]	0.32 ± 0.10	
UV Photoluminescence	0.90 ± 0.16	0.05 ± 0.19

Some additional uncertainty in this penetration depth does exist for the PL measurement; effects such as PL self-absorption and exciton diffusion can cause an effective penetration depth deeper than expected. Fortunately, for thin films and considerable TD densities this effect is small. In Ref. [170], for 2-μm thick films on sapphire, the exciton diffusion length was measured in a range from 34 – 101 nm, depending on doping concentration. Similarly, in Ref. [171], an exciton diffusion length of ~50 nm was estimated for 2-μm thick n-GaN with appreciable TD densities. The authors attribute TDs acting as a non-radiative recombination centers as the cause for the 50-nm estimate. Considering all of this, the additional effects would only stand to alter the effective penetration depth to a value < 165 nm. Without more detailed information for this wafer regarding doping concentrations and TD densities it is difficult to glean a more accurate estimate.

7.5 Chapter Summary

In summary, UV photoluminescence was used to investigate and map through-layer stresses in GaN HEMT layers on a CVD diamond substrate across a 75-mm wafer. The analysis reveals an unexpected gradient along the growth direction of the GaN layer between the tensile stresses near the AlGaN/GaN interface (~0.90 GPa) and near the GaN/diamond interface (~0.05 GPa). Correlation of this analysis with previous results from UV and visible Micro-Raman attributes the gradient to stress relaxation due to threading dislocations in the regions nearest to the original growth substrate of the MOCVD nitride layers. Agreement between these studies and previous thermal stress simulations imply large difference in the coefficients of thermal expansion for the growth and substrate materials are the cause of the relaxation and suggest the existence of this gradient during the initial stages of MOCVD growth.

7.6 Figures

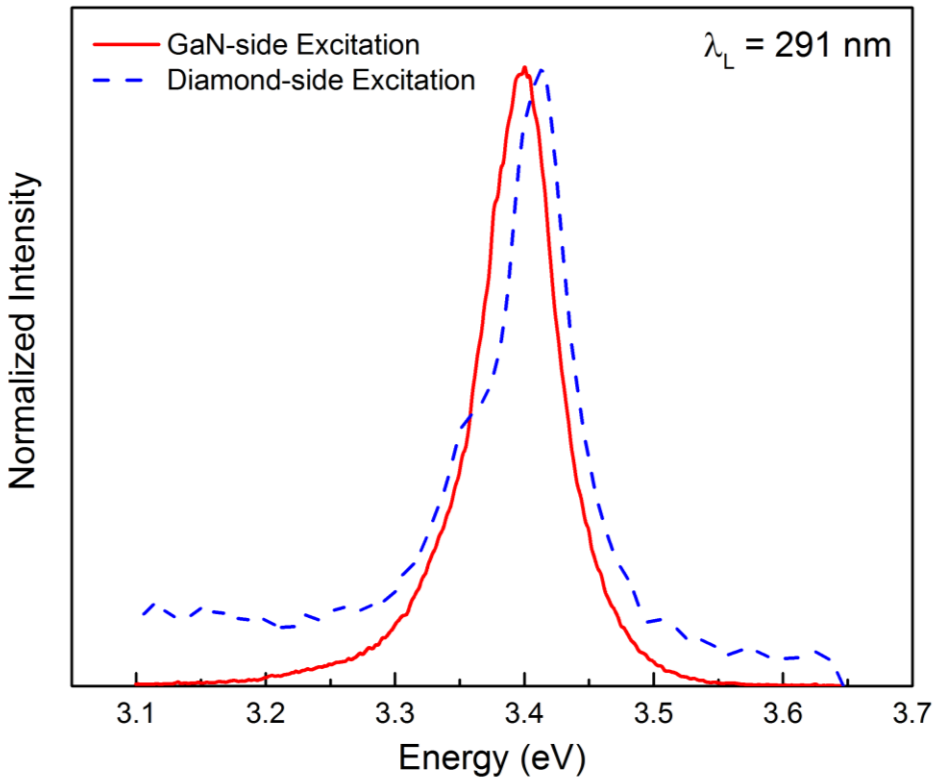

Figure 7.1. PL spectra from GaN-on-diamond wafer. A representative room temperature spectrum shown for excitation from the top GaN surface (solid red line) and the bottom diamond surface (dashed blue line).

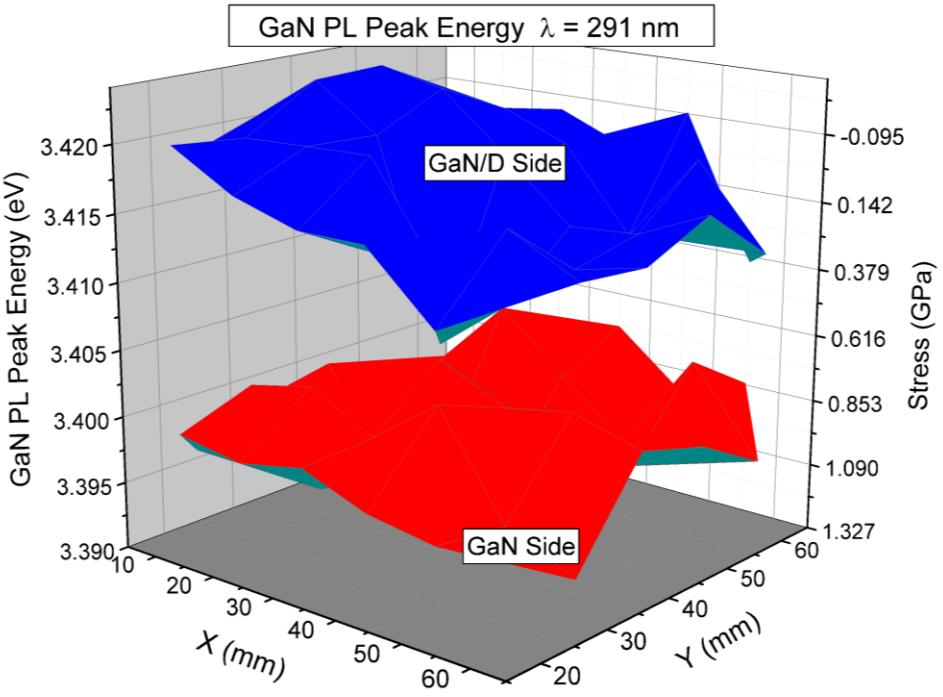

Figure 7.2. Spatial map of PL peak energy across GaN-on-diamond wafer. The upper (blue) and lower (red) surface contours correspond to measurements for GaN/D- and GaN-side excitation, respectively. The right-hand axis displays the calculated tensile stresses for each measurement.

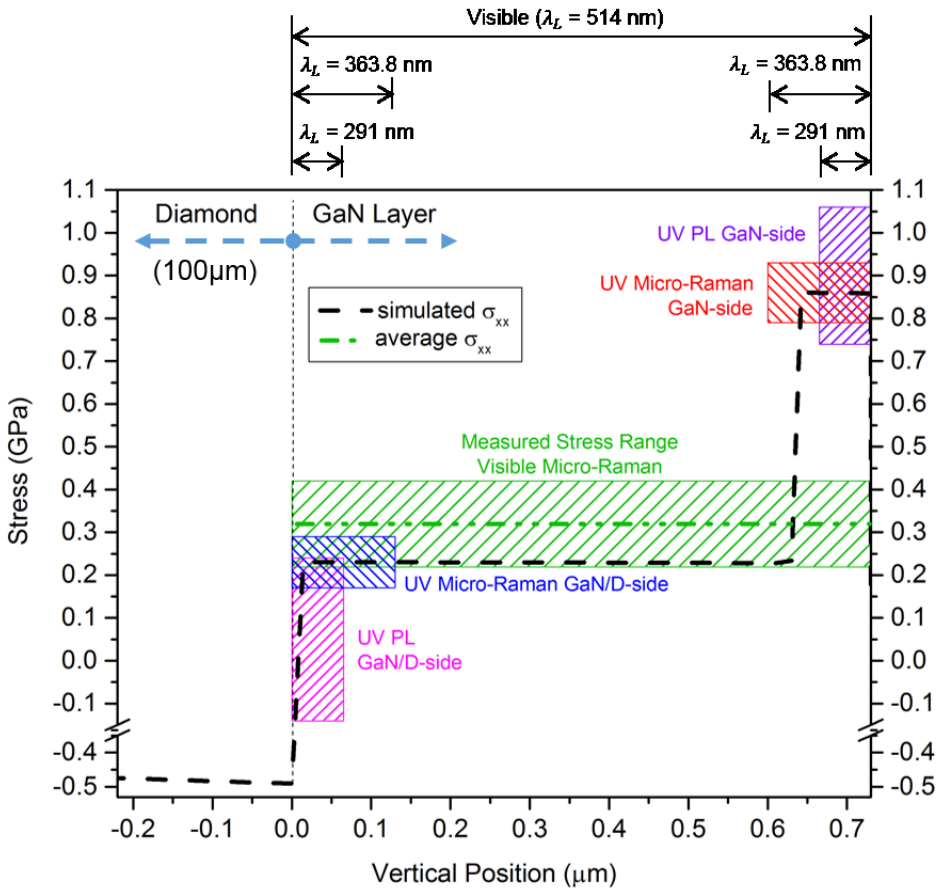

Figure 7.3. Comparison of stress data to finite element results. The stress as a function of vertical position along the material cross-section is shown (Amended from [84]). Simulated stress is shown as a black dashed line. The measured ranges for stress values from micro-Raman and PL for each side of the wafer are represented as patterned rectangles with vertical dimension corresponding to standard deviations from the mean stress value and horizontal dimension the depth optically probed for each measurement. The average stress for the layer, from visible micro-Raman is designated as a dotted-dashed.

8. CONCLUSIONS

The growing market for III-nitride power devices can be attributed to the diverse application spaces addressable by GaN LEDs and AlGaN/GaN transistors. While the success of these devices is apparent in research and industry, their performance potential is limited by thermal management approaches. To overcome this issue, precise characterization is necessary to assess the magnitude of device self-heating. In addition, solutions are needed which provide effective heat extraction near the device layers without substantially adding to the physical footprint of the device and its packaging.

This dissertation work addresses the assessment of device self-heating in high-brightness InGaN/GaN LEDs and AlGaN/GaN HEMTs by monitoring temperature rise in the devices during operation. Additionally, the efficacy of diamond as a heat-spreading substrate was evaluated through the characterization of thermal conductivity in CVD diamond in its applications for thermal management and analyzing the effects of current GaN-on-diamond processing on the material quality of the GaN device material.

8.1 Contributions of this work

The findings presented in this dissertation contribute significantly to the following areas: optical techniques for measuring temperature in LEDs during operation; self-heating metrology in AlGaN/GaN transistors; material quality and thermal transport in CVD diamond thin films for heat-sink applications; and the effects of GaN-on-diamond fabrication on material quality in the device layers. The objective of this collective work is to further the understanding of thermal effects in GaN device materials as well as

provide useful contributions to the development of future thermal management technologies involving CVD diamond in III-nitride applications.

First, techniques for assessing self-heating in high-brightness LEDs were addressed. The junction temperature for an InGaN/GaN MQW high-brightness blue LED was measured using a straightforward electrical technique. The observed blue shift in electroluminescence spectra under typical drive conditions confirms the presence of band-filling and carrier screening in the polar III-nitride device materials in addition to the ever-present self-heating. The consequence of these effects on the peak output energy further validate electrical techniques such as the forward voltage method for accurately measuring junction temperature in III-nitride LEDs and their superiority over spectroscopic methods which rely on heat-induced changes in band gap energy. Finally, it was shown how the forward voltage technique provides the potential for experimentally extracting the thermal relaxation time for the device material.

Next, the characterization of self-heating in GaN transistors during operation using micro-Raman spectroscopy was presented. A depth-dependent profile of temperature rise was established for an AlGaN/GaN HEMT using visible and UV micro-Raman spectroscopy. It was demonstrated how the combination of UV and visible excitation provide insight into the behavior of heat flow for the various layers of the device during operation. Measurements near the 2DEG region of the GaN reveal a temperature rise of ~350 °C for 7.8 W/mm input power, almost twice that seen in the bulk of the GaN from visible Raman. Finite element simulations were used to interpret the temperature depth profile and to establish a value for the TBR present between the AlN nucleation layer and Si substrate.

The integration of CVD diamond into III-nitride device applications was discussed and work involving the characterization of thermal conductivity in CVD diamond thin films was presented with a goal of providing a useful understanding of heat transport in this material for its potential applications in thermal management technologies. Diamond membrane structures on silicon substrates were used to explore the thermal conductivity of thin (~ 1 μm) diamond and the diamond/interface TBR. UV micro-Raman measurements were used to map temperature rises across the diamond membrane to establish an analytical determination of in-plane thermal conductivity. It was discussed how finite element simulations were utilized for fitting the Raman data using a Monte Carlo optimization approach and chi-square minimization technique. Preliminary work was also presented for implementing a new experimental setup involving a line focus across the sample to improve precision in point-to-point data acquisition in the thermal conductivity measurements.

Finally, stresses in GaN-on-diamond wafers were explored through the use of micro-Raman and micro-photoluminescence spectroscopy. Spatial stress mapping across a 75-mm GaN-on-diamond wafer reveal a significant stress gradient between the top and bottom ~100-nm regions of the GaN layer, with ~ 0.9 GPa of tensile stress near the device surface. Stress relaxation due to threading dislocations at the GaN/Diamond interface is discussed as a probable cause for the gradient along the vertical growth direction in the GaN. TEM imaging reveals a larger TD density in the initial growth regime. Results from finite element analysis support this gradient for simulations incorporating stress relaxation in the elastic properties of the GaN at each thermal step in

the fabrication process and demonstrate a stress gradient present from the initial nitride MOCVD growth.

The following articles have been published in association with this dissertation research at Texas State University:

- **B. Logan Hancock**, M. Nazari, J. Anderson, E. L. Piner, F. Faili, S. Oh, D. Francis, D. J. Twitchen, S. Graham, and M. W. Holtz, "Ultraviolet and visible micro-Raman and micro-photoluminescence spectroscopy investigations of stress on a 75-mm GaN-on-diamond wafer," *Phys. status solidi (c),* Under Review 2016

- **B. Logan Hancock**, M. Nazari, J. Anderson, E. Piner, F. Faili, S. Oh, D. Twitchen, S. Graham, and M. Holtz, "Ultraviolet micro-Raman spectroscopy stress mapping of a 75-mm GaN-on-diamond wafer," *Appl. Phys. Lett.*, vol. 108, p. 211901, 2016

- M. Nazari, **B. Logan Hancock**, J. Anderson, A. Savage, E. L. Piner, S. Graham, F. Faili, S. Oh, D. Francis, D. Twitchen, and M. Holtz, "Near-ultraviolet micro-Raman study of diamond grown on GaN," *Appl. Phys. Lett.*, vol. 108, no. 3, 2016

- B. Squires, **B. Logan Hancock**, M. Nazari, J. Anderson, K. D. Hobart, T. I. Feygelson, M. J. Tadjer, B. B. Pate, T. J. Anderson, E. L. Piner, and M. W. Holtz, "Hexagonal boron nitride particles for determining the thermal conductivity of diamond films based on near-ultraviolet micro-Raman mapping," *Appl. Phys. Lett.*, Under Review 2016

- M. Nazari, **B. Logan Hancock**, E. L. Piner, and M. W. Holtz, "Self-heating profile in an AlGaN/GaN heterojunction field-effect transistor studied by ultraviolet and visible micro-Raman spectroscopy," *IEEE Trans. Electron Devices*, vol. 62, no. 5, pp. 1467–1472, 2015

- **B. Logan Hancock**, M. Holtz, "Straightforward electrical measurement of forward-voltage to investigate thermal effects in InGaN/GaN high-brightness light-emitting diodes," *J. Vac. Sci. Technol. B*, vol. 32, no. 6, p. 61209, 2014.

8.2 Suggestions for Future Work

8.2.1 Self-heating in GaN LEDs

For this study, related future efforts should focus on the extraction of thermal relaxation properties for LED materials. This includes careful simulations of self-heating in LED chip materials and packaging, considering a multiple decay model for thermal relaxation. Further developments should include the automation and miniaturization of the experimental setup for fast and cost-effective extraction of LED junction temperature and thermal time-constant measurements in real-time, during device operation. The realization of this setup in a microchip-scale format could warrant substantial commercial merit. Furthermore, evaluating the potential of utilizing the underlying mechanics of this measurement for other electronics, such as field-effect transistors, would prove meaningful in the advancement of indirect temperature characterization methodology

8.2.2 Self-heating in AlGaN/GaN HEMTs

Suggested future work for this study should include applications of this technique for similar devices and heterostructures. It was mentioned how variations in device

design, material composition, layer thickness, and substrate materials all impart effects on the thermal behavior and heat dissipation for the device. It would be interesting to see a more systematic comparison of the temperature effects for a few of these variables in regard to UV/visible measurements during operation. The effects of these material changes on the resulting TBR obtained would also be beneficial. The FE simulations presented in this study also display opportunities for further investigation, namely in exploring complexities in input material properties. For instance, the model used incorporated a temperature dependence in the GaN thermal conductivity due to large temperature changes seen near the 2DEG region during operation. Other layers in the material stack could benefit from similar treatment to improve accuracy, as these layers will begin to see large temperature rises as well during higher power operation.

8.2.3 Thermal Conductivity of CVD Diamond

Future work for this project should include further investigations of diamond thin films on silicon. The thickness of the diamond thin film appears to play a significant role in the values obtained for κ, and further experimentation involving diamond thickness as a consistent variable would be informative. Additionally, the incorporation of stress into the measurements presented here is still not well understood. Preliminary work involving careful simulations of the diamond membrane devices comparing scenarios for uniform heating (as accomplished during $d\omega/dT$ calibration) and heating via current drive in the metalized heater have been initiated but require further consideration. To minimize the role of stress in these measurements, it was mentioned that work involving the incorporation of hexagonal boron nitride (h-BN) micro-particles as on-surface Raman temperature sensors has been recently established and results submitted for publication

[130]. Continual efforts using this h-BN approach in conjunction with investigations of the role stress plays for in-plane measurements of κ would benefit the understanding greatly. It was also discussed how preliminary efforts have begun involving the focus of laser excitation in a line across the membrane, in which Raman signal can be obtained from each point across the membrane in a single measurement. Further efforts to optimize this setup and data collection technique would simplify the diamond membrane measurement in regard to total measurement time, as well as provide greater precision in point-to-point comparisons of the Raman-measured temperature for power-on vs. power-off conditions.

8.2.4 Stress Mapping of GaN-on-Diamond Wafers

Future work for this aspect of the dissertation should include further investigation of GaN HEMT layers integrated with CVD diamond as a heat-spreading substrate. The stress uniformity and stress gradient observed in these efforts are suspected to be present within the material during the initial steps of MOCVD growth of the GaN and nitride transition layers. A study of the observed stresses in these samples for which some, or all, of the transition layers are left intact prior to diamond deposition would be of interest to explore the role these layers play in mitigating stress along the growth direction of the material stack following the integration of CVD diamond. It would also be interesting to investigate the stresses in the GaN layer prior to the diamond deposition, when the underside of the GaN (and/or the transition layers) is exposed. This would provide insight into the existence of a substantial stress gradient prior to the diamond processing step(s).

Additional improvements in the FE model should also be explored. Incorporation of better (and sample-specific) data for TD densities in the GaN would help to improve

the understanding of their role in the stress gradient as substantiated through simulation. Another improvement in the model might be to investigate mechanical steps in the fabrication process; e.g. removal of the initial Si substrate following MOCVD nitride growth and attachment/detachment of the sacrificial handle wafer. It is difficult to model the effects these processing steps have on the overall stress in the thin nitride and diamond layers. There have also been several efforts at investigating the quality of the initial CVD diamond growth regime for these substrates [135]. It would be interesting to look into ways of incorporating this poor diamond quality into the simulations as well. While the effects of this layer on stress may be arguably inconsequential, its role in the investigation of thermal boundary resistance (TBR) at the GaN/diamond interface would be insightful.

REFERENCES

[1] E. F. Schubert, *Light-Emitting Diodes*. Cambridge University Press, 2006.

[2] Z. C. Feng, *III-Nitride Devices and Nanoengineering*. London: Imperial College Press, 2008.

[3] C. Lu, L. Wang, J. Lu, R. Li, L. Liu, D. Li, N. Liu, and L. Li, "Investigation of the electroluminescence spectrum shift of InGaN / GaN multiple quantum well light-emitting diodes under direct and pulsed currents," *J. Appl. Phys.*, vol. 13102, no. 1, p. 13102, 2013.

[4] D. Zhu, D. J. Wallis, and C. J. Humphreys, "Prospects of III-nitride optoelectronics grown on Si," *Reports Prog. Phys.*, vol. 76, no. 10, p. 106501, 2013.

[5] Q. Shan, Q. Dai, S. Chhajed, J. Cho, and E. F. Schubert, "Analysis of thermal properties of GaInN light-emitting diodes and laser diodes," *J. Appl. Phys.*, vol. 108, no. 8, p. 84504, 2010.

[6] J.-C. Wang, C.-H. Fang, Y.-F. Wu, W.-J. Chen, D.-C. Kuo, P.-L. Fan, J.-A. Jiang, and T.-E. Nee, "The effect of junction temperature on the optoelectrical properties of InGaN/GaN multiple quantum well light-emitting diodes," *J. Lumin.*, vol. 132, no. 2, pp. 429–433, 2012.

[7] L. F. Eastman and U. K. Mishra, "The Toughest Transistor Yet," *IEEE Spectrum*, p. 28, 2002.

[8] H. Kambayashi, Y. Satoh, Y. Niiyama, T. Kokawa, M. Iwami, T. Nomura, S. Kato, and T. P. Chow, "Enhancement-mode GaN hybrid MOS-HFETs on Si substrates with Over 70 A operation," *Power Semicond. Devices IC's, 2009. ISPSD 2009. 21st Int. Symp.*, no. 111, pp. 21–24, 2009.

[9] O. Lancry, E. Pichonat, J. Réhault, M. Moreau, R. Aubry, and C. Gaquière, "Development of Time-resolved UV Micro-Raman Spectroscopy to measure temperature in AlGaN/GaN HEMTs," *Solid. State. Electron.*, vol. 54, no. 11, pp. 1434–1437, 2010.

[10] T. P. Chow and R. Tyagi, "Wide bandgap compound semiconductors for superior high-voltage Unipolar Power devices," *IEEE Trans. Electron Devices*, vol. 41, no. 8, p. 1481, 1994.

[11] U. K. Mishra, L. Shen, T. E. Kazior, and Y. F. Wu, "GaN-based RF power devices and amplifiers," *Proc. IEEE*, vol. 96, no. 2, pp. 287–305, 2008.

[12] U. K. Mishra, P. Parikh, and Y. F. Wu, "AlGaN/GaN HEMTs - An overview of device operation and applications," *Proc. IEEE*, vol. 90, no. 6, pp. 1022–1031, 2002.

[13] Y. Wu and A. Agarwal, “5.07 - GaN- and SiC-Based Power Devices A2 - Bhattacharya, Pallab,” R. Fornari and H. B. T.-C. S. S. and T. Kamimura, Eds. Amsterdam: Elsevier, 2011, pp. 299–339.

[14] E. Johnson, “Physical limitations on frequency and power parameters of transistors,” *IRE Int. Conv. Rec.*, vol. 13, pp. 27–34, 1966.

[15] F. a Marino, N. Faralli, D. K. Ferry, S. M. Goodnick, and M. Saraniti, “Figures of merit in high-frequency and high-power GaN HEMTs,” *J. Phys. Conf. Ser.*, vol. 193, p. 12040, 2009.

[16] S. Chhajed, Y. Xi, Y. L. Li, T. Gessmann, and E. F. Schubert, “Influence of junction temperature on chromaticity and color-rendering properties of trichromatic white-light sources based on light-emitting diodes,” *J. Appl. Phys.*, vol. 97, no. 5, pp. 1–8, 2005.

[17] Y. Xi and E. F. Schubert, “Junction-temperature measurement in GaN ultraviolet light-emitting diodes using diode forward voltage method,” *Appl. Phys. Lett.*, vol. 85, no. 12, pp. 2163–2165, 2004.

[18] Y. Xi, J. M. Shah, J. K. Kim, E. F. Schubert, a J. Fischer, M. H. Crawford, K. H. a Bogart, and a a Allerman, “Junction and carrier temperature measurements in deep-ultraviolet light-emitting diodes using three different methods,” *Appl. Phys. Lett.*, vol. 86, pp. 1–3, 2005.

[19] a Wang, M. J. Tadjer, and F. Calle, “Simulation of thermal management in AlGaN/GaN HEMTs with integrated diamond heat spreaders,” *Semicond. Sci. Technol.*, vol. 28, no. 5, p. 55010, 2013.

[20] Y. Xi, T. Gessmann, J. Xi, J. K. Kim, J. M. Shah, E. Fred Schubert, A. J. Fischer, M. H. Crawford, K. H. A. Bogart, and A. A. Allerman, “Junction temperature in ultraviolet light-emitting diodes,” *Japanese J. Appl. Physics, Part 1 Regul. Pap. Short Notes Rev. Pap.*, vol. 44, no. 10, pp. 7260–7266, 2005.

[21] A. Keppens, W. R. Ryckaert, G. Deconinck, and P. Hanselaer, “High power light-emitting diode junction temperature determination from current-voltage characteristics,” *J. Appl. Phys.*, vol. 104, no. 9, 2008.

[22] N. Killat, M. Kuball, T. M. Chou, U. Chowdhury, and J. Jimenez, “Temperature assessment of AlGaN/GaN HEMTs: A comparative study by Raman, electrical and IR thermography,” *IEEE Int. Reliab. Phys. Symp. Proc.*, pp. 528–531, 2010.

[23] M. Kuball, “Raman spectroscopy of GaN, AlGaN and AlN for process and growth monitoring/control,” *Surf. Interface Anal.*, vol. 31, no. 10, pp. 987–999, 2001.

[24] M. Kuball, J. M. Hayes, M. J. Uren, T. Martin, J. C. H. Birbeck, R. S. Balmer, and B. T. Hughes, “Measurement of temperature in active high-power AlGaN/GaN HFETs using Raman spectroscopy,” *IEEE Electron Device Lett.*, vol. 23, no. 1, pp. 7–9, 2002.

[25] M. Kuball, S. Rajasingam, a. Sarua, M. J. Uren, T. Martin, B. T. Hughes, K. P. Hilton, and R. S. Balmer, "Measurement of temperature distribution in multifinger AlGaN/GaN heterostructure field-effect transistors using micro-Raman spectroscopy," *Appl. Phys. Lett.*, vol. 82, no. 1, pp. 124–126, 2003.

[26] A. Sarua, H. Ji, K. P. Hilton, D. J. Wallis, M. J. Uren, T. Martin, and M. Kuball, "Thermal boundary resistance between GaN and substrate in AlGaN/GaN electronic devices," *IEEE Trans. Electron Devices*, vol. 54, no. 12, pp. 3152–3158, 2007.

[27] I. Ahmad, V. Kasisomayajula, M. Holtz, J. M. Berg, S. R. Kurtz, C. P. Tigges, a. a. Allerman, and a. G. Baca, "Self-heating study of an AlGaN/GaN-based heterostructure field-effect transistor using ultraviolet micro-Raman scattering," *Appl. Phys. Lett.*, vol. 86, p. 173503, 2005.

[28] I. Ahmad, V. Kasisomayajula, D. Y. Song, L. Tian, J. M. Berg, and M. Holtz, "Self-heating in a GaN based heterostructure field effect transistor: Ultraviolet and visible Raman measurements and simulations," *J. Appl. Phys.*, vol. 100, no. 11, pp. 1–7, 2006.

[29] D. Francis, F. Faili, D. Babić, F. Ejeckam, A. Nurmikko, and H. Maris, "Formation and characterization of 4-inch GaN-on-diamond substrates," *Diam. Relat. Mater.*, vol. 19, no. 2–3, pp. 229–233, 2010.

[30] F. Ejeckam, D. Babi, F. Faili, D. Francis, F. Lowe, Q. Diduck, C. Khandavalli, D. Twitchen, and B. Bolliger, "3,000+ Hours Continuous Operation of GaN-on-Diamond HEMTs at 350 ◦ C Channel Temperature," *IEEE Semicond. Therm. Meas. Manag. Symp. 2014. 30th Annu.*, 2014.

[31] A. Wang, M. J. Tadjer, T. J. Anderson, R. Baranyai, J. W. Pomeroy, T. I. Feygelson, K. D. Hobart, B. B. Pate, F. Calle, and M. Kuball, "Impact of intrinsic stress in diamond capping layers on the electrical behavior of AlGaN/GaN HEMTs," *IEEE Trans. Electron Devices*, vol. 60, no. 10, pp. 3149–3156, 2013.

[32] G. D. Via, J. G. Felbinger, J. Blevins, K. Chabak, G. Jessen, J. Gillespie, R. Fitch, A. Crespo, K. Sutherlin, B. Poling, S. Tetlak, R. Gilbert, T. Cooper, R. Baranyai, J. W. Pomeroy, M. Kuball, J. J. Maurer, and A. Bar-Cohen, "Wafer-scale GaN HEMT performance enhancement by diamond substrate integration," *Phys. Status Solidi C*, vol. 11, no. 3–4, pp. 871–874, 2014.

[33] D. I. Babic, Q. Diduck, P. Yenigalla, A. Schreiber, D. Francis, F. Faili, F. Ejeckam, J. G. Felbinger, and L. F. Eastman, "GaN-on-diamond field-effect transistors: from wafers to amplifier modules," in *MIPRO, 2010 Proceedings of the 33rd International Convention*, 2010.

[34] "Light Emitting Diodes (LED) Market by Technology (...) and Application (...)," *Allied Market Research*, 2014. [Online]. Available: https://www.alliedmarketresearch.com/LED-light-emitting-diode-market.

[35] M. S. Shur and A. Žukauskas, "Solid-state lighting: Toward superior illumination," *Proc. IEEE*, vol. 93, no. 10, pp. 1691–1703, 2005.

[36] R. N. Hall, G. E. Fenner, J. D. Kingsley, T. J. Soltys, and R. O. Carlson, "Coherent Light Emission From GaAs Junctions," *Phys. Rev. Lett.*, vol. 9, no. 9, pp. 366–368, Nov. 1962.

[37] M. I. Nathan, W. P. Dumke, G. Burns, F. H. Dill, and G. Lasher, "STIMULATED EMISSION OF RADIATION FROM GaAs p-n JUNCTIONS," *Appl. Phys. Lett.*, vol. 1, no. 3, p. 62, 1962.

[38] T. M. Quist, R. H. Rediker, R. J. Keyes, W. E. Krag, B. Lax, A. L. McWhorter, and H. J. Zeigler, "SEMICONDUCTOR MASER OF GaAs," *Appl. Phys. Lett.*, vol. 1, no. 4, 1962.

[39] Y. Li, "Quantum Efficiency Study of GaInN-Based Green Light-Emitting Diodes," Rensselaer Polytechnic Institute, 2010.

[40] H. Rupprecht, J. M. Woodall, and G. D. Pettit, "EFFICIENT VISIBLE ELECTROLUMINESCENCE AT 300°K FROM Ga1- xAlxAs p- n JUNCTIONS GROWN BY LIQUID- PHASE EPITAXY," *Appl. Phys. Lett.*, vol. 11, no. 3, 1967.

[41] M. R. Krames, G. Christenson, D. Collins, L. W. Cook, M. G. Craford, A. Edwards, R. M. Fletcher, N. F. Gardner, W. K. Goetz, W. R. Imler, E. Johnson, R. S. Kern, R. Khare, F. A. Kish, C. Lowery, M. J. Ludowise, R. Mann, M. Maranowski, S. A. Maranowski, P. S. Martin, J. O'Shea, S. L. Rudaz, D. A. Steigerwald, J. Thompson, J. J. Wierer, J. Yu, D. Basile, Y.-L. Chang, G. Hasnain, M. Heuschen, K. P. Killeen, C. P. Kocot, S. Lester, J. N. Miller, G. O. Mueller, R. Mueller-Mach, S. J. Rosner, R. P. Schneider, Jr., T. Takeuchi, and T. S. Tan, "High-Brightness AlGaInN light-emitting diodes," in *Proceedings of SPIE*, 2000, pp. 2–12.

[42] R. Mueller-Mach, G. O. Mueller, M. R. Krames, O. B. Shchekin, P. J. Schmidt, H. Bechtel, C. H. Chen, and O. Steigelmann, "All-nitride monochromatic amber-emitting phosphor-converted light-emitting diodes," *Phys. Status Solidi - Rapid Res. Lett.*, vol. 3, no. 7–8, pp. 215–217, 2009.

[43] S. Nakamura and G. Fasol, *The Blue Laser Diode*. Berlin, Heidelberg: Springer Berlin Heidelberg, 1997.

[44] J. Wu, W. Walukiewicz, K. M. Yu, J. W. Ager, E. E. Haller, H. Lu, W. J. Schaff, Y. Saito, and Y. Nanishi, "Unusual properties of the fundamental band gap of InN," *Appl. Phys. Lett.*, vol. 80, no. 21, 2002.

[45] C. Wetzel and T. Takeuchi, "Optical band gap in Ga 1-x In x N (0.2) on GaN by photoreflection spectroscopy," *Appl. Phys. ...*, vol. 73, no. 14, pp. 1994–1996, 1998.

[46] T. P. Chow and M. Ghezzo, "SiC Power Devices," *MRS Proc.*, vol. 423, 1996.

[47] H. Amano, K. Masahiro, K. Hiramatsu, and I. Akasaki, "P-Type Conduction in Mg-Doped GaN Treated with Low-Energy Electron Beam Irradiation (LEEBI)," *Jpn. J. Appl. Phys.*, vol. 28, no. 12A, p. L2112, 1989.

[48] S. N. and M. S. and T. Mukai, “Highly P-Typed Mg-Doped GaN Films Grown with GaN Buffer Layers,” *Jpn. J. Appl. Phys.*, vol. 30, no. 10A, p. L1708, 1991.

[49] D. Kapolnek, X. H. Wu, B. Heying, S. Keller, B. P. Keller, U. K. Mishra, S. P. DenBaars, and J. S. Speck, “Structural evolution in epitaxial metalorganic chemical vapor deposition grown GaN films on sapphire,” *Appl. Phys. Lett.*, vol. 67, no. 11, 1995.

[50] Y.-F. Wu, M. Moore, a. Saxler, T. Wisleder, and P. Parikh, “40-W/mm Double Field-plated GaN HEMTs,” *2006 64th Device Res. Conf.*, pp. 2005–2006, 2006.

[51] “GaN Power Devices Market by Technology (...), Wafer (...), Device (...), Products, Application & Geography - Global Forecast to 2022,” *MarketsandMarkets*, 2016.

[52] M. Kuball, G. J. Riedel, J. W. Pomeroy, A. Sarua, M. J. Uren, T. Martin, K. P. Hilton, J. O. Maclean, and D. J. Wallis, “Time-Resolved Temperature Measurement of AlGaN / GaN Electronic Devices Using Micro-Raman Spectroscopy,” *IEEE Electron Device Lett.*, vol. 28, no. 2, pp. 86–89, 2007.

[53] B. L. Hancock and M. Holtz, “Straightforward electrical measurement of forward-voltage to investigate thermal effects in InGaN/GaN high-brightness light-emitting diodes,” *J. Vac. Sci. Technol. B*, vol. 32, no. 6, p. 61209, 2014.

[54] S. Todoroki, M. Sawai, and K. Aiki, “Temperature distribution along the striped active region in high-power GaAAlAs visible lasers,” *J. Appl. Phys.*, vol. 58, no. 3, p. 1124, 1985.

[55] N. C. Chen, Y. N. Wang, C. Y. Tseng, and Y. K. Yang, “Determination of junction temperature in AlGaInP⁄GaAs light emitting diodes by self-excited photoluminescence signal,” *Appl. Phys. Lett.*, vol. 89, no. 10, p. 101114, 2006.

[56] Y. P. Varshni, “Temperature dependence of the energy gap in semiconductors,” *Physica*, vol. 34, p. 149, 1967.

[57] D. L. Blackburn, “Temperature measurements of semiconductor devices-a review,” *Semicond. Therm. Meas. Manag. Symp. 2004. Twent. Annu. IEEE*, vol. 20, pp. 70–80, 2004.

[58] M. Nazari, B. L. Hancock, E. L. Piner, and M. W. Holtz, “Self-heating profile in an AlGaN/GaN heterojunction field-effect transistor studied by ultraviolet and visible micro-Raman spectroscopy,” *IEEE Trans. Electron Devices*, vol. 62, no. 5, pp. 1467–1472, 2015.

[59] S. Nakamura, S. Pearton, and G. Fasol, *The Blue Laser Diode*. Berlin, Heidelberg: Springer Berlin Heidelberg, 2000.

[60] T. Kozawa, T. Kachi, H. Kano, H. Nagase, N. Koide, and K. Manabe, “Thermal stress in GaN epitaxial layers grown on sapphire substrates,” *J. Appl. Phys.*, vol. 77, no. 9, p. 4389, 1995.

[61] M. Bhatnagar and B. J. Baliga, “Comparison of 6H-SiC, 3C-SiC, and Si for power devices,” *IEEE Transactions on Electron Devices*, vol. 40, no. 3. pp. 645–655, 1993.

[62] M. Leszczynski, H. Teisseyre, T. Suski, I. Grzegory, M. Bockowski, J. Jun, S. Porowski, K. Pakula, J. M. Baranowski, C. T. Foxon, and T. S. Cheng, “Lattice parameters of gallium nitride,” *Appl. Phys. Lett.*, vol. 69, no. 1, 1996.

[63] V. Siklitsky, “Material Properties,” *New Semiconductor Materials (NSM) Archive*. [Online]. Available: http://www.ioffe.ru/SVA/NSM/Semicond/.

[64] K. Malcolm, “Characterization of the thermal properties of chemical vapor deposition grown diamond films for electronics cooling,” Georgia Institute of Technology, 2016.

[65] F. N. Faili, C. Engdahl, and E. Francis, “GaN-on-Diamond substrates for HEMT applications,” *Diam. Tool. J.*, vol. 1, no. 9, pp. 52–55, 2009.

[66] J. Anaya, S. Rossi, M. Alomari, E. Kohn, L. Tóth, B. Pécz, K. D. Hobart, T. J. Anderson, T. I. Feygelson, B. B. Pate, and M. Kuball, “Control of the in-plane thermal conductivity of ultra-thin nanocrystalline diamond films through the grain and grain boundary properties,” *Acta Mater.*, vol. 103, pp. 141–152, 2016.

[67] M. A. Angadi, T. Watanabe, A. Bodapati, X. Xiao, O. Auciello, J. A. Carlisle, J. A. Eastman, P. Keblinski, P. K. Schelling, and S. R. Phillpot, “Thermal transport and grain boundary conductance in ultrananocrystalline diamond thin films,” *J. Appl. Phys.*, vol. 99, no. 11, 2006.

[68] K. Filippov and A. A. Balandin, “The effect of the thermal boundary resistance on self-heating of AlGaN/GaN HFETs,” *MRS Internet J. Nitride Semicond. Res.*, vol. 8, p. e4, 2003.

[69] Y. Won, J. Cho, D. Agonafer, M. Asheghi, and K. E. Goodson, “Fundamental Cooling Limits for High Power Density Gallium Nitride Electronics,” *IEEE Trans. Components, Packag. Manuf. Technol.*, vol. 5, no. 6, pp. 737–744, 2015.

[70] J. Cho, Y. Li, W. E. Hoke, D. H. Altman, M. Asheghi, and K. E. Goodson, “Phonon scattering in strained transition layers for GaN heteroepitaxy,” *Phys. Rev. B - Condens. Matter Mater. Phys.*, vol. 89, no. 11, pp. 1–11, 2014.

[71] J. Cho, E. Bozorg-Grayeli, D. H. Altman, M. Asheghi, and K. E. Goodson, “Low thermal resistances at GaN-SiC interfaces for HEMT technology,” *IEEE Electron Device Lett.*, vol. 33, no. 3, pp. 378–380, 2012.

[72] J. Kuzmík, S. Bychikhin, D. Pogany, C. Gaquière, E. Pichonat, and E. Morvan, “Investigation of the thermal boundary resistance at the III-Nitride/substrate interface using optical methods,” *J. Appl. Phys.*, vol. 101, no. 2007, p. 54508, 2007.

[73] J. W. Pomeroy, R. B. Simon, H. Sun, D. Francis, F. Faili, D. J. Twitchen, and M. Kuball, "Contactless Thermal Boundary Resistance Measurement of GaN-on-Diamond Wafers," *IEEE Electron Device Lett.*, vol. 35, no. 10, pp. 1007–1009, 2014.

[74] J. W. Pomeroy, M. Bernardoni, D. C. Dumka, D. M. Fanning, and M. Kuball, "Low thermal resistance GaN-on-diamond transistors characterized by three-dimensional Raman thermography mapping," *Appl. Phys. Lett.*, vol. 104, no. 8, 2014.

[75] J. Cho, Z. Li, E. Bozorg-Grayeli, T. Kodama, D. Francis, F. Ejeckam, F. Faili, M. Asheghi, and K. E. Goodson, "Improved thermal interfaces of GaN-Diamond composite substrates for HEMT applications," *IEEE Trans. Components, Packag. Manuf. Technol.*, vol. 3, no. 1, pp. 79–85, 2013.

[76] H. Sun, R. B. Simon, J. W. Pomeroy, D. Francis, F. Faili, D. J. Twitchen, and M. Kuball, "Reducing GaN-on-diamond interfacial thermal resistance for high power transistor applications," *Appl. Phys. Lett.*, vol. 106, no. 11, 2015.

[77] J. E. Graebner, M. E. Reiss, L. Seibles, T. M. Hartnett, R. P. Miller, and C. J. Robinson, "Phonon scattering in chemical-vapor-deposited diamond," *Phys. Rev. B*, vol. 50, no. 6, pp. 3702–3713, 1994.

[78] G. W. G. van Dreumel, P. T. Tinnemans, A. A. J. van den Heuvel, T. Bohnen, J. G. Buijnsters, J. J. ter Meulen, W. J. P. van Enckevort, P. R. Hageman, and E. Vlieg, "Realising epitaxial growth of GaN on (001) diamond," *J. Appl. Phys.*, vol. 110, no. 1, 2011.

[79] J. Pomeroy, M. Bernardoni, a. Sarua, a. Manoi, D. C. Dumka, D. M. Fanning, and M. Kuball, "Achieving the best thermal performance for GaN-on-diamond," *Tech. Dig. - IEEE Compd. Semicond. Integr. Circuit Symp. CSIC*, pp. 1–4, 2013.

[80] K. D. Chabak, J. K. Gillespie, V. Miller, A. Crespo, J. Roussos, M. Trejo, D. E. Walker, G. D. Via, G. H. Jessen, J. Wasserbauer, F. Faili, D. I. Babic, D. Francis, and F. Ejeckam, "Full-Wafer Characterization of AlGaN / GaN HEMTs," *Ieee Electron Device Lett. Vol. 31, No. 2, Febr. 2010*, vol. 31, no. 2, pp. 99–101, 2010.

[81] F. Ejeckam, D. Francis, F. Faili, D. Twitchen, B. Bolliger, D. Babic, and J. Felbinger, "S2-T1: GaN-on-diamond: A brief history," *2014 Lester Eastman Conf. High Perform. Devices*, no. July 2015, pp. 1–5, 2014.

[82] H. Sun, J. W. Pomeroy, R. B. Simon, D. Francis, F. Faili, D. J. Twitchen, and M. Kuball, "Rapid Characterization of GaN-on-diamond Interfacial Thermal Resistance Using Contactless Transient Thermoreflectance," *CS MANTECH 2015*, pp. 151–154, 2015.

[83] H. Sun, J. W. Pomeroy, R. B. Simon, D. Francis, F. Faili, D. J. Twitchen, and M. Kuball, "Temperature-Dependent Thermal Resistance of GaN-on-Diamond HEMT Wafers," *IEEE Electron Device Lett.*, vol. 37, no. 5, pp. 621–624, 2016.

[84] B. L. Hancock, M. Nazari, J. Anderson, E. Piner, F. Faili, S. Oh, D. Twitchen, S. Graham, and M. Holtz, "Ultraviolet micro-Raman spectroscopy stress mapping of a 75-mm GaN-on-diamond wafer," *Appl. Phys. Lett.*, vol. 108, p. 211901, 2016.

[85] S. Nakamura, "A bright future for blue/green LEDs," *IEEE Circuits Devices Mag.*, vol. 11, no. 3, pp. 19–23, 1995.

[86] X. Sun, D. Li, H. Song, Y. Chen, H. Jiang, G. Miao, and Z. Li, "Short-wavelength light beam in situ monitoring growth of InGaN/GaN green LEDs by MOCVD.," *Nanoscale Res. Lett.*, vol. 7, no. 1, p. 282, 2012.

[87] D. I. Ellis and R. Goodacre, "Metabolic fingerprinting in disease diagnosis: biomedical applications of infrared and Raman spectroscopy," *Analyst*, vol. 131, no. 8, pp. 875–885, 2006.

[88] G. Mogilevsky, L. Borland, M. Brickhouse, and A. W. Fountain III, "Raman Spectroscopy for Homeland Security Applications," *Int. J. Spectrosc.*, vol. 2012, pp. 1–12, 2012.

[89] J. R. Ferraro, K. Nakamoto, and C. W. Brown, *Introductory Raman Spectroscopy*. 2003.

[90] C. Hodges, J. Pomeroy, and M. Kuball, "Probing temperature gradients within the GaN buffer layer of AlGaN/GaN high electron mobility transistors with Raman thermography," *J. Appl. Phys.*, vol. 115, pp. 4–9, 2014.

[91] P. L. Stiles, J. A. Dieringer, N. C. Shah, and R. P. Van Duyne, "Surface-Enhanced Raman Spectroscopy," *Annu. Rev. Anal. Chem.*, vol. 1, no. 1, pp. 601–626, Jul. 2008.

[92] V. Deckert, "Tip-Enhanced Raman Spectroscopy," *J. Raman Spectrosc.*, vol. 40, no. 10, pp. 1336–1337, Oct. 2009.

[93] C. Kittel, *Introduction to Solid State Physics, 8th Ed.* Wiley, 2005.

[94] C. V. Raman and K. S. Krishnan, "A New Type of Secondary Radiation," *Nature*, vol. 121, no. 3048, pp. 501–502, Mar. 1928.

[95] D. Altman, M. Tyhach, J. McClymonds, S. Kim, S. Graham, J. Cho, K. Goodson, D. Francis, F. Faili, F. Ejeckam, and S. Bernstein, "Analysis and characterization of thermal transport in GaN HEMTs on Diamond substrates," *Fourteenth Intersoc. Conf. Therm. Thermomechanical Phenom. Electron. Syst.*, pp. 1199–1205, 2014.

[96] D. Y. Song, M. Basavaraj, S. A. Nikishin, M. Holtz, V. Soukhoveev, A. Usikov, and V. Dmitriev, "The influence of phonons on the optical properties of GaN," *J. Appl. Phys.*, vol. 100, no. 11, pp. 1–6, 2006.

[97] S. Choi, E. Heller, D. Dorsey, R. Vetury, and S. Graham, "Thermometry of AlGaN/GaN HEMTs Using Multispectral Raman Features," *IEEE Trans. Electron Devices*, vol. 60, no. 6, pp. 1898–1904, 2013.

[98] A. Link, K. Bitzer, W. Limmer, R. Sauer, C. Kirchner, V. Schwegler, M. Kamp, D. G. Ebling, and K. W. Benz, "Temperature dependence of the E-2 and A(1)(LO) phonons in GaN and AlN," *J. Appl. Phys.*, vol. 86, no. 11, pp. 6256–6260, 1999.

[99] S. C. Hsu, B. J. Pong, W. H. Li, T. E. Beechem, S. Graham, and C. Y. Liu, "Stress relaxation in GaN by transfer bonding on Si substrates," *Appl. Phys. Lett.*, vol. 91, no. 25, pp. 1–4, 2007.

[100] M. Holtz, M. Seon, T. Prokofyeva, H. Temkin, R. Singh, F. P. Dabkowski, and T. D. Moustakas, "Micro-Raman imaging of GaN hexagonal island structures," *Appl. Phys. Lett.*, vol. 75, no. 12, pp. 1757–1759, 1999.

[101] I. Ahmad, M. Holtz, N. N. Faleev, and H. Temkin, "Dependence of the stress-temperature coefficient on dislocation density in epitaxial GaN grown on alpha-Al2O3 and 6H-SiC substrates," *J. Appl. Phys.*, vol. 95, no. 4, pp. 1692–1697, 2004.

[102] C. Kisielowski, J. Krüger, S. Ruvimov, T. Suski, J. Ager, E. Jones, Z. Liliental-Weber, M. Rubin, E. Weber, M. Bremser, and R. Davis, "Strain-related phenomena in GaN thin films," *Phys. Rev. B*, vol. 54, no. 24, pp. 17745–17753, 1996.

[103] S. Choi, E. Heller, D. Dorsey, R. Vetury, and S. Graham, "Analysis of the residual stress distribution in AlGaN/GaN high electron mobility transistors," *J. Appl. Phys.*, vol. 113, no. 9, p. 93510, 2013.

[104] T. Batten, J. W. Pomeroy, M. J. Uren, T. Martin, and M. Kuball, "Simultaneous measurement of temperature and thermal stress in AlGaN/GaN high electron mobility transistors using Raman scattering spectroscopy," *J. Appl. Phys.*, vol. 106, no. 9, p. 94509, 2009.

[105] Q. Yan, P. Rinke, A. Janotti, M. Scheffler, and C. G. Van De Walle, "Effects of strain on the band structure of group-III nitrides," *Phys. Rev. B - Condens. Matter Mater. Phys.*, vol. 90, no. 12, pp. 1–11, 2014.

[106] J. a. Ferrer-Pérez, B. Claflin, D. Jena, M. Sen, R. Vetury, and D. Dorsey, "Photoluminescence-based electron and lattice temperature measurements in GaN-based HEMTs," *J. Electron. Mater.*, vol. 43, no. 2, pp. 341–347, 2014.

[107] D. G. Zhao, S. J. Xu, M. H. Xie, S. Y. Tong, and H. Yang, "Stress and its effect on optical properties of GaN epilayers grown on Si(111), 6H-SiC(0001), and c-plane sapphire," *Appl. Phys. Lett.*, vol. 83, no. 4, pp. 677–679, 2003.

[108] W. Rieger, T. Metzger, H. Angerer, R. Dimitrov, O. Ambacher, and M. Stutzmann, "Influence of substrate-induced biaxial compressive stress on the optical properties of thin GaN films," *Appl. Phys. Lett.*, vol. 970, no. 1996, p. 970, 1995.

[109] V. Y. Davydov, N. S. Averkiev, I. N. Goncharuk, D. K. Nelson, I. P. Nikitina, a. S. Polkovnikov, a. N. Smirnov, M. a. Jacobson, and O. K. Semchinova, "Raman and photoluminescence studies of biaxial strain in GaN epitaxial layers grown on 6H-SiC," *J. Appl. Phys.*, vol. 82, no. 10, pp. 5097–5102, 1997.

[110] J. Pankove, *Optical Processes in Semiconductors*. Dover Publications, 1971.

[111] E. Madenci and I. Guven, *The Finite Element Method and Applications in Engineering Using ANSYS®*. Boston, MA: Springer US, 2015.

[112] J. Taylor, *an Introduction to Error Analysis*, 2nd ed. University Science Books, 1997.

[113] R. Pässler, "Temperature dependence of fundamental band gaps in group IV, III-V, and II-VI materials via a two-oscillator model," *J. Appl. Phys.*, vol. 89, no. 11 I, pp. 6235–6240, 2001.

[114] M. E. Holtz, I. Gherasoiu, V. Kuryatkov, S. A. Nikishin, A. A. Bernussi, and M. W. Holtz, "Influence of phonons on the temperature dependence of photoluminescence in InN with low carrier concentration," *J. Appl. Phys.*, vol. 105, no. 6, 2009.

[115] P. G. Eliseev, P. Perlin, J. Lee, and M. Osin, """ Blue "' temperature-induced shift and band-tail emission in InGaN-based light sources," *Appl. Phys. Lett.*, vol. 71, pp. 569–571, 1997.

[116] K. L. Teo, J. S. Colton, P. Y. Yu, E. R. Weber, M. F. Li, W. Liu, K. Uchida, H. Tokunaga, N. Akutsu, and K. Matsumoto, "An analysis of temperature dependent photoluminescence line shapes in InGaN," *Appl. Phys. Lett.*, vol. 73, no. 12, pp. 1697–1699, 1998.

[117] S. Nakagawa, H. Tsujimura, K. Okamoto, M. Kubota, and H. Ohta, "Temperature dependence of polarized electroluminescence from nonpolar m-plane InGaN-based light emitting diodes," *Appl. Phys. Lett.*, vol. 91, no. 17, p. 171110, 2007.

[118] T. Mukai, D. Morita, and S. Nakamura, "High-power UV InGaN/AlGaN double-heterostructure LEDs," *J. Cryst. Growth*, vol. 189–190, pp. 778–781, 1998.

[119] T. Mukai, H. Narimatsu, and S. Nakamura, "Amber InGaN-Based Light-Emitting Diodes Operable at High Ambient Temperatures," *Jpn. J. Appl. Phys.*, vol. 37, no. 5A, p. L479, 1998.

[120] P. Vitta and A. Žukauskas, "Thermal characterization of light-emitting diodes in the frequency domain," *Phys. status solidi*, vol. 6, no. S2, pp. S877–S880, Jun. 2009.

[121] J. W. Johnson, E. L. Piner, A. Vescan, R. Therrien, P. Rajagopal, J. C. Roberts, J. D. Brown, S. Singhal, and K. J. Linthicum, "12 W/mm AlGaN-GaN HFETs on silicon substrates," *IEEE Electron Device Lett.*, vol. 25, no. 7, pp. 459–461, 2004.

[122] T. Batten, A. Manoi, M. J. Uren, T. Martin, and M. Kuball, “Temperature analysis of AlGaN/GaN based devices using photoluminescence spectroscopy: Challenges and comparison to Raman thermography,” *J. Appl. Phys.*, vol. 107, no. 7, p. 74502, 2010.

[123] J. Wagner, H. Obloh, M. Kunzer, M. Maier, K. Köhler, and B. Johs, “Dielectric function spectra of GaN, AlGaN, and GaN/AlGaN heterostructures,” *J. Appl. Phys.*, vol. 89, no. 5, pp. 2779–2785, 2001.

[124] D. E. Aspnes and A. A. Studna, “Dielectric functions and optical parameters of Si, Ge, GaP, GaAs, GaSb, InP, InAs, and InSb from 1.5 to 6.0 eV,” *Phys. Rev. B*, vol. 27, no. 2, pp. 985–1009, Jan. 1983.

[125] T. Hart, R. Aggarwal, and B. Lax, “Temperature Dependence of Raman Scattering in Silicon,” *Phys. Rev. B*, vol. 1, no. 2, pp. 638–642, 1970.

[126] T. Beechem, A. Christensen, D. S. Green, and S. Graham, “Assessment of stress contributions in GaN high electron mobility transistors of differing substrates using Raman spectroscopy,” *J. Appl. Phys.*, vol. 106, no. 11, p. 114509, 2009.

[127] C. Hodges, J. Anaya Calvo, S. Stoffels, D. Marcon, and M. Kuball, “AlGaN/GaN field effect transistors for power electronics—Effect of finite GaN layer thickness on thermal characteristics,” *Appl. Phys. Lett.*, vol. 103, no. 20, 2013.

[128] W. Liu and A. a. Balandin, “Temperature dependence of thermal conductivity of Al[sub x]Ga[sub 1−x]N thin films measured by the differential 3ω technique,” *Appl. Phys. Lett.*, vol. 85, no. 22, p. 5230, 2004.

[129] W. Liu and A. A. Balandin, “Thermal conduction in AlxGa1-xN alloys and thin films,” *J. Appl. Phys.*, vol. 97, no. 7, 2005.

[130] A. Jeżowski, B. A. Danilchenko, M. Boćkowski, I. Grzegory, S. Krukowski, T. Suski, and T. Paszkiewicz, “Thermal conductivity of GaN crystals in 4.2–300 K range,” *Solid State Commun.*, vol. 128, no. 2–3, pp. 69–73, Oct. 2003.

[131] E. T. Swartz and R. O. Pohl, “Thermal boundary resistance,” *Rev. Mod. Phys.*, vol. 61, no. 3, pp. 605–668, 1989.

[132] A. Manoi, J. W. Pomeroy, N. Killat, and M. Kuball, “Benchmarking of Thermal Boundary Resistance in AlGaN/GaN HEMTs on SiC Substrates: Implications of the Nucleation Layer Microstructure,” *IEEE Electron Device Letters*, vol. 31, no. 12. pp. 1395–1397, 2010.

[133] G. J. Riedel, J. W. Pomeroy, K. P. Hilton, J. O. Maclean, D. J. Wallis, M. J. Uren, T. Martin, U. Forsberg, A. Lundskog, A. Kakanakova-Georgieva, G. Pozina, E. Janzen, R. Lossy, R. Pazirandeh, F. Brunner, J. Wurfl, and M. Kuball, “Reducing Thermal Resistance of AlGaN/GaN Electronic Devices Using Novel Nucleation Layers,” *IEEE Electron Device Letters*, vol. 30, no. 2. pp. 103–106, 2009.

[134] W. L. Liu, M. Shamsa, I. Calizo, a. a. Balandin, V. Ralchenko, a. Popovich, and a. Saveliev, "Thermal conduction in nanocrystalline diamond films: Effects of the grain boundary scattering and nitrogen doping," *Appl. Phys. Lett.*, vol. 89, no. 17, p. 171915, 2006.

[135] M. Nazari, B. L. Hancock, J. Anderson, A. Savage, E. L. Piner, S. Graham, F. Faili, S. Oh, D. Francis, D. Twitchen, and M. Holtz, "Near-ultraviolet micro-Raman study of diamond grown on GaN," *Appl. Phys. Lett.*, vol. 108, no. 3, 2016.

[136] N. Khosravian, M. K. Samani, G. C. Loh, G. C. K. Chen, D. Baillargeat, and B. K. Tay, "Molecular dynamic simulation of diamond/silicon interfacial thermal conductance," *J. Appl. Phys.*, vol. 113, no. 2, 2013.

[137] J. Anaya, S. Rossi, M. Alomari, E. Kohn, L. Tóth, B. Pécz, and M. Kuball, "Thermal conductivity of ultrathin nano-crystalline diamond films determined by Raman thermography assisted by silicon nanowires," *Appl. Phys. Lett.*, vol. 106, no. 22, p. 223101, 2015.

[138] B. Squires, B. L. Hancock, M. Nazari, J. Anderson, K. D. Hobart, T. I. Feygelson, M. J. Tadjer, B. B. Pate, T. J. Anderson, E. L. Piner, and M. W. Holtz, "Hexagonal boron nitride particles for determining the thermal conductivity of diamond films based on near-ultraviolet micro-Raman mapping," 2016.

[139] L. Bergman and R. J. Nemanich, "Raman and photoluminescence analysis of stress state and impurity distribution in diamond thin films," *J. Appl. Phys.*, vol. 78, no. 11, pp. 6709–6719, 1995.

[140] W. H. Press, S. A. Teulkolsky, W. T. Vetterling, and B. P. Flannery, *Numerical Recipes*. Cambridge University Press, 2007.

[141] K. D. Chabak, J. K. Gillespie, V. Miller, A. Crespo, J. Roussos, M. Trejo, D. E. Walker, G. D. Via, G. H. Jessen, J. Wasserbauer, F. Faili, D. I. Babić, D. Francis, and F. Ejeckam, "Full-wafer characterization of AlGaN/GaN HEMTs on free-standing CVD diamond substrates," *IEEE Electron Device Lett.*, vol. 31, no. 2, pp. 99–101, 2010.

[142] J. G. Felbinger, M. V. S. Chandra, Y. Sun, L. F. Eastman, J. Wasserbauer, F. Faili, D. Babic, D. Francis, and F. Ejeckam, "Comparison of GaN HEMTs on diamond and SiC substrates," *IEEE Electron Device Lett.*, vol. 28, no. 11, pp. 948–950, 2007.

[143] R. H. Zhu, J. Y. Miao, J. L. Liu, L. X. Chen, J. C. Guo, C. Y. Hua, T. Ding, H. K. Lian, and C. M. Li, "High temperature thermal conductivity of free-standing diamond films prepared by DC arc plasma jet CVD," *Diam. Relat. Mater.*, vol. 50, pp. 55–59, 2014.

[144] D. Francis, J. Wasserbauer, and F. Faili, "GaN-HEMT epilayers on diamond substrates: recent progress," *Proc. CS MANTECH, Austin, TX*, no. 650, p. 133, 2007.

[145] S. Tripathy, S. J. Chua, P. Chen, and Z. L. Miao, "Micro-Raman investigation of strain in GaN and Al xGa 1-xN/GaN heterostructures grown on Si(111)," *J. Appl. Phys.*, vol. 92, no. 7, pp. 3503–3510, 2002.

[146] M. Chu, A. D. Koehler, A. Gupta, T. Nishida, and S. E. Thompson, "Simulation of AlGaN/GaN high-electron-mobility transistor gauge factor based on two-dimensional electron gas density and electron mobility," *J. Appl. Phys.*, vol. 108, no. 10, p. 104502, 2010.

[147] B. S. Kang, S. Kim, J. Kim, F. Ren, K. Baik, S. J. Pearton, B. P. Gila, C. R. Abernathy, C. C. Pan, G. T. Chen, J. I. Chyi, V. Chandrasekaran, M. Sheplak, T. Nishida, and S. N. G. Chu, "Effect of external strain on the conductivity of AlGaN/GaN high-electron-mobility transistors," *Appl. Phys. Lett.*, vol. 83, no. 23, pp. 4845–4847, 2003.

[148] B. S. Kang, S. Kim, F. Ren, J. W. Johnson, R. J. Therrien, P. Rajagopal, J. C. Roberts, E. L. Piner, K. J. Linthicum, S. N. G. Chu, K. Baik, B. P. Gila, C. R. Abernathy, and S. J. Pearton, "Pressure-induced changes in the conductivity of AlGaN/GaN high-electron mobility-transistor membranes," *Appl. Phys. Lett.*, vol. 85, no. 14, pp. 2962–2964, 2004.

[149] A. D. Williams and T. D. Moustakas, "Formation of large-area freestanding gallium nitride substrates by natural stress-induced separation of GaN and sapphire," *J. Cryst. Growth*, vol. 300, pp. 37–41, 2007.

[150] H. Windischmann and G. F. Epps, "Intrinsic stress in diamond films prepared by microwave plasma CVD," *J. Appl. Phys.*, vol. 69, no. 4, pp. 2231–2237, 1991.

[151] C. H. Xu, C. Z. Wang, C. T. Chan, and K. M. Ho, "Theory of the thermal expansion of Si and diamond," *Phys. Rev. B*, vol. 43, no. 6, pp. 5024–5027, 1991.

[152] M. J. Edwards, C. R. Bowen, D. W. E. Allsopp, and A. C. E. Dent, "Modelling wafer bow in silicon–polycrystalline CVD diamond substrates for GaN-based devices," *J. Phys. D. Appl. Phys.*, vol. 43, no. 38, p. 385502, 2010.

[153] C. Roder, S. Einfeldt, S. Figge, and D. Hommel, "Temperature dependence of the thermal expansion of GaN," *Phys. Rev. B*, vol. 72, no. 8, p. 85218, 2005.

[154] H. Watanabe, N. Yamada, and M. Okaji, "Linear thermal expansion coefficient of silicon from 293 to 1000 K," *Int. J. Thermophys.*, vol. 25, no. 1, pp. 221–236, 2004.

[155] G. Nootz, A. Schulte, L. Chernyak, A. Osinsky, J. Jasinski, M. Benamara, and Z. Liliental-Weber, "Correlations between spatially resolved Raman shifts and dislocation density in GaN films," *Appl. Phys. Lett.*, vol. 80, no. 8, pp. 1355–1357, 2002.

[156] N. Faleev, H. Temkin, I. Ahmad, M. Holtz, and Y. Melnik, "Depth dependence of defect density and stress in GaN grown on SiC," *J. Appl. Phys.*, vol. 98, no. 12, p. 123508, 2005.

[157] H. L. Duan, J. Wang, Z. P. Huang, and B. L. Karihaloo, "Size-dependent effective elastic constants of solids containing nano-inhomogeneities with interface stress," *J. Mech. Phys. Solids*, vol. 53, pp. 1574–1596, 2005.

[158] J. C. Roberts, J. W. Cook, P. Rajagopal, E. L. Piner, and K. J. Linthicum, "AlGaN transition layers on Si (111) substrates - observations of microstructure and impact on material quality," *Mater. Res. Soc. Symp. Proc.*, vol. 1068, pp. 147–152, 2008.

[159] A. Vescan, J. D. Brown, J. W. Johnson, R. Therrien, T. Gehrke, P. Rajagopal, J. C. Roberts, S. Singhal, W. Nagy, R. Borges, E. L. Piner, and K. Linthicum, "AlGaN/GaN HFETs on 100 mm silicon substrates for commercial wireless applications," *Phys. Status Solidi C*, vol. 0, pp. 52–56, 2002.

[160] H. Harima, "Properties of GaN and related compounds studied by means of Raman scattering," *J. Phys. Condens. Matter*, vol. 14, no. 38, pp. R967–R993, 2002.

[161] D. Y. Song, A. Chandolu, N. Stojanovic, S. a. Nikishin, and M. Holtz, "Effect of impurity incorporation on emission wavelength in cathodoluminescence spectrum image study of GaN pyramids grown by selective area epitaxy," *J. Appl. Phys.*, vol. 104, no. 6, p. 64309, 2008.

[162] G. H. Jessen, J. K. Gillespie, G. D. Via, A. Crespo, D. Langley, J. Wasserbauer, F. Faili, D. Francis, D. Babic, F. Ejeckam, S. Guo, and I. Eliashevich, "AlGaN/GaN HEMT on diamond technology demonstration," *Tech. Dig. - IEEE Compd. Semicond. Integr. Circuit Symp. CSIC*, no. December, pp. 271–274, 2006.

[163] D. C. Dumka, D. Francis, T. M. Chou, F. Ejeckam, and F. Faili, "AlGaN/GaN HEMTs on diamond substrate with over 7 W/mm output power density at 10 GHz," *Electron. Lett.*, vol. 49, no. 20, pp. 1298–1299, 2013.

[164] A. V. Sukhadolau, E. V. Ivakin, V. G. Ralchenko, A. V. Khomich, A. V. Vlasov, and A. F. Popovich, "Thermal conductivity of CVD diamond at elevated temperatures," *Diam. Relat. Mater.*, vol. 14, no. 3–7, pp. 589–593, 2005.

[165] D. J. Twitchen, C. S. J. Pickles, S. E. Coe, R. S. Sussmann, and C. E. Hall, "Thermal conductivity measurements on CVD diamond," *Diam. Relat. Mater.*, vol. 10, no. 3–7, pp. 731–735, 2001.

[166] F. C. Wang, C. L. Cheng, Y. F. Chen, C. F. Huang, and C. C. Yang, "Residual thermal strain in thick GaN epifilms revealed by cross-sectional Raman scattering and cathodoluminescence spectra," *Semicond. Sci. Technol.* , vol. 22, no. 8, pp. 896–899, 2007.

[167] B. L. Hancock, M. Nazari, J. Anderson, E. L. Piner, F. Faili, S. Oh, D. Francis, D. J. Twitchen, S. Graham, and M. W. Holtz, "Ultraviolet and visible micro-Raman and micro-photoluminescence spectroscopy investigations of stress on a 75-mm GaN-on-diamond wafer," 2016.

[168] J. F. Muth, J. H. Lee, I. K. Shmagin, R. M. Kolbas, H. C. Casey, B. P. Keller, U. K. Mishra, and S. P. DenBaars, "Absorption coefficient, energy gap, exciton binding energy, and recombination lifetime of GaN obtained from transmission measurements," *Appl. Phys. Lett.*, vol. 71, no. 18, p. 2572, 1997.

[169] C. Y. Fang, C. F. Lin, E. Y. Chang, and M. S. Feng, "A study of subbands in AlGaN/GaN high-electron-mobility transistor structures using low-temperature photoluminescence spectroscopy," *Appl. Phys. Lett.*, vol. 80, no. 2002, pp. 4558–4560, 2002.

[170] N. Pauc, M. R. Phillips, V. Aimez, and D. Drouin, "Carrier recombination near threading dislocations in GaN epilayers by low voltage cathodoluminescence," *Appl. Phys. Lett.*, vol. 89, no. 16, pp. 2006–2008, 2006.

[171] T. Sugahara, H. Sato, M. Hao, Y. Naoi, S. Kurai, S. Tottori, K. Yamashita, K. Nishino, L. T. Romano, and S. Sakai, "Direct Evidence that Dislocations are Non-Radiative Recombination Centers in GaN," *Jpn. J. Appl. Phys.*, vol. 37, no. 4, pp. L398–L400, 1998.